

**Science and Engineering
Department of Chemical Engineering**

Novel Reactors for Multiphase Processes

Tejas Jagdish Bhatelia

**This thesis is presented for the Degree of
Doctor of Philosophy
of
Curtin University of Technology**

April 2009

Declaration

To the best of my knowledge and belief this thesis contains no material previously published by any other person except where due acknowledgment has been made.

This thesis contains no material which has been accepted for the award of any other degree or diploma in any university.

Signature:

Date:

Acknowledgement

It is a great pleasure for me to acknowledge all the people who helped me to accomplish this dissertation. First of all I would like to express my deepest gratitude to my supervisor Dr. Vishnu K. Pareek for giving me the opportunity to work in his group. It would be an understatement to say he has provided a whole-hearted support for this work. His indepth advice, encouragement, easy accessibility and freedom for work helped me to explore new ideas and to complete the work in time. I express my sincere gratitude to my co-supervisor Professor Moses Tadó for his timely support and advice. I am thankful to both of them for sharing ideas on many varied issues such as report writing, time management, presentation techniques etc. which helped me to develop my personal skills as well. I would also like to thank chairman of the doctoral commission, Professor Ming H. Ang, for evaluating my work.

My special thanks to Dr Ranjeet P. Utikar, for his knowledgeable advice, which was instrumental in completing this work. I would also like to thank my colleagues, Milin, Ganesh, Abid, Owen, Kailash, Johan, Kalpit, Mikhil, Nilesh, Chirayu and Pradeep, who ensured a technically stimulating, creative and pleasant working environment and helped in technical and non-technical matters. The support given by technical and IT staff, notably Ms. Karen Haynes, Mr. Glenvill Abeywickrema, Ms. Alison Lynton and Mr. Michael Akindeju is worthy mentioning. Timely help from the secretarial staff, namely Ms. Jann Bolton and Ms. Naomi Tokisue is highly appreciated.

Finally, I am thankful to my parents and family for their support during this stressful time. Last but not the least my wife, Nalini's support before and during this thesis writing cannot be expressed in words. I also acknowledge everyone who has assisted me directly or indirectly in the completion of this work. Their assistance is invaluable and shall always be held in high regards.

Biography of the Author

Tejas Bhatelia has studied the principles of chemical engineering for past 11 years which includes three degrees in chemical engineering and current enrollment as PhD student at Curtin University of Technology. He has extensively worked in the area of chemical engineering design, multiphase applications, numerical modeling and process engineering principles for past three and half years he has spent as a researcher at Curtin University of technology. His research interests lies into process intensification, novel reactors for multiphase applications, numerical modeling and Computational Fluid Dynamics. In the course of his PhD research his work has been refereed at international journals and conferences which include:

LIST OF PUBLICATIONS

1. Wang S. and Bhatelia T; “Comparison of Cu removal by Australian natural zeolite and fly ash” Studies in Surface Science and Catalysis, Volume 170, Part 2, 2007, Pages 2104-2109.
2. Bhatelia T., V.K. Pareek and M.O. Tade; “CFD Simulations of Multiphase GTL Reactor: Spinning Disc Reactor”, Poster Presentation at 1st International Congress on Green Process Engineering, 24 – 26 April, 2008, held in *Toulouse, France*.
3. Bhatelia T., V.K. Pareek and M.O. Tade; “Hydrodynamics of Slug Flow Capillary Micro Reactor” Proceeding of CHEMCON, 2008, *Chandigarh INDIA*.
4. Bhatelia T., V.K. Pareek, R.P. Utikar and M.O. Tade “CFD study of Slug Flow in Capillary Microchannel”. Proceedings of CHEMECA, 2008, *Newcastle (Australia)*.
5. Bhatelia T., V.K. Pareek, R.P. Utikar and M.O. Tade “Hydrodynamics of Slug Flow Capillary Micro-Reactor”, UniJet, Volume 1, 2009, Pages 1-7.
6. V.K. Pareek, Bhatelia T.J., Balliu N., Ang M., Tade M.O. and Vuthaluru H., “Chemical plant design project: A concurrent assessment of individual and team skills”, Evaluations and Assessment Conference, Enhancing Student Learning, 2006.

CONFERENCES AND WORKSHOPS

1. CHEMECA, “Towards a Sustainable Australasia” 28th September 2008 to 1st October 2008, Newcastle City Hall, Newcastle, Australia.
2. CEFRC, “Curtin Engineering Faculty Research Colloquium”, 6th November 2007, Curtin University of Technology, Perth Australia.
3. “Novel Techniques for Multiphase Reactors”, Workshop by Prof. Mike P. Dudukovic Director of the Chemical Reaction Engineering Laboratory Washington University in St Louis, 19th October 2007, Techonolgy Park, Bentley, Perth, Australia.
4. FLUENT user group meetings, 2004-2009.

Abstract

Process intensification tools, such as the capillary reactor, offer several benefits to the chemical process industries due to the well-defined high specific interfacial area available for heat and mass transfer, which increases the transfer rates, and due to low inventories, they also enhance the safety of the process. This has provided motivation to investigate three such tools, namely the capillary microreactor, spinning disc and rotating tube reactors, in this study.

The gas-liquid slug flow capillary microreactor intensifies reactor performance through internal circulation caused by the shear between the continuous phase/wall surface and the slug axis, which enhances the diffusivity and consequently increases the reaction rates. However, integrating the complex hydrodynamics of this reactor with its chemical kinetics is a mathematically challenging task. Therefore, in this study, a simple-to-complex approach, using a set of state-of-the-art computational fluid dynamic tools, has been used. Firstly, simulations were performed without any chemical reaction to ascertain the extent of slug flow regime. The model also clearly captured the slug flow generation mechanism which can be used to structurally optimize the angle of entry in these reactors. Finally, the hydrodynamic model was also capable of estimating the pressure drop and slug lengths. After successfully simulating the hydrodynamics of the system, a reaction model was incorporated to study the chemical reaction kinetics. The results were compared with the published experimental work and were found to be in good agreement.

The spinning disc reactor utilizes the centrifugal and shear forces to generate thin liquid films characterized with intense interfering waves. This enables a very high heat transfer coefficients to be realized between the disc and liquid, as well as very high mass transfer between the liquid and the bulk gas phase. The waves formed also produce an intense local mixing with very little back mixing. This makes a spinning disc reactor an ideal contactor for multiphase processes. The focus of this study has been to elucidate the hydrodynamic behaviour of the liquid film flow over the horizontal spinning disc. Investigations were also performed to elaborate the local and overall hydrodynamic characteristics of a fully developed spinning disc reactor. Simulation results showed a continuous linear liquid film on the horizontal spinning disc and intense mixing performance in the annulus of the reactor around the disc

surface. Finally, the film thickness data from the simulations were compared with the limited amount of data available for this novel process.

Rotating tube reactor also uses centrifugal forces to generate the liquid film and a high degree of mixing along with an improved control over the reactant retention times. In this work we have conducted a CFD analysis to understand the hydrodynamics of this new technology for future developments.

List of Tables

Chapter 1 Introduction

<i>Table 1 Literature review of various PI equipments</i>	<i>15</i>
---	-----------

Chapter 3 Computational Fluid Dynamics

<i>Table 2 Conservations equations expressed inform of general scalar quantity.....</i>	<i>29</i>
---	-----------

<i>Table 3 Governing equations of Eulerian Eulerian Model</i>	<i>38</i>
---	-----------

<i>Table 4 Constants of Morsi-Alexander drag model.....</i>	<i>39</i>
---	-----------

<i>Table 5 Governing equations of VOF model</i>	<i>40</i>
---	-----------

Chapter 4 Slug Flow Capillary Microreactor

<i>Table 6 Comparison of multiphase models [90].....</i>	<i>42</i>
--	-----------

<i>Table 7 Dimensionless quantities used to characterize flow in microchannel.....</i>	<i>55</i>
--	-----------

<i>Table 8 Geometry configurations for studying the effect of entry angle</i>	<i>56</i>
---	-----------

<i>Table 9 Simulation parameters (SFR)</i>	<i>58</i>
--	-----------

<i>Table 10 Comparison between 2D and 3D results</i>	<i>60</i>
--	-----------

<i>Table 11. Various correlations to calculate friction factor</i>	<i>69</i>
--	-----------

<i>Table 12 Operating conditions and physical properties for calculating pressure drop</i>	<i>72</i>
--	-----------

<i>Table 13 Comparison of analytical and CFD calculated pressure drop.....</i>	<i>72</i>
--	-----------

<i>Table 14 Simulation parameters for single phase simulation</i>	<i>76</i>
---	-----------

<i>Table 15 Literature review on numerical models for mass transfer with and without chemical reaction in the gas-liquid microreactor.</i>	<i>80</i>
---	-----------

<i>Table 16 Reactions in series for DC process.....</i>	<i>83</i>
---	-----------

<i>Table 17 Operating conditions for simulating chemical reaction</i>	<i>86</i>
---	-----------

<i>Table 18 Simulation parameters for species transport model.....</i>	<i>86</i>
--	-----------

<i>Table 19 Comparison of species mass fraction</i>	<i>89</i>
---	-----------

Chapter 5 Spinning Disc Reactor

<i>Table 20 Various models for liquid flow over spinning discs</i>	<i>95</i>
<i>Table 21 Dimensionless numbers for flow characterization in spinning disc.....</i>	<i>97</i>
<i>Table 22 Operating conditions for computing liquid film thickness.....</i>	<i>100</i>
<i>Table 23 Simulation parameters for computing liquid film thickness</i>	<i>101</i>
<i>Table 24 Measured film thickness in mm</i>	<i>105</i>
<i>Table 25 Operating Parameters (SDR).....</i>	<i>113</i>
<i>Table 26 Simulation Parameters for Eulerian-Eulerian Model.....</i>	<i>114</i>

Chapter 6 Rotating Tube Reactor

<i>Table 27 Operating conditions (RTB).....</i>	<i>123</i>
<i>Table 28 Simulation parameters (RTB)</i>	<i>123</i>
<i>Table 29 Operating and simulation parameters of modelling chemical reaction in RTB.....</i>	<i>125</i>

List of Figures

Chapter 1 Introduction

Figure 1 Outline of thesis 6

Chapter 2 A review of Process Intensification

Figure 2 Monolithic structures of various shapes. Square channel cordierite structures, internally finned channels, wash-coated [4] 11

Figure 3 Schematic of spinning disc reactor 12

Chapter 3 Computational Fluid Dynamics

Figure 4 Schematic of structured meshing scheme..... 24

Figure 5 Schematic of unstructured meshing scheme..... 25

Figure 6 Element of fluid 26

Figure 7 Schematic of staggered grid..... 34

Figure 8 General form of multiphase systems 36

Figure 9 Flow regimes in multiphase systems 37

Chapter 4 Slug Flow Capillary Microreactor

Figure 10 Various gas-liquid contactors [97]..... 50

Figure 11 Flow regimes observed in horizontal two phase flow [100]..... 52

Figure 12 Flow map of Suo and Griffith for $Ca/Re=1.5 \times 10^{-5}$ [104]..... 54

Figure 13 Schematic of microchannel used in modelling..... 56

Figure 14 a) Slug flow development in 2D $L_g = 6.36$ mm b) Slug flow development in 3D; $L_g = 4.96$ mm (red- gas slug and blue- liquid slug)..... 59

Figure 15 Slugs at different mesh resolution ($U_g = 0.1$ ms⁻¹, $U_l = 0.1$ ms⁻¹, $t = 0.5$ s); a) Grid size 0.4mm b) Grid size 0.3mm c) Grid size 0.25mm & d) Grid size 0.2mm..... 61

Figure 16 Effect of grid size on analytical Laplace pressure drop across the interface. 62

<i>Figure 17 a) Contours of volume fraction of air $U_l = 0.1, 0.05, 0.025$ & 0.01 ms^{-1} (left to right); b) Effect of liquid velocity on mean gas slug length. $U_g = 0.1 \text{ ms}^{-1}, t = 0.5\text{s}$.....</i>	<i>63</i>
<i>Figure 18 a) Contours of vorticity magnitude in mixing zone for various inlet geometries b) Mean gas, liquid slug length and number of gas slugs for varying angle of entry $U_g = 0.1 \text{ ms}^{-1}, U_l = 0.1 \text{ ms}^{-1}, t = 0.5\text{s}$.....</i>	<i>64</i>
<i>Figure 19 Mean gas slug length and number of gas slugs for varying channel diameter; $U_g = 0.1 \text{ ms}^{-1}, U_l = 0.1 \text{ ms}^{-1}, t = 0.5\text{s}$.....</i>	<i>65</i>
<i>Figure 20 Bond number versus effective channel diameter.....</i>	<i>66</i>
<i>Figure 21 Ratio of slug detachment length required between horizontal and vertical channel for varying channel diameters $U_g = 0.1 \text{ ms}^{-1}, U_l = 0.1 \text{ ms}^{-1}$.....</i>	<i>67</i>
<i>Figure 22 Effect of contact angle on mean gas and liquid slug length.</i>	<i>68</i>
<i>Figure 23 Typical alternate gas-liquid slug flow in microchannel</i>	<i>74</i>
<i>Figure 24 Schematic of the internal recirculation in gas bubble and liquid slug.....</i>	<i>74</i>
<i>Figure 25 Grid display of gas bubble and liquid slug.....</i>	<i>75</i>
<i>Figure 26 Contours of velocity gas bubble(Left) and Liquid Slug(Right) ($L_g = 4.7\text{mm}, L_s = 3.7\text{mm}, U_{(avg)} = 0.2 \text{ m/s}$).....</i>	<i>77</i>
<i>Figure 27 Velocity vectors within gas bubble and liquid slug, internal recirculation, gas bubble(Left) and Liquid Slug(Right) ($L_g = 4.7\text{mm}, L_s = 3.7\text{mm}, U_{(avg)} = 0.2 \text{ m/s}$)</i>	<i>77</i>
<i>Figure 28 Parabolic velocity profile within the liquid slug ($L_s = 3.7\text{mm}, D = 1.8\text{mm}$ and $\delta = 0.1\text{mm}$).....</i>	<i>78</i>
<i>Figure 29 Internal circulations by particle tracing in gas bubble and liquid slug ($L_g = 4.7\text{mm}, L_s = 3.7\text{mm}, U_{(avg)} = 0.2 \text{ m/s}$).....</i>	<i>78</i>
<i>Figure 30 Schematic of the microchannel for reaction.</i>	<i>84</i>
<i>Figure 31 Contours of mass fraction of hydrogen peroxide.....</i>	<i>87</i>
<i>Figure 32 Contours of mass fraction of hydrogen.....</i>	<i>87</i>
<i>Figure 33 Mass fraction of hydrogen Peroxide along the reaction zone</i>	<i>88</i>

<i>Figure 34 Mass fraction of hydrogen along the reaction zone.....</i>	<i>88</i>
---	-----------

Chapter 5 Spinning Disc Reactor

<i>Figure 35 Schematic of agitated vessel fitted with cooling jacket.....</i>	<i>92</i>
---	-----------

<i>Figure 36 Liquid film behaviour on a rotating disc observed by Woods [147]</i>	<i>94</i>
---	-----------

<i>Figure 37 Schematic of the computed domain for model validation</i>	<i>99</i>
--	-----------

<i>Figure 38 Assumed flow schematic.....</i>	<i>102</i>
--	------------

<i>Figure 39 Computed volume fraction of water for 2D (a) and 3D (b) model. $Q = 18\text{ml/sec}$, $\omega = 21\text{ Rad/sec}$, 2D radius 15cm, 3D radius 3.5cm.....</i>	<i>104</i>
---	------------

<i>Figure 40 Effect of rotational speed on the non dimensional liquid film thickness $Q = 10\text{ml/s}$ Disc diameter = 10cm.....</i>	<i>105</i>
---	------------

<i>Figure 41 Effect of rotational speed on the non dimensional liquid film thickness $Q = 14\text{ ml/s}$ Disc diameter = 10cm.....</i>	<i>106</i>
--	------------

<i>Figure 42 Effect of rotational speed on the non dimensional liquid film thickness $Q = 18\text{ ml/s}$ Disc diameter = 10cm.....</i>	<i>107</i>
--	------------

<i>Figure 43 Effect of volumetric flow rate on measured and calculated non dimensional film thickness compared with the experimental data Burns et al.....</i>	<i>108</i>
--	------------

<i>Figure 44. Non dimensional film thickness in a 5cm radius disc for varying volumetric flow rate.</i>	<i>110</i>
--	------------

<i>Figure 45 Schematic of the Spinning Disc Reactor used for Eulerian- Eulerian model</i>	<i>112</i>
---	------------

<i>Figure 46 Sections of geometry for velocity mapping</i>	<i>114</i>
--	------------

<i>Figure 47 Velocity vectors rotational speed 300 RPM (Left) and 0 RPM (Right) ..</i>	<i>115</i>
--	------------

<i>Figure 48 Velocity profile along the radial distance for varying axial lengths. $U = 0.1\text{ m/s}$ Disc Speed = 300 RPM.....</i>	<i>116</i>
--	------------

<i>Figure 49 Velocity profile at $Z=2.5\text{cm}$ for varying disc speeds.</i>	<i>117</i>
--	------------

<i>Figure 50 Velocity profile at $Z=12.5\text{cm}$ for varying disc speeds.</i>	<i>117</i>
---	------------

<i>Figure 51 Velocity profile at $Z=12.5\text{cm}$ for varying disc speeds</i>	<i>118</i>
---	------------

Chapter 6 Rotating Tube Reactor

<i>Figure 52 Image of the tube reactor [159].....</i>	<i>121</i>
<i>Figure 53 Schematic of the rotating tube used for computational model.....</i>	<i>122</i>
<i>Figure 54 Effect of rotational speed on the velocity profiles $U = 40\text{mm/sec}$.....</i>	<i>124</i>
<i>Figure 55 Particle trajectories for rotating tube at varying rotational speed $U = 40\text{mm/sec}$.....</i>	<i>125</i>
<i>Figure 56 Inlet configurations.....</i>	<i>126</i>
<i>Figure 57 Mass fraction of CO_2 along the length of the tube.....</i>	<i>126</i>
<i>Figure 58 Particle trajectories varying rotational speed $U_{\text{air}} = 0.1 \text{ m/s}$, $U_{\text{ethylene}} = 0.1 \text{ m/s}$.....</i>	<i>127</i>

Table of Contents

Acknowledgement

Abstract

List of Tables

List of Figures

Table of Contents

Chapter 1 Introduction	1
1.1 <i>Slug-Flow Capillary Microreactor</i>	2
1.2 <i>Spinning disc reactor</i>	3
1.3 <i>Rotating tube reactor</i>	3
1.4 <i>Objectives</i>	3
1.5 <i>Contribution of thesis</i>	4
1.6 <i>Thesis outline</i>	5
Chapter 2 A Review of Process Intensification	7
2.1 <i>Introduction</i>	7
2.2 <i>Process Intensification Technologies</i>	8
2.2.1 <i>Equipment for Process Intensification</i>	8
2.2.1.1 <i>Static Mixer Reactors</i>	9
2.2.1.2 <i>Microreactors</i>	9
2.2.1.3 <i>Monolithic catalytic reactors</i>	10
2.2.1.4 <i>Spinning Disc Reactors</i>	11
2.2.2 <i>Methods for Process Intensification</i>	12
2.2.2.1 <i>Heat Integrated Reactors</i>	12
2.2.2.2 <i>Reactive Separations</i>	13
2.2.2.3 <i>Hybrid Separators</i>	14
2.2.2.4 <i>Alternative Source of Energy</i>	18
Chapter 3 Computational Fluid Dynamics	20
3.1 <i>Introduction</i>	20
3.2 <i>Pre-analysis</i>	21
3.3 <i>Pre-processing</i>	22
3.3.1 <i>Structured grid</i>	23
3.3.2 <i>Unstructured grid</i>	23

3.4 CFD codes	25
3.5 Conservation equations.....	26
3.5.1 Continuity equation	27
3.5.2 Momentum equation.....	27
3.5.3 Energy equation.....	28
3.6 <i>Generic transport equations</i>	29
3.6 <i>Numerical techniques</i>	29
3.6.1 Finite difference method.....	30
3.6.2 Finite element method	30
3.6.3 Finite volume method.....	30
3.7 <i>Multiphase flow modelling</i>	35
3.7.1 Flow regimes in multiphase processes	37
3.7.2 Eulerian Eulerian model	38
3.7.3 Volume of fluid model	40
3.7.4 Selection of multiphase model	41
3.8 <i>Summary</i>	41
3.9 <i>Nomenclature</i>	44
4. Slug Flow Capillary Micro-Channel.....	47
4.1 <i>Introduction to Micro-technology</i>	47
4.2 <i>Gas-Liquid Contactors</i>	48
4.3 <i>Microchannel</i>	51
4.4 <i>Flow characterisation</i>	53
4.5 <i>Computational model</i>	56
4.5.1 Model Geometry.....	56
4.5.2 Model Parameters	57
4.5.3 Simulation Parameters.....	57
4.6 <i>Results and Discussion</i>	58
4.6.1 Comparison of 2D and 3D model.....	58
4.6.2 Effect of mesh size	60
4.6.3 Comparison with previous work.....	62
4.6.5 Effect of angle of entry	63
4.6.6 Effect of channel diameter.....	65
4.6.7 Effect of gravity.....	66
4.6.8 Effect of Contact angle	67
4.6.9 Pressure drop	67
4.6.10 Internal recirculation.....	73
4.6.10.1 Phenomenological model.....	75
4.6.11 Chemical reaction	78

4.7 Summary.....	89
4.8 Nomenclature	90
5 Spinning Disc Reactor	91
5.1 Introduction.....	91
5.2 Literature Review.....	93
5.3 Flow characterisations	97
5.4 Computation of film thickness (VOF)	98
5.4.1 Computational model	98
5.4.2 Analytical approach.....	100
5.4.3 Results and Discussion	103
5.4.3.1 Comparison of 2D and 3D model	103
5.4.3.2 Effect of rotational speed	105
5.4.3.3 Effect of Volumetric Flow rate.....	107
5.4.4 Computation of velocities.....	110
5.4.4.1 Phenomenological model	111
5.5 Summary.....	118
5.6 Nomenclature	119
6 Rotating Tube Reactor	120
6.1 Introduction.....	120
6.2 Computational Model	121
6.3 Model Geometry	122
6.4 Simulation Parameters.....	122
6.5 Results and discussion	123
6.5.1 Hydrodynamics	124
6.5.2 Modelling of chemical reaction	125
6.6 Summary.....	127
7 Conclusions and Future Developments	128
7.1 Capillary Microreactor.....	128
7.1.1 Hydrodynamics	128
7.1.2 Chemical reaction.....	130
7.2 Spinning disc reactor	130
7.3 Rotating tube reactor	131
7.4 Open questions	131
7.4.1 Microreactor.....	131

7.4.2 Spinning disc reactor	132
7.4.3 Rotating tube reactor	132
7.5 <i>Recommendations for Future Work</i>	132
7.5.1 Capillary Microreactor	132
7.5.2 Spinning disc reactor	134
7.5.3 Rotating tube reactor	135
Bibliography	136
Appendix A.....	146

Chapter 1 Introduction

Global climate change is driving chemical industries to develop cleaner sustainable technologies. One of the major challenges for chemical industries is to minimize the waste generation either by developing alternative synthesis and processing routes or by designing novel equipments which exhibit improved transport rates by increasing specific interfacial area, which in turn reduces the diffusional path lengths and helps in enhancing the safety by virtue of the lower hold-up and superior temperature control, even for strongly exothermic reactions. Consideration is also given to the overall energy requirements by reducing the pressure drops and improving the energy efficiency. In general, design of novel equipments and technologies is termed as “Process intensification”, which offers opportunities to chemical industry primarily in six broad areas: in reducing costs, safety, compactness, controlled and well-defined conditions, time to the market, and the overall image of the company. It leads to substantially cheaper processes, particularly in terms of land usage (much higher production capacity and/or number of products per unit of manufacturing area), investment costs (smaller equipment, reduced piping, etc.), the cost of raw materials (higher yields/selectivities), utilities (in particular energy), and waste processing (reduction in waste amounts).

The majority of the chemical processes involve more than one phase. Processes such as extraction, chemical reaction, mass-transfer, separation, etc., involve multiphase flows utilizing miscible and immiscible fluids. Multiphase flows are dominated by

the phenomena such as bubble transport, formation, breakup, coalescence, etc. in these processes an efficient contacting of multiple phases is essential for enhanced heat and mass transfer rates. Therefore, the concept of process intensification is likely to play a vital role in multiphase processes in the coming decade. The performance of multiphase processes is generally governed by the underlying hydrodynamics. Hence it is important to understand the basic hydrodynamics associated with multiphase processes to elaborate its performance. In this work, we have performed detailed hydrodynamic characterization (with and without chemical reaction) for two novel multiphase reactors (Chapter 4 and 5) and performed preliminary analysis on another type of reactor (Chapter 6).

1.1 Slug-Flow Capillary Microreactor

Process intensification via microreactor technology has remained an important strategy for many chemical processes. Microreactors offer superior mass transport and selectivity over the conventional gas-liquid (-solid) contactors. Due to their small dimensions, these reactors have high surface to volume ratio, and consequently exhibit high heat and mass transfer coefficients. Secondly, they provide simplicity in scaling up by these systems simple replication or bundling of microreactor units. This minimizes the cost of redesigning, thus shortening the development time from the lab scale to commercial scale production. For these reasons, microreactors are finding increasing applications in multiphase processes. Numerous researchers over the past decade have used microchannels for various applications which includes the solid catalyzed gas-liquid reactions [1-4], hydrogenation [5-8], and Fischer-Tropsch synthesis [7].

The performance of a microreactor largely depends on the underlying hydrodynamics of the gas-liquid (-solid) flow. Depending on the operating conditions and design parameters, the gas-liquid flow in a microchannel can exhibit various flow regimes viz. bubbly, churn, slug and annular flow [9-16]. Over a wide range of operating conditions, the slug flow regime which is characterized by alternate bullet shaped bubbles separated by free gas-entrained liquid slugs is observed. This flow regime is sometimes also referred as the Taylor flow regime [10]. This work focuses on understanding the hydrodynamic characteristics with and without chemical reactions in a slug flow capillary microchannel/microreactor using a computational fluid dynamics (CFD) approach.

1.2 Spinning disc reactor

Another potential process intensification route involves the use of centrifugal forces to generate thin, unstable and wavy liquid films over a disc in the presence of a bulk gas phase. These reactors are known as the spinning/rotating disc reactors (SDR). There exists a strong turbulence within the waves in the liquid film over the spinning disc resulting in the enhancement of heat and mass transfer rates. These waves also produce intense micro mixing and very little back mixing bringing these reactors closer to an ideal plug flow. This is of particular advantage with fast liquid-liquid reactions such as nitration, sulphonation and polymerization [17]. These reactors have also shown potential benefits for unit operations such as absorbers, humidifiers, dust collectors, dryers, evaporators etc [18]. Owing to these advantages, the SDR has found various applications in manufacturing of fine chemicals and pharmaceuticals [19].

Hydrodynamic behaviour of the liquid film directly influences the heat and mass transfer performance of these reactors [20]. Characteristic behaviour of the liquid film can be closely related to the falling film theory for which a considerable amount of theoretical and experimental work exists in the open literature [21]. But there is still only a little understanding on the behaviour of the film under the influence of centrifugal forces. Computational fluid dynamics (CFD) models can provide an in-depth insight on the hydrodynamics of such complex processes. However, no such study is available in the open literature.

1.3 Rotating tube reactor

Rotating tube reactor (RTB) also uses centrifugal force to generate thin liquid films but unlike the spinning disc reactors where liquid moves off the disc giving very little control over the retention times, in the RTB, the reactant retention time is independent of the rotation of the tube. The concept is promising and to the best of our knowledge has never been investigated before. Thus a complete CFD analysis was performed to provide a foundation for the future development of this reactor type.

1.4 Objectives

Therefore, the overall objective of this study was to elucidate the hydrodynamics of novel reactors for multiphase processes using computational fluid dynamics, models

In summary the goals of this research were:

- 1) Slug Flow Capillary Microreactor
 - a. To investigate the hydrodynamics of the slug flow capillary microreactors.
 - b. To characterize the internal recirculation of gas bubbles and liquid slugs.
 - c. To study the effect of gas-liquid chemical reaction on a capillary reactor.
 - d. To calculate the pressure drop along the channel and investigate the specific energy and power requirement.
- 2) Spinning disc reactor
 - a. To develop a CFD model for predicting the liquid film thickness under various operating and design conditions.
 - b. To develop flow mapping in fully developed three dimensional spinning disc reactor.
- 3) Rotating tube reactor
 - a. To perform preliminary analysis for understanding hydrodynamics of the rotating tube reactor.
 - b. To incorporate a simple chemical reaction and compare the performance, with and without the reaction.

1.5 Contribution of thesis

The contribution of this thesis is focused on understanding the behaviour of the novel reactors for multiphase processes. This work provides an insight into hydrodynamic behaviour of these reactors with the help of computational fluid dynamics modelling. Major contribution of this thesis can be summarized as follow:

1. Slug flow capillary microchannel:

- The hydrodynamic model presented in this work provides detailed analysis of the slug flow capillary microchannel for various operating, geometric and simulation parameters.
- Pressure drops across the capillary microchannels were analytically and computationally calculated and compared.
- A methodology has been presented to detail the important internal recirculation.

- Performance of the reactor was studied for the DC process for production of hydrogen peroxide.

2. Spinning disc reactor:

- Important hydrodynamic characteristics of the liquid film behaviour over the horizontal spinning disc have been elaborated through 2D and 3D computational models.
- A methodology has also been developed to analyze the velocity profiles on and around the disc surface rotating at very high speeds.

3. Rotating tube reactor:

- Hydrodynamic performance of the rotating tube reactor has been presented and simple chemical reaction kinetics in this reactor has also been studied.

1.6 Thesis outline

As shown in Figure 1, the thesis is divided into three sections: (i) Microreactor (Chapter 4), (ii) Spinning disc reactor (Chapter 5) and (iii) Rotating tube reactor (Chapter 6). Chapter 2 provides a review of the process intensification tools and CFD model formulations and methodologies are explained in Chapter 3. Finally, Chapter 7 summarizes the results from this study.

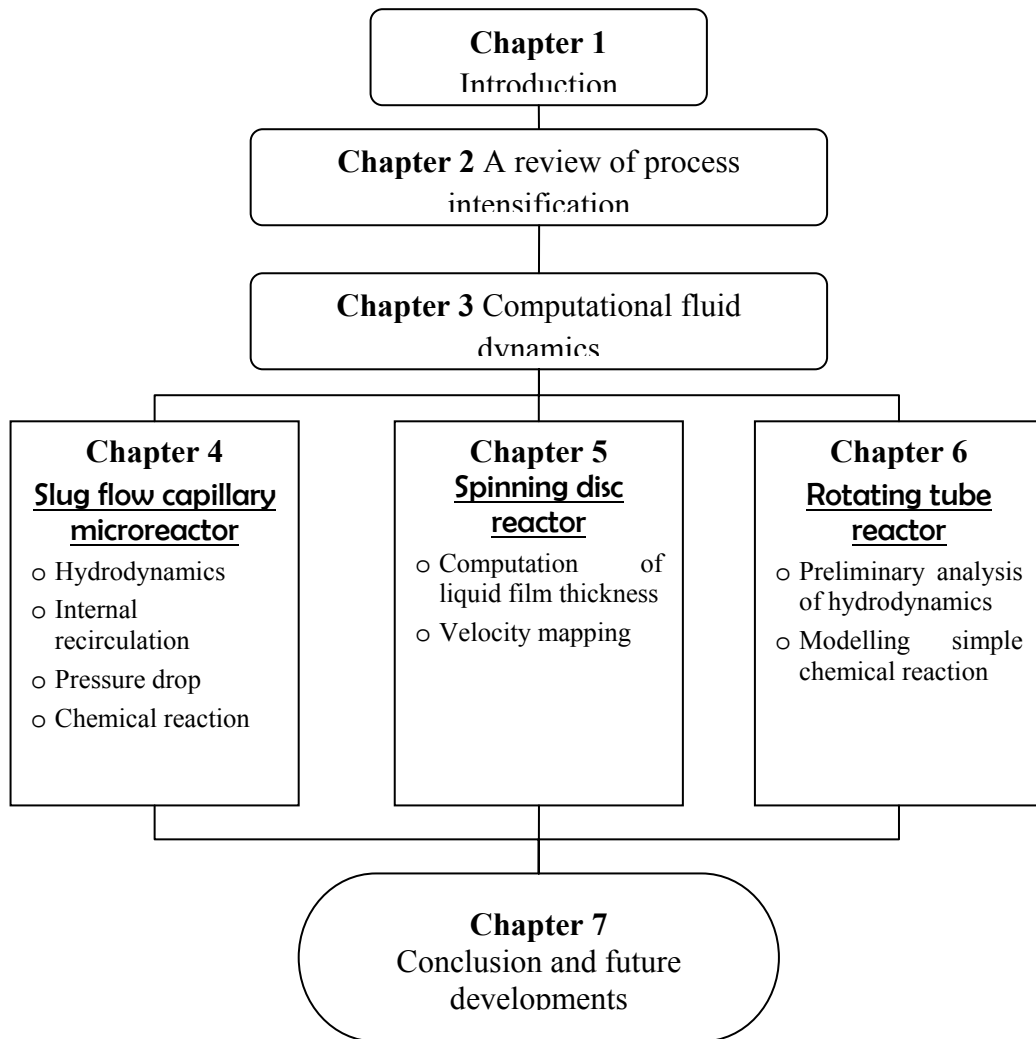


Figure 1 Outline of thesis

Chapter 2 A Review of Process Intensification

2.1 Introduction

In the recent years, more and more efforts are being made to design novel processes which are compact, safe, energy-efficient, environmentally friendly and sustainable. Commonly known as “Process Intensification” (PI), nucleates these qualities into a design. Hence it has gained an increasing popularity amongst the engineers and scientists all over the world.

The concept of process intensification has been around for quite a some time but it is only since the past two decades that we have started to understand and apply its principles to real chemical processes. Some of the first definitions of process intensification were given at the Annual Research Meeting (Process Intensification), held at the UMIST, Manchester [17]. The pioneer of the process intensification Prof. Collin Ramshaw first defined it in 1983 as [22],

“Process intensification is described as devising an exceedingly compact plant which reduces both the main plant item and the installation costs”.

Since then, process intensification has been defined by various researchers in their own perspectives, for example Heggs has defined the process intensification as the process which is “concerned with the order of magnitude reductions in the process plant and equipment” [23], Moulijn describes the process intensification to “consists of the development of novel apparatuses and techniques that, compared to those commonly used today, are expected to bring dramatic improvements in manufacturing and processing, substantially decreasing equipment-size/production-capacity ratio, energy consumption, or waste production, and ultimately resulting in cheaper, sustainable technologies”, [24].

Chemical industries are being driven towards the process intensification due to its particular advantages such as:

- Increased production capacity per unit land usage.
- Reduced capital and operating costs.
- Higher yields and selectivity.
- Shorter time to the market.
- Less waste/by-products handling.
- Shorter time to the market.
- Better company image.

2.2 Process Intensification Technologies

There are mainly two approaches to intensify any given process. In the first approach the core components (reactors/unit operations) of the process are replaced by novel components such as the spinning disc reactor, microreactors, monolith reactors, micro heat exchangers, centrifugal absorbers etc. In the second approach, the process is carried out using multifunctional reactors, hybrid separators, alternative energy resources etc. In practical systems, a combination of both approaches is used, due to the fact that new components will require new approaches and vice versa.

2.2.1 Equipment for Process Intensification

Process intensification is carried out on mainly two types of equipments, reactive and nonreactive equipments [17]. Some of the examples of reactive equipments include the spinning disc, static mixer, monolith, and micro reactors. Centrifugal absorbers,

rotating packed bed, micro heat-exchangers, and static mixers are classified as non reactive equipments.

Each of the novel reactive equipment offers unique advantages and the choice of the reactor is dependant on various factors such as the contacting pattern, the number of phases, desired heat and mass transfer coefficients etc. On the other hand, it is comparatively easy to select non reactive intensified equipments. Some of the equipments that have been developed recently are described below:

2.2.1.1 Static Mixer Reactors

A static mixer reactor mainly comprises of a series of mixing elements fixed in a pipe, which uses the energy of the flow stream to create mixing between two or more fluids. Furthermore, when reaction is incorporated with mixing it offers many advantages such as [25]:

- Continuous flow that assures a constant product quality from the reactor.
- Almost ideal plug flow behaviour resulting in a sharply defined end-product and intense micro mixing.
- Ability to handle highly viscous liquids.
- Excellent heat transfer characteristics, this permits the processing of reactions with relatively large reaction enthalpies.
- Short residence time.
- Easy to scale up.

Static mixer reactor is one of the first equipment to be developed and applied commercially. One of the major breakthroughs in this equipment was brought by SLUZER by making the mixing elements of heat transfer tubes. This has made it possible to apply the static mixer reactors in processes requiring continuous mixing and heat transfer such as the nitration, neutralization and polymerization reactions.

2.2.1.2 Microreactors

Microreactors are defined as miniaturized reaction systems fabricated by using, at least partially, methods of microtechnology and precision engineering [26]. Typical dimensions of microreactors range from sub-micrometer to sub-millimetres. Micro reactors have shown significant benefits in intensifying the heat and mass transfer

rates. Many examples of these are extensively studied by Wolfgang et al. [27] They have emphasized on some of the major advantages of microreactor units which are described below:

- Advantages due to the decrease in physical size
- Decreasing linear dimensions increases the respective gradient in physical properties such as temperature, concentration, density or pressure which, are the driving forces of the heat and mass transport in chemical process.
- Increase in Surface to volume ratio by a factor ranging from 10 to 50 times higher than the laboratory and production scale equipments.
- Decreased volume of the reactor means smaller hold ups, safer processes and short residence times.
- Less time requirement for concept to market.
- Reduced land and plant costs.
- Flexibility in operation.

2.2.1.3 Monolithic catalytic reactors

This type of reactors consists of blocks of monolith catalyst placed in the tubular reaction vessels. Some of the commonly used monoliths are shown in Figure 2. Monoliths comprises of a number of microchannels through which the reaction mixture is allowed to flow. Reaction takes place both in the fluid bulk and, primarily, on the catalyst-coated inner surfaces of the channels. Flow in the channels is essentially laminar, and significant gradients in temperature and concentrations of reactants and products exist between the bulk fluid and the surface. Substantial heat transfer is observed across the solid walls of the channels. Most popular example of monolith catalytic reactor is the automotive exhaust gas converter which uses monolith catalyst. Monolithic catalytic reactors have also shown particular advantages in multiphase processes [4].

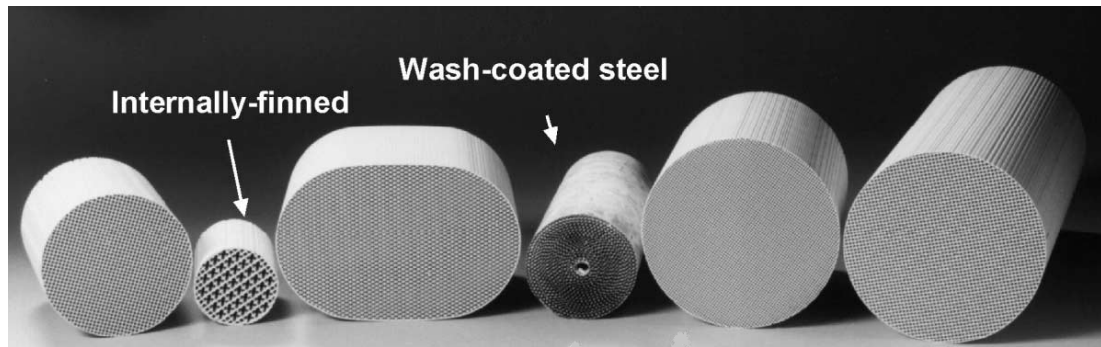


Figure 2 *Monolithic structures of various shapes. Square channel cordierite structures, internally finned channels, wash-coated [4]*

Keptejin et al [28] concluded that, for the gas-liquid reactions, the monolith reactors can combine advantages of the slurry reactor and trickle bed reactors. In another study, it was found that the reactor size could be reduced by a factor of 100, by simply replacing the conventional reactor with a monolith reactor placed horizontally in a pipeline [29]. Therefore, it is clear that the monolith reactors offer many advantages such as the high surface to volume ratios, high catalytic efficiency as well as low pressure drops for a wide range of applications.

However, the monolith reactors also have some drawbacks. For example, Grolman et al [30] studied the hydrodynamic instabilities in gas-liquid monolith reactors. They have reported that in the conventional multiphase monolith reactors, it is difficult to maintain a stable gas-liquid flow under the gravity and also the flow distribution along the top of the reactor is not uniform [30]. Hence to maintain a stable and uniform flow, higher throughputs will be required, resulting in relatively low residence times [29]. This adversely reduces the conversion per pass, and larger recycles of the liquid are needed. One of the improvements suggested by Stankiewicz [29] was to use an in-line monolith reactor instead of the conventional monolith vessel. Their modelling results showed dramatic improvements in the reactor performance and reductions in the reactor volumes by a magnitude of up to 2 times. This makes the monolith reactor an attractive choice in process intensification.

2.2.1.4 Spinning Disc Reactors

In a spinning disc reactor (SDR), a centrifugal force is applied to the liquid which generates thin, unstable and wavy liquid films over the disc. A schematic of a typical SDR is shown in Figure 3 below. Because of the strong turbulence, liquid films over the spinning disc possess very high heat and mass transfer rates. These waves produce

intense micro mixing and very little back mixing bringing these reactors closer to an ideal plug flow. This is of particular advantage when performing fast liquid-liquid reactions such as the nitration, sulphonation and polymerization [17]. These reactors have also shown potential benefits as unit operations such as absorbers, humidifiers, dust collectors, dryers, evaporators etc [18]. Owing to these advantages the SDR has found various applications manufacturing of fine chemicals and pharmaceuticals [19].

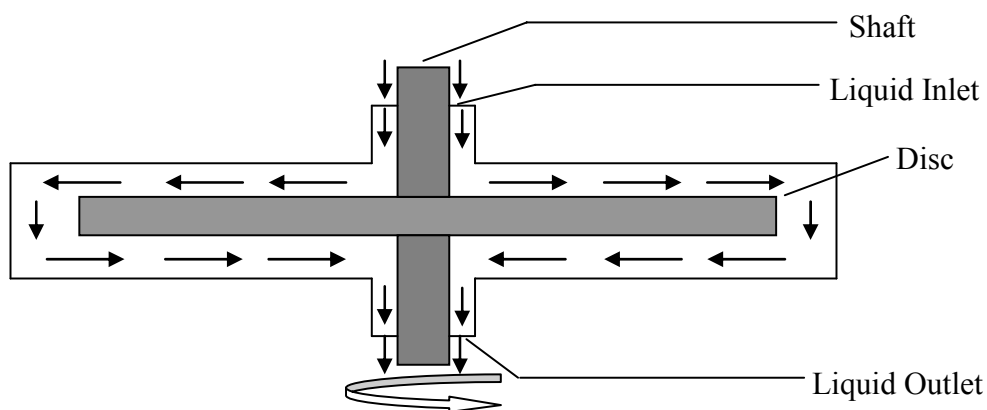


Figure 3 Schematic of spinning disc reactor

2.2.2 Methods for Process Intensification

Process intensification can be carried out by using novel processing methods, non-conventional energy and novel operational techniques [17]. Novel processing methods include use of a single equipment to conduct reaction and one or more other unit operations, which conventionally would have been carried out in different equipment. It also includes the use of hybrid separation systems such as membrane adsorptions, adsorptive distillation and membrane distillation. When conventional energy sources are replaced by nonconventional or alternative forms of energy, they can result in a significant reduction in the operating costs. Some of the other methods that are studied for process intensifications include the use of alternate operational techniques, such as replacing conventional fluids by supercritical fluids and conducting rigorous process integration.

2.2.2.1 Heat Integrated Reactors

The majority of the chemical reactions used commercially involve either generation or absorption of energy in the form of heat. For optimal thermodynamic efficiencies,

a significant number of these reactions require fast removal of heat. Conventionally, these processes are performed in jacketed /coiled tank reactors. In 1999 BHR group working in conjunction with Chart Marston developed a promising reactor technology for highly exothermic reactions – an integrated chemical reactor heat exchanger (HEX) [31]. Typically these HEX-chemical reactors offer very high heat exchange coefficients in the range of 3500-7500 Wm⁻²K⁻¹ and heat transfer areas up to 2200 m² per m³ [17]. HEX-reactors also provide a better control over the product selectivity. For example, Phillips and Symonds (1999) [31] decreased the by-product formation by up to 75% in the ICI acrylics process. They were also able to reduce the process time in a Hickson and Welch Fine chemical process from 18 hours to 15 minutes. In summary, HEX-reactors offer safe, clean and efficient processing of exothermic processes.

2.2.2.2 Reactive Separations

In conventional chemical plants, the reaction and separation are performed independently in different process equipments. There lies a potential to couple these two types of unit operations into single equipment. One of such multi functional reactors, which is commonly applied in process industry, is the reactive distillation [17]. In these reactors, packed distillation columns are used, in which the material used for packing is either the catalyst itself or an inert packing lined with the catalyst. Simultaneously the chemicals react on the catalyst surface and the resulting products are separated by a fractionation. The synergistic effect of this combination has the potential to increase the conversion, improve the selectivity, thus significantly reducing the capital investment and providing additional flexibilities for the operation [32]. Hence, this class of PI equipment is under constant scrutiny by numerous researchers around the world. Most of these developments are summarized in a review by Taylor and Krishna (2000) [33].

When the reactive distillation is carried out in a batch mode, it is called the reactive batch distillation (RBD). This combines the advantages of reactive distillation and batch processing [32], and can provide a new dimension to PI for the processes involving multiple reactive and separation equipments. Reactive distillation has been widely applied in hydrocarbon processing such as the esterification, halogenations, acylation, poly-condensations etc. [34] and is finding more and more versatile applications in the chemical process industry.

Some of the chemical processes involve single phase liquid–liquid reactions. In such processes conventionally the products from the reactor are extracted using a solvent in liquid-liquid extractors. Sharma and co-workers [35-38] considered performing these two operations (reaction and extraction) in single equipment called the Reactive Extraction [35-38]. This process has a great PI potential as it continuously removes the products from the catalyst surfaces, thus favoring the desirable reaction over the undesired products. Hence, these processes have higher yields, improved selectivity and smaller amount of by-product [39]. Consequently, a number of different designs of multi-functional reactors and other PI equipments have been used for the synthesis of several chemicals. A brief review of these studies is given in Table 1.

2.2.2.3 Hybrid Separators

A Hybrid separator incorporates two or more separation pathways to enhance the separation efficiency. Below we briefly review some of the hybrid separators:

- Hybrid Absorption and Stripping (Membrane):

The most commonly known hybrid separators involve a membrane along with the absorption and stripping. This technology offers advantages over the conventional mass transfer processes, such as high selectivity, compact design and high volumetric mass transfer coefficients. Moreover, in the hybrid separators, the gas and liquid flow rates can be varied independently to avoid flooding, loading or weeping [40, 41]. This technology has shown promising results in the removal of volatile organic compounds in gas and liquid effluents [41].

- Hybrid Absorption and Stripping (non-membrane):

For azeotropic mixtures, a combination of adsorption and distillation can be utilised to overcome the difficulties encountered in a conventional azeotropic distillation systems [42]. In this technique, typically there are three stages, namely the distillation-adsorption-distillation. When in the first stage, the pinch point is achieved; a solution/adsorbent is added to change the concentration of a component. This allows a further separation in the final stage of distillation. Another modification to this technique called the pressure-swing adsorption distillation using molecular sieves has been successfully applied to industrial scale water removal from isopropanol-water azeotrope [43].

Table 1 Literature review of various PI equipments

No	Equipment	Advantages	Applications	References
1	Rotating packed bed	Tall columns can be replaced by smaller equipments using centrifugal forces. Increased mass, heat and momentum transfer. Can be applied to reacting and multiphase systems.	Deaeration of flood water from oil fields [44]. Hypochlorous Acid process of Dow [45]. Hydrogenation of α -methyl styrene [46].	Zheng et al (1997) [44] Trent et al (2001) [45] Dhiman et al (2005) [46]
2	Centrifugal adsorber	Short contact times. Large interfacial area. Short diffusion lengths. High Capacities Compact equipment	Recovery of volatile material from industrial waste water [47]. Adsorption of bovine serum albumin (BSA) [48].	Bisschops et al (2002) [48].
3	Reactive Crystallization	Improved crystal growth Favourable reaction kinetics	Liquid Phase oxidation of Para-xylene to terephthalic acid [49].	Bayley et al (1992) [50] Kelkar et al (1999) [49]

		Can be used for production of nano-size specialty chemicals.	Acidic Hydrolysis of sodium salicylate to Salicylic acid [49]. Adsorption of ammonia in aqueous sulphuric acid to form ammonium sulphate [49]. Diastereomic Crystallisation [50]. Synthesis of calcite nanocrystal [51]	Lina et al (2006) [51]
4	Reactive Absorption	Can replace high energy demanding processes like cryogenic distillation Reduced number of equipment can provide economic benefits	Production of Nitric and sulphuric acid [52]. Gas purification [52]. Olefin/paraffin separations [52].	Douglas J. Safarik R. Bruce Eldridge (1998) [52].
5	Reactive Extrusion	Decreased quantities of solvents required when processing highly viscous fluids.	Polymerisation reactions [53, 54]: Bulk polymerisation Graft Reactions Interchange copolymer	Ebrahimi-Moshkabad and Winterbottom (1999) [53]

			<p>Crosslink reactions</p> <p>Controlled degradations</p> <p>Functional Group modifications</p>	
6	<p>Reactive Absorption</p> <p>Chromatographic Reactor [55, 56]</p> <p>Trickle flow reactor [57]</p> <p>Periodic separation reactors [58]</p> <p>Simulated moving bed reactor [59]</p>	<p>Versatile PI applications.</p> <p>Improved reaction kinetics.</p> <p>In some cases conversions can be achieved higher than the equilibrium conversions.</p>	<p>Methanol Synthesis</p> <p>Production of bisphenol-a</p> <p>Isomerisation of glucose</p> <p>Production of dextran etc</p>	<p>Dunnebie et al (2000)</p> <p>Lode et al (2001) [55]</p> <p>Vaporcyian et al (1989) [58]</p> <p>Westertrep et al (1988) [57]</p> <p>Kenig et al (2001) [56]</p>

- Membrane Chromatography:

Membrane chromatography is a combination of liquid chromatography and membrane filtration. This consists of a micro porous or macro porous membrane containing functional ligands attached to their inner pore structure which acts as adsorbents [17]. Recently, Wickramasinghe and Grzenia [60] have compared the performance of the membrane chromatography with the conventional method of using resin for acetic acid removal from biomass hydrolysates. Their results showed that the membrane exhibited larger throughputs and reduced product loss.

- Membrane Distillation:

The membrane distillation process has received a lot of attention due to its promising applications in many separation areas. The membrane distillation (MD) is essentially a thermally driven separation process using microporous hydrophobic membranes which operates on the principles of vapour–liquid equilibrium (VLE) under different configurations [61]. Two liquids (usually two aqueous solutions) held at different temperatures are mechanically separated by a hydrophobic membrane. The hydrophobic nature of the membrane prevents the penetration of liquid water into the membrane pores. Generally, MD process is characterized by different embodiments designed to impose a vapor pressure difference between the two membrane sides in order to drive the vapor across the membrane. Lowering the vapour pressure at the permeate side can be accomplished in four different ways: (a) direct contact membrane distillation (DCMD); (b) air gap membrane distillation (AGMD); (c) sweeping gas membrane distillation (SGMD); (d) vacuum membrane distillation (VMD) [62]. Each one of the above membrane distillation configurations has its own advantages and disadvantages depending on the feed and operating conditions. The membrane distillation can find potential PI benefits into waste water treatment, textile, pharmaceuticals, gas/liquid VOC (volatile organic compounds) removal, etc [63, 64].

2.2.2.4 Alternative Source of Energy

In recent years, there has been increasing awareness to use unconventional forms of energy to provide environmental and economic benefits. In some processes, the forms of energy used are altered to improve the process performance for e.g., centrifugal forces are used in place of gravitational forces, use of microwave dielectric heating, utilising electric fields and arcs, etc. Most of these techniques can

be energy extensive but the PI benefits offered makes them more economical than the conventional forms of energy. Another potential lies in using the renewable forms of energies such as the solar energy to reduce the green house gas emissions. This technique has been utilised by Pohlman et al [65] in cyclo addition reaction of carbonyl compounds to an olefin in solar furnace reactor. Peill and Hoffman [66] used solar powered fiber optic reactor for the oxidation of 4-cholorophenol.

Chapter 3 Computational Fluid Dynamics

3.1 Introduction

The conventional approach of designing any chemical engineering unit operation or unit process, involves the following steps. Firstly a set of assumptions are made on the basis of which the equations of conservation of mass, momentum and energy are written. These differential equations are then integrated describing relation between the physical and operating parameters with the performance of the equipment. In order to write these conservation equations it is vital to understand the flow profile or velocity map inside the equipment to be designed. But traditionally it was not possible to find the complete velocity map of the equipment hence, various approximations and assumptions were made while designing any reacting or non reacting vessel. A classical example of such assumptions used in chemical engineering design is the concept of residence time distribution (RTD) used to describe the flow pattern within the chemical reactor.

The concept of residence time distribution introduced by Levenspiel [67] has been extensively used by engineers in chemical reactor design [67]. In this approach rigorous experimentation must be performed to find accurate RTD of the system.

Knowing the RTD one can calculate the overall conversion of the reactor. But performing rigorous experiments is some times not possible. Also there are other challenges in this approach such as the accuracy of the results, the complexity in the flow patterns etc. But with the availability of the new generation powerful computers these challenges can now be dealt with very little computation using computational fluid dynamics (CFD) to provide a complete velocity map and accurate RTD of the system.

It was in early 19th century that Navier (1827), Poisson (1831) and Stokes (1845) derived the fluid flow equation commonly known as the Navier-Stokes equation, which forms the basis for CFD calculations. Before the availability of powerful computer it was not possible to attain the numerical solution of the Navier-stokes equation. But since the introduction of powerful computers various advanced numerical techniques have been proposed and implied to analytically solve the Navier-Stoke equation providing useful tool to resolve the flow profiles associated in complex geometries.

Computational fluid dynamics is the analysis of the systems involving fluid flow, heat transfer and associated phenomena such as the chemical reactions by means of computer-based simulation [68]. According to Harris et al [69] “Computational Fluid Dynamics (CFD) is a discipline that encompasses the numerical solution of the equations of motion (mass, momentum and energy) in a flow geometry of interest, together with subsidiary sets of equations reflecting the problem at hand.” He further describes there are three sets of subsidiary equations that are normally incorporated in the CFD flow modelling, namely equations describing turbulence quantities, chemical species and equations of multiphase flow [69]. Predominantly CFD was extensively utilized by aerospace industry in design, research and development and manufacture of aircrafts and jet engines. In past few decades, CFD has been increasingly used to resolve wide range of industrial [70] and fundamental problems.

3.2 Pre-analysis

The quality of the results obtained from the CFD simulations is entirely depended on the ground work performed by the user in pre-analysing the problem. Before performing any CFD work on a problem, user need to make appropriate assumptions to reduce the complexity of the problem to a manageable level without affecting the

accuracy and adequacy of the results. This requires logically breaking down the problem into its physical and chemical phenomena.

The first decision that must be made is whether the problem or the equipment can be resolved in two dimensions or it requires to be formulated in 3D. One must be aware that three dimensional problem will demand much higher computational power. Some times the flow may be speculated to be symmetrical. In such cases only half of the geometry is computed and the results can be mirrored to the other half along the axis of symmetry. Determining the geometrical configuration is vital with the point of view of practicality and manageability of computation required to resolve the problem.

Once the geometrical configuration is decided the other assumptions relating to the process must be made. This includes the decision as to whether the flow incorporates effective turbulences, chemical reactions, mass transfer phenomena, the importance of heat transfer mechanisms, the existence of multiphase's and the formulations to be utilised to resolve them. To summarize, before generating any information using CFD, the user must entirely be aware of the physical phenomena of the process and take appropriate measures to simplify the problem without affecting the accuracy of the results.

3.3 Pre-processing

Once the pre-analysis is performed and an appropriate geometrical configuration is selected, flow field is then discretized into a computational domain. The discretized flow field is commonly known as the grid/mesh. It is defined as “a set of points distributed over a calculation field for a numerical solution of a set of partial differential equations (PDEs) [71].” Mesh is generally generated using CAD based software such as GAMBIT. It is vital to generate appropriate mesh to facilitate accurate numerical solution. While generating a mesh there are various factors that needs to be considered such as:

- Mesh should be sufficiently dense but practically computable.
- Grid spacing should be smooth.
- Discontinuities or skewness should be avoided.
- Appropriate choice of the grid should be made.

- Well organised grid is desirable.

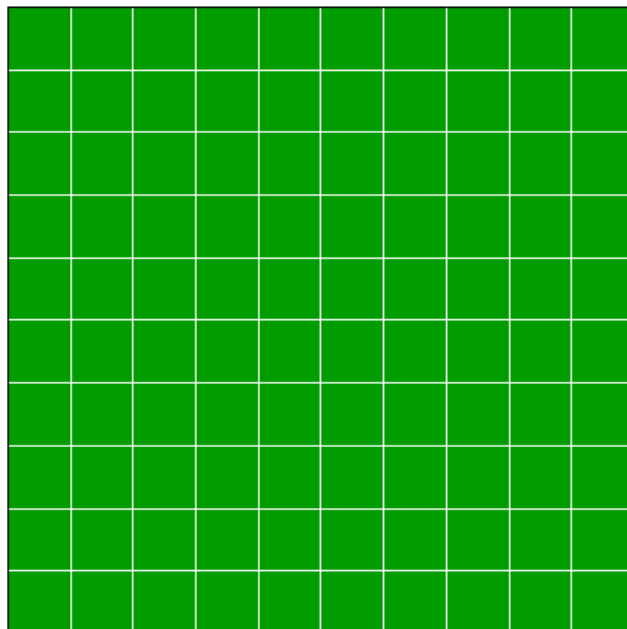
Taking into account the above factors either of the two types of the grids can be generated; namely structured grid or unstructured grid.

3.3.1 Structured grid

When a grid is formed by intersection of curvilinear co-ordinate surfaces the mesh is called as the structured mesh. In 2D sets of points form quadrilateral structured cells as shown in Figure 4. Whereas in 3D hexahedral cells with non-planar sides are computed to form structured grid. Also in structured grid all interior nodes have equal number of adjacent elements.

3.3.2 Unstructured grid

Essentially an unstructured grid consists of triangle and tetrahedral elements in 2D and 3D respectively. Also quadrilateral, hexahedral or elements of any shape can be incorporated in an unstructured grid. The unstructured grid allows any number of elements to meet at a node. A schematic of a 2D and 3D unstructured grid is shown in Figure 5.



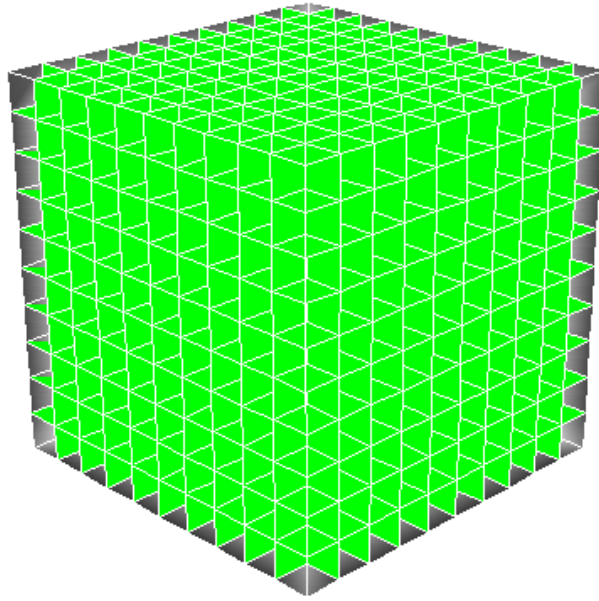
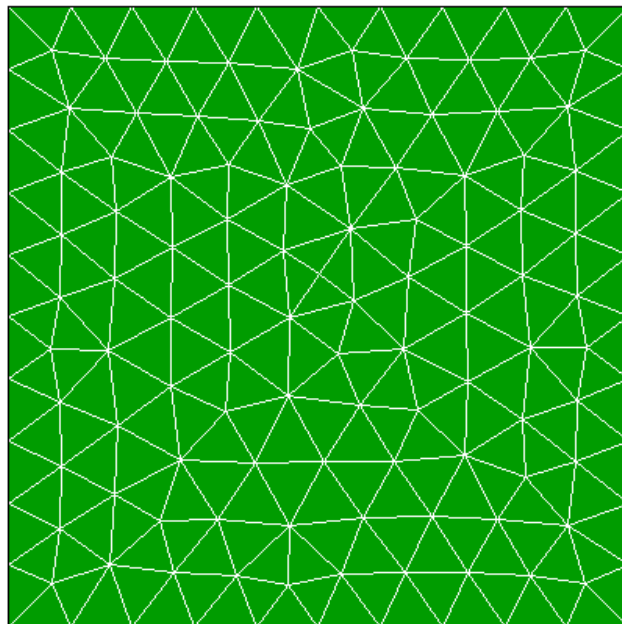


Figure 4 Schematic of structured meshing scheme



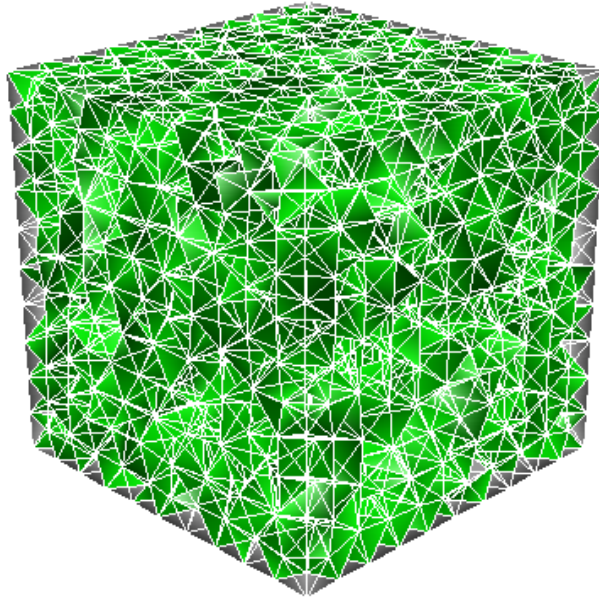


Figure 5 Schematic of unstructured meshing scheme

3.4 CFD codes

A variety of CFD codes have been developed and utilized for a broad spectrum of applications. Salient feature of the CFD codes have been reviewed by various researchers and detailed in open literature [72-74]. In general all the CFD codes include three key elements:

1. Pre-processor
2. Solver
3. Post-processor

As described in section 3.3 pre-processing includes defining a computational domain and generating an appropriate grid/mesh. Whereas pre-processor also defines boundary conditions at cells which coincide with or touch the domain boundary. One of the pre-processor commonly associated with FLUENT solver is GAMBIT, which was used in this work.

Essentially, the solver solves the formulated partial difference equations (PDE) using any of the three numerical solution techniques:

1. Finite difference method
2. Finite element method
3. Finite volume method

Principles and methodologies of these techniques are further detailed in section 3.6. Finally, CFD codes are also equipped with graphic capabilities to visualise the data. User has a variety of information which can be visualised in either 2D or 3D such as, vector plots, contours and surface plots. Various techniques have also been developed to generate animations enabling a dynamic result display. Furthermore advanced techniques have been embedded into CFD codes which can generate useful raw data as well. In this study, FLUENT release 6.3 was used.

3.5 Conservation equations

The conservation laws of physics are represented mathematically in the form of governing conservation equations in CFD. This includes the conservation of mass (continuity), momentum (Newtons Second Law) and energy (first law of Thermodynamics). We will consider a very small element of fluid as shown in Figure 6 and derive generic forms of these equations.

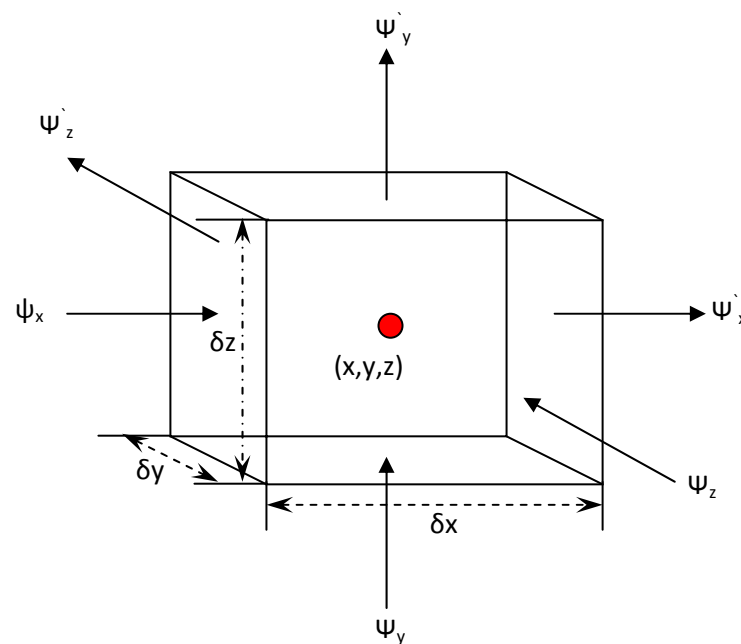


Figure 6 Element of fluid

Where ψ and ψ' are the scalar properties of the fluid entering and exiting the fluid element in x,y and z direction respectively. The generic forms of the equations are detailed by Versteeg and Malalaskera ; and Ranade. [68, 75].

3.5.1 Continuity equation

Equation of continuity is derived from the law of conservation of mass. A mass balance for a species k yields [75]:

$$\frac{\partial}{\partial t}(\rho x_k) + \nabla \cdot (\rho U x_k) = -\nabla \cdot (J_k) + S_k \quad 1$$

Where, x_k is mass fraction of species, ρ and U are density and velocity of the fluid respectively. S_k is the source term and represents the net gain of mass of species k because of a chemical reaction or interphase transfer per unit volume. J_k is rate of diffusive flux of species k (mass per unit area per unit time) and is given by:

$$J_k = -\rho D_k \nabla x_k \quad 2$$

Where, D_k is diffusivity of species k in the fluid. Substitution of equation 2 in equation 1 gives:

$$\frac{\partial}{\partial t}(\rho x_k) = -\nabla \cdot (\rho U x_k) + \nabla \cdot (\rho D_k \nabla x_k) + S_k \quad 3$$

where, the left-hand side, LHS, of equation 3 represents the rate of accumulation of species k and on the RHS, the first and second terms depict the rate of gain of species k due to convection and diffusion respectively.

Consequently for all the species in the system, equation 3 can be rewritten as;

$$\frac{\partial}{\partial t}(\rho) + \nabla \cdot (\rho U) = \sum_k S_k \quad 4$$

3.5.2 Momentum equation

The momentum equation for the fluid particle is derived from the **Newton's Second Law** of motion. It states "Observed from an inertial reference frame, the net force on a particle is proportional to the time rate of change of its linear momentum." Mathematically this can be written as [76]:

$$\frac{\partial}{\partial t}(\rho U) + \nabla \cdot (\rho U U) = -\nabla p - \nabla \cdot \tau + \rho g + F \quad 5$$

Where, the first and second term in LHS represents the rate of increase and change in the momentum per unit volume respectively. RHS represents the sum of the surface and body forces.

For Newtonian fluids, the stress tensor τ in equation 5 is expressed as [75, 76]

$$\tau_{ij} = -\mu(\nabla U + \nabla U^T) + \frac{2}{3}\mu\delta_{ij}(\nabla \cdot U) \quad 6$$

Where, μ is viscosity of the fluid, δ_{ij} is Kronecker delta ($\delta_{ij} = 0$ if $i \neq j$ and $\delta_{ij} = 1$ if $i=j$).

Three components of momentum balances can be obtained by substituting equation 6 in equation 5:

x – momentum	$\frac{\partial}{\partial t}(\rho U_x) + \nabla \cdot (\rho U U_x) = -\frac{\partial p}{\partial x} + \nabla \cdot (\mu \nabla U_x) + S_{mx}$
y – momentum	$\frac{\partial}{\partial t}(\rho U_y) + \nabla \cdot (\rho U U_y) = -\frac{\partial p}{\partial y} + \nabla \cdot (\mu \nabla U_y) + \rho g_y + F_y$
z – momentum	$\frac{\partial}{\partial t}(\rho U_z) + \nabla \cdot (\rho U U_z) = -\frac{\partial p}{\partial z} + \nabla \cdot (\mu \nabla U_z) + \rho g_z + F_z$

Where, $S_{mx} = \rho g_x + F_x$, $S_{my} = \rho g_y + F_y$ and $S_{mz} = \rho g_z + F_z$.

3.5.3 Energy equation

Using the first law of thermodynamics, the equation of conservation of energy is presented. In principle this equation is formulated with the following principle:

Rate of increase of energy of fluid particle	=	Net rate of heat added to fluid particle	+	Net rate of work done
---	---	---	---	--------------------------

Numerically this can be represented as [76]

$$\frac{\partial}{\partial t}(\rho E) = -\nabla \cdot (U(\rho E + p)) + k\nabla^2 T - (\tau : \nabla U) - \nabla \cdot \left(\sum_k H_k J_k \right) + S_h \quad 7$$

Here, E internal energy is calculated by,

$$E = H - \frac{p}{\rho} + \frac{U^2}{2} \quad 8$$

Further H, specific enthalpy is calculated using following equation,

$$H = \sum_k x_k H_k \quad 9$$

For ideal gas E and H can be written as,

$$E = C_v(T - T_o) \quad 10$$

and,

$$H_k = C_{pk}(T - T_o) \quad 11$$

Finally substituting equation 10 and 11 in equation 7 we get,

$$\frac{\partial}{\partial t}(\rho C_v T) = -\nabla \cdot (U \rho C_v T) + k \nabla^2 T - \nabla \cdot (U p) - (\tau : \nabla U) - \nabla \cdot \left(\sum_k C_{pk}(T - T_o) J_k \right) + S_h \quad 12$$

3.6 Generic transport equations

Properties of the conservation equations of mass momentum and energy can be rewritten in the form of a general scalar quantity Ψ as [77]

$$\frac{\partial}{\partial t}(\rho \Psi) + \nabla \cdot (\rho U \Psi) = \nabla \cdot (\rho \Lambda \nabla \Psi) + S_\Psi \quad 13$$

Where, Λ and S_Ψ are diffusivity and corresponding source term for scalar quantity Ψ respectively. Solution to these conservation equations is not easy. As described in the section above, these conservation equations are solved in CFD using numerical techniques which are detailed in the section 3.7. The corresponding variables for the scalar quantities of equation 13 are detailed in the Table 2 below:

Table 2 Conservations equations expressed inform of general scalar quantity

Scalar	Ψ	Λ	S_Ψ
Continuity equation	X_k	D_k	S_k
x – momentum	U_x	μ/ρ	$-\frac{\partial p}{\partial x} + S_{mx}$
y- momentum	U_y	μ/ρ	$-\frac{\partial p}{\partial y} + S_{my}$
z – momentum	U_z	μ/ρ	$-\frac{\partial p}{\partial z} + S_{mz}$
Energy equation	$C_v T$	$k/C_v \rho$	$-\nabla \cdot (U p) - \tau : \nabla U - \nabla \cdot \left(\sum_k H_k J_k \right) + S_h$

3.6 Numerical techniques

Mainly three numerical techniques are available to obtain simple algebraic equations from the set of complex PDEs. Either of the finite difference, finite element and

finite volume are used to discretize the computational domain and approximate unknown variable using simple functions [77]. The main difference between all three methods is the methodology by which the flow variables are approximated [68].

3.6.1 Finite difference method

In the finite difference method, the unknown variable is described by mean of the point samples at the nodes of a grid co-ordinate lines. An application of truncated Taylor series to these grid co-ordinates yields number of algebraic equations. This can generally be solved using any of the elimination techniques [78, 79].

3.6.2 Finite element method

In the finite element method, the computational domain is divided into a number of finite elements. Simple piecewise functions (e.g. linear or quadratic) are applied to these elements to describe the local variations of the unknown flow variables. This substitution is an error and hence residual is defined to measure the errors. Then these residuals are multiplied by a set of weighting functions and integration. Resulting set of algebraic equations are then solved similar to finite difference method. Before finding application into CFD this technique was predominantly used for stress analysis in structural engineering problems [80].

3.6.3 Finite volume method

The most common numerical technique that is widely used in modern CFD codes is the finite volume method. It has particular advantage over other numerical technique that it can ensure the conservation of various properties in a control volume. Firstly in this technique the computational domain is divided into small number of finite volumes. Then a formal integration of the governing equations of the fluid flow is performed over all the finite volumes. Then after various finite difference type approximations are substituted for the terms in the integrated equation. This results into a series of algebraic equations which are finally solved iteratively.

To explain the steps involved in calculations using the finite volume method, a simple example of steady state diffusion is considered. Governing equation of steady diffusion is derived from the previously described generic transport equation 13 by deleting the transient and convective terms is given as,

$$\Delta \cdot (\rho \Lambda_{\psi} \Delta \psi) + S_{\psi} = 0 \quad 14$$

This equation if integrated over all the control volume in the computational domain, which forms a key step of the finite volume method that distinguishes it from all other techniques. Following form of integrated equation is obtained,

$$\int_{cv} \nabla \cdot (\Lambda \rho \nabla \psi) dV + \int_{cv} S_{\psi} dV = 0 \quad 15$$

Applying Gauss's divergence theorem (for a vector \mathbf{b}):

$$\int_{cv} \nabla \cdot \mathbf{b} dV = \int_A \hat{\mathbf{n}} \cdot \mathbf{b} dA \quad 16$$

Equation 15 can be rewritten as:

$$\int_{cv} \nabla \cdot (\Lambda \rho \nabla \psi) dV + \int_{cv} S_{\psi} dV = \int_A \hat{\mathbf{n}} \cdot (\Lambda \rho \nabla \psi) dA + \int_{cv} S_{\psi} dV = 0 \quad 17$$

Now consider a 3D finite volume as shown in Figure 6 with the cell centre P having six neighbouring nodes identified as north, south, east, west, top and bottom. Where notations, n, s, e, w, t and b represents the faces in north, south, east, west, top, and bottom directions respectively.

Rewriting equation 14 in three dimensional form gives:

$$\frac{\partial}{\partial x} \left(\Lambda \frac{\partial \psi}{\partial x} \right) + \frac{\partial}{\partial y} \left(\Lambda \frac{\partial \psi}{\partial y} \right) + \frac{\partial}{\partial z} \left(\Lambda \frac{\partial \psi}{\partial z} \right) + S = 0 \quad 18$$

Integrating equation 18 over the control volume gives

$$\left[\Lambda_e A_e \left(\frac{\partial \psi}{\partial x} \right)_e - \Lambda_w A_w \left(\frac{\partial \psi}{\partial x} \right)_w \right] + \left[\Lambda_n A_n \left(\frac{\partial \psi}{\partial y} \right)_n - \Lambda_s A_s \left(\frac{\partial \psi}{\partial y} \right)_s \right] + \left[\Lambda_t A_t \left(\frac{\partial \psi}{\partial z} \right)_t - \Lambda_b A_b \left(\frac{\partial \psi}{\partial z} \right)_b \right] + \bar{S} \Delta V = 0 \quad 19$$

Above equation represents the balance of the generation of Ψ in a control volume and fluxes through its cell faces. Using the approximation we can write the expression for the flux through control volume faces as:

$$f_n = \Lambda_n A_n \left(\frac{\partial \psi}{\partial y} \right)_n = \Lambda_n A_n \frac{(\psi_N - \psi_P)}{\delta y_{PN}}$$

$$f_s = \Lambda_s A_s \left(\frac{\partial \psi}{\partial y} \right)_s = \Lambda_s A_s \frac{(\psi_P - \psi_S)}{\delta y_{SP}}$$

$$f_e = \Lambda_e A_e \left(\frac{\partial \psi}{\partial x} \right)_e = \Lambda_e A_e \frac{(\psi_E - \psi_P)}{\delta x_{PE}}$$

$$f_w = \Lambda_w A_w \left(\frac{\partial \psi}{\partial x} \right)_w = \Lambda_w A_w \frac{(\psi_P - \psi_W)}{\delta x_{WP}}$$

$$f_t = \Lambda_t A_t \left(\frac{\partial \psi}{\partial z} \right)_t = \Lambda_t A_t \frac{(\psi_T - \psi_P)}{\delta z_{PT}}$$

$$f_b = \Lambda_b A_b \left(\frac{\partial \psi}{\partial z} \right)_b = \Lambda_b A_b \frac{(\psi_P - \psi_B)}{\delta z_{BP}}$$

$$\bar{S} \Delta V = S_u + S_p \Psi_P$$

Substituting the above equations in equation 18 gives the discretized form of the equation;

$$\left[\Lambda_e A_e \frac{(\psi_E - \psi_P)}{\delta x_{PE}} - \Lambda_w A_w \frac{(\psi_P - \psi_W)}{\delta x_{WP}} \right] + \left[\Lambda_n A_n \frac{(\psi_N - \psi_P)}{\delta y_{PN}} - \Lambda_s A_s \frac{(\psi_P - \psi_S)}{\delta y_{SP}} \right] + \left[\Lambda_t A_t \frac{(\psi_T - \psi_P)}{\delta z_{PT}} - \Lambda_b A_b \frac{(\psi_P - \psi_B)}{\delta z_{BP}} \right] + (S_u + S_p \Psi_P) = 0 \quad 20$$

Equation 20 can be rearranged as

$$a_p \Psi_P = a_w \Psi_W + a_e \Psi_E + a_s \Psi_S + a_n \Psi_N + a_b \Psi_B + a_t \Psi_T + S_u$$

Where,

$$a_w = \frac{\Lambda_w A_w}{\delta x_{WP}}$$

$$a_e = \frac{\Lambda_e A_e}{\delta x_{PE}}$$

$$a_s = \frac{\Lambda_s A_s}{\delta y_{SP}}$$

$$a_n = \frac{\Lambda_n A_n}{\delta y_{PN}}$$

$$a_b = \frac{\Lambda_b A_b}{\delta x_{BP}}$$

$$a_t = \frac{\Lambda_t A_t}{\delta x_{PT}}$$

$$a_p = a_w + a_e + a_s + a_n + a_b + a_t - S_p \quad 21$$

Several algorithms have been proposed to elaborate these nodal values they include central differencing scheme (CDS), upwind scheme, and QUICK (quadratic upstream interpolation for convective kinetics). Versteeg and Malalasekera have detailed them [68].

Solution for the general scalar transport equation will be obtained using the above described procedure. However there are more complexities associated with the pressure source terms of the momentum equation that requires special treatment. The problem lies in the manner in which the pressure is stored with velocity in the grid. If pressure and velocity both are defined at the nodes of an ordinary control volume highly non-uniform pressure field can act as a uniform pressure field in the momentum equation [68]. This type of grids is referred to as “co-located” grids. However, co-located grids fail to pass so-called ‘checker-board’ pressure test explained by Varsteeg and Malalaskera [68].

A remedy of this problem is to assign different locations for velocity and pressure. Such an arrangement is termed as “staggered grid”. In this arrangement the scalar variables such as pressure, temperature, density etc. are assigned to ordinary nodal points and velocity components are calculated on the staggered grids centred on the cells faces. Schematic of a staggered grid is shown in Figure 7 wherein the scalar variables (pressure and temperature) are stored at nodes marked (•) and the velocities are indicated by arrows and are stored at cell faces. To identify the locations of scalar and vector quantities in a staggered grid arrangement a special notation system is adopted [68]. The dashed lines in Figure 7 identify pressure field and have been indexed using capital I and J. The unbroken lines that construct the scalar cell faces are marked by i and j. A general control volume P of co-located arrangement is identified by indices (I, J).

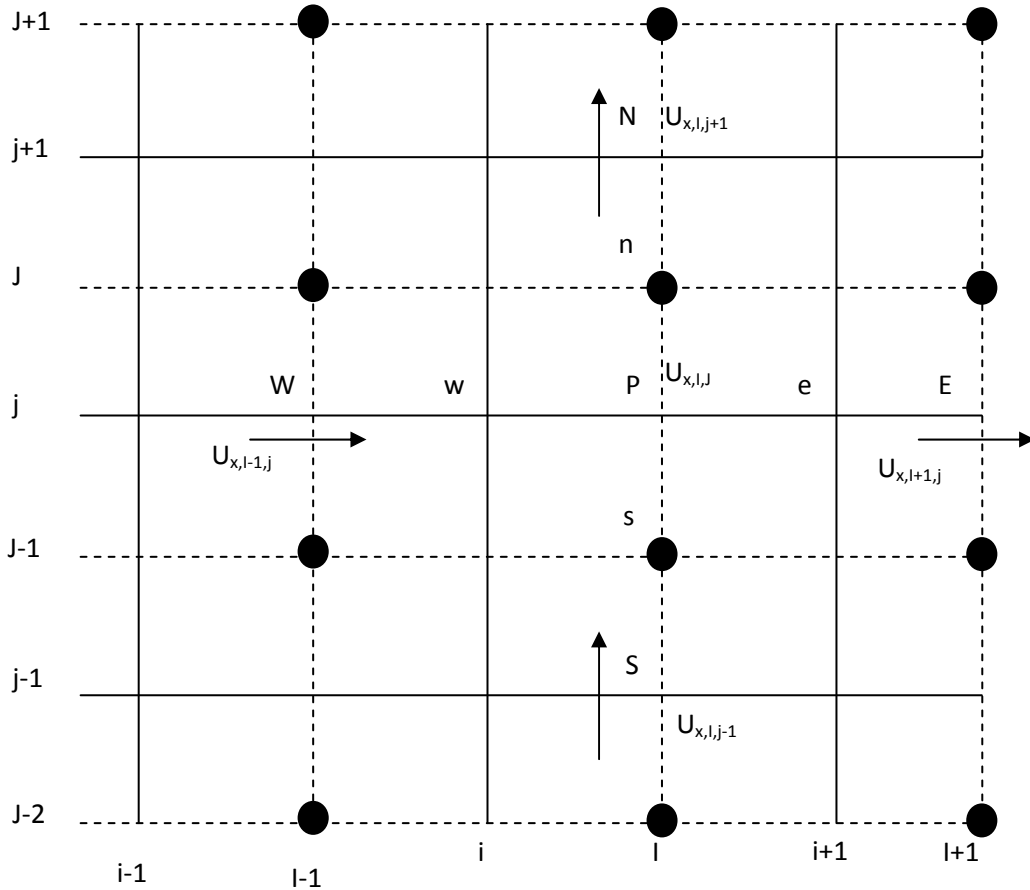


Figure 7 Schematic of staggered grid

Discretized v momentum equation is obtained by applying the generic transport equation on the new co-ordinate system. V-momentum equation is given as:

$$a_{I,j}v_{I,j} = \sum a_{nb} + v_{nb} + (p_{I,J-1} - p_{IJ})A_{I,j} + b_{I,j} \quad 22$$

Where,

$$b_{I,j} = \bar{S}\Delta V_u$$

The values of the unknown a_{ij} and a_{nb} are approximated using any of the differencing schemes explained in the section above. The resulting coefficient will contain convective flux per unit mass F and diffusive conductance D . Which are rewritten as:

$$F_e = \frac{F_{i+1,J} + F_{i+1,J-1}}{2} = \frac{1}{2} \left[\left(\frac{\rho_{i+1,J} + \rho_{I,J}}{2} \right) u_{i+1,J} + \left(\frac{\rho_{I,J} + \rho_{I-1,J}}{2} \right) u_{i,J} \right] \quad 23$$

$$F_w = \frac{F_{i,J} + F_{i,J-1}}{2} = \frac{1}{2} \left[\left(\frac{\rho_{I,J} + \rho_{I-1,J}}{2} \right) u_{i,J} + \left(\frac{\rho_{I-1,J} + \rho_{I-2,J}}{2} \right) u_{i-1,J} \right] \quad 24$$

$$F_s = \frac{F_{I,j-1} + F_{I,j}}{2} = \frac{1}{2} \left[\left(\frac{\rho_{I,J} + \rho_{I-1,J}}{2} \right) v_{i,J} + \left(\frac{\rho_{I-1,J} + \rho_{I-2,J}}{2} \right) v_{i-1,J} \right] \quad 25$$

$$F_n = \frac{F_{I,j} + F_{I,j+1}}{2} = \frac{1}{2} \left[\left(\frac{\rho_{I,J+1} + \rho_{I,J}}{2} \right) v_{I,J+1} + \left(\frac{\rho_{I-1,J+1} + \rho_{I-1,J}}{2} \right) u_{i-1,j+1} \right] \quad 26$$

$$D_e = \frac{\Lambda_{I,J}}{x_{i+1} - x_i} \quad 27$$

$$D_w = \frac{\Lambda_{I-1,J}}{x_i - x_{i-1}} \quad 28$$

$$D_s = \frac{\Lambda_{I-1,J} + \Lambda_{I,J} + \Lambda_{I-1,J-1} + \Lambda_{I,J-1}}{4(y_i - y_{i-1})} \quad 29$$

$$D_n = \frac{\Lambda_{I-1,J+1} + \Lambda_{I,J+1} + \Lambda_{I-1,J} + \Lambda_{I,J}}{4(y_{j+1} - y_j)} \quad 30$$

Similarly, u-momentum is resolved details of which can be found in the text by Versteeg and Malalasekera [68]. As it can be seen from the above equations additional unknowns are produced in the form of pressure nodal values. Therefore, an additional scheme is needed to calculate the pressure field. The most popular algorithm for the velocity-pressure coupling is called SIMPLE (Semi-Implicit Method for Pressure-Linked Equations) [81, 82]. This algorithm essentially involves a trial and error procedure for evaluating pressure field in a staggered grid arrangement. The scheme progressively corrects the previously assumed pressure field. There are a number of variants of SIMPLE, including SIMPLER (SIMPLE Revised), SIMPLEC (SIMPLE Consistent) and PISO (Pressure Implicit with Splitting of Operators) [68].

3.7 Multiphase flow modelling

In a large number of equipments of engineering problems there are more than one phases involved. Thus to understand the hydrodynamic behaviour of such systems it is vital to take into account the interaction between these phases. Whenever there are multiple phases existing, from the physical behaviour of a phase it can be classified as either to be continuous phase or dispersed phase.

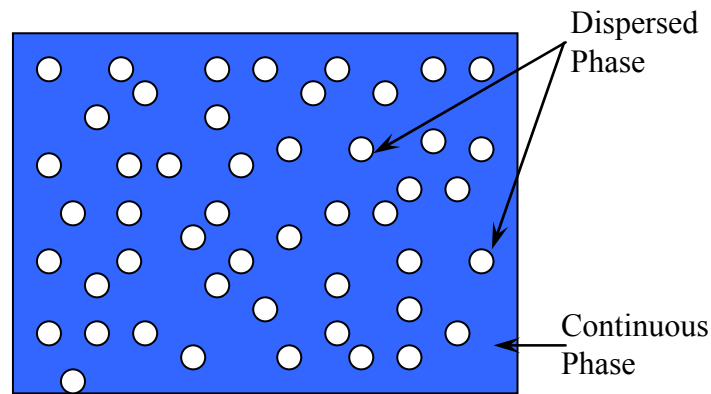


Figure 8 General form of multiphase systems

A continuous phase is materially connected within its entirety. Whereas the dispersed phase exists in the form of micro, maso or macro scale pockets in the continuous phase. It is vital to have some subsidiary sets of equations derived which can predict the behaviour of multiple phases.

In general there are two approaches which have been derived to model the multiphase flow:

1) Eulerian-Langrangian approach.

In the Eulerian-Langrangian approach the fluid phase is treated as a continuum by solving the time-averaged Navier-Stokes equations, while the dispersed phase is solved by tracking a large number of particles, bubbles, or droplets through the calculated flow field. The dispersed phase can exchange momentum, mass, and energy with the fluid phase [83].

The salient feature of this approach is that the dynamics of the individual bubble or particles can be tracked throughout the domain. Whereas, in some cases where the dispersed phase have high concentrations simulations can become highly memory intensive and unstable. Typically this approach applied in modelling of spray dryers, coal and liquid fuel combustion, and some particle-laden flows. And this approach is not suitable for applications such as fluidised beds, liquid-liquid mixtures etc.

2) Eulerian-Eulerian approach.

In the Eulerian-Eulerian approach, both discrete and continuous phases are treated mathematically as interpenetrating continua and ensemble averaged equations for individual phases are solved in the Eulerian frame of reference [84, 85]. Since the

volume of a phase cannot be occupied by the other phases, the concept of phasic volume fraction is introduced [83]. These volume fractions are assumed to be continuous functions of space and time and their sum is equal to one. The conservation equation for each phase are derived to obtain a set of equations, which have similar structure for all phases. Any interaction between the inter-penetrating phases is accounted for using closure laws obtained from the empirical laws. This approach does not provide any information about the hydrodynamics of individual bubbles but it requires significantly fewer computational resources, which makes it more effective in simulating large industrial reactors.

3.7.1 Flow regimes in multiphase processes

A variety of flow regimes are observed in the multiphase vessels. Primarily, any observed flow regime is depended of the fluid velocities of the individual phases. But some studies have also related the vessel geometry configuration with the observed flow patterns in multiphase equipments [86, 87]. Some of the general flow regimes observed in multiphase systems are shown in Figure 9

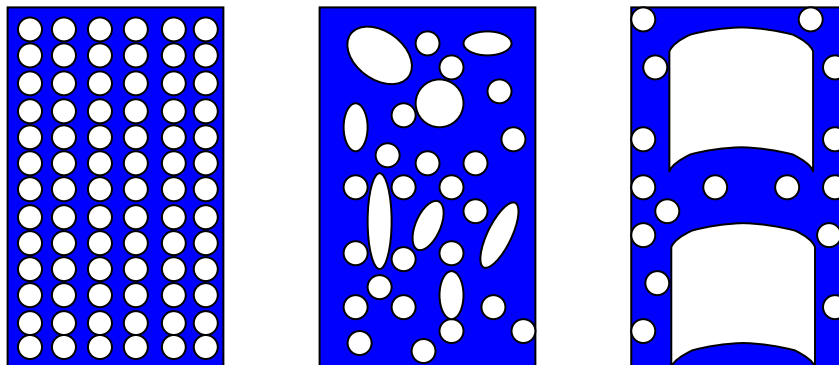


Figure 9 Flow regimes in multiphase systems

All of the above stated flow regimes occur in engineering problems either independently or simultaneously and it is vital to identify the flow regime before selecting an appropriate multiphase model. This is because each of them will require special considerations and appropriate assumptions for simplifying the problem.

In the homogenous bubbly flow regime, the hydrodynamic characteristics are entirely dependent on the individual bubbles and interaction between the bubbles and the continuous fluid. For this regime, there are numerous well established correlations available in the literature that can predict bubble characteristics. Thus

either of the Eulerian-Eulerian or Eulerian-Lagrangian approach can be utilised to evaluate the flow in the homogenous bubbly flow regime.

In the churn turbulent regime, there are a wide range of bubble sizes present. Thus to characterise the flow in this regime, the overall regime can be subdivided into groups of the bubble sizes and modelled using Eulerian-Lagrangian approach [84]. However, simulating the slug flow regime is different and requires surface tracking methods such as Volume of Fluid (VOF) due to existing sharp interfaces [88].

3.7.2 Eulerian Eulerian model

In the Eulerian-Eulerian multiphase model each of the phases present is treated as interpenetrating continua. Applying the concept of phasic volume fraction averaged conservation equations of mass, momentum and energy are obtained which are shown in Table 3 below. This method is not suitable for predicting flows in which interface tracking is significant. For example, this method cannot predict the shape and size of bubbles in bubble column, whereas for applications like fluidised bed this method is beneficial.

Table 3 Governing equations of Eulerian Eulerian Model

No	Equation name	Equation
1	Continuity equation	$\frac{\partial}{\partial t}(\varepsilon_k \rho_k) + \nabla \cdot (\varepsilon_k \rho_k \mathbf{U}_k) = \sum_{\substack{j=1 \\ j \neq k}}^n \dot{m}_{jk}$ $\sum_{k=1}^n \varepsilon_k = 1.0$
2	Momentum equation	$\frac{\partial}{\partial t}(\varepsilon_k \rho_k \mathbf{U}_k) = -\nabla \cdot (\varepsilon_k \rho_k \mathbf{U}_k \mathbf{U}_k) - \varepsilon_k \nabla p - \nabla \cdot (\varepsilon_k \boldsymbol{\tau}_k) + \varepsilon_k \rho_k \mathbf{g} + \mathbf{F}_k + \mathbf{F}$ $\mathbf{F} = \mathbf{F}_{\text{lift}} + \mathbf{F}_{\text{vm}}$
3	Lift force	$\mathbf{F}_{\text{lift}} = \frac{1}{2} \rho_q \varepsilon_q \mathbf{U}_k - \mathbf{U}_q \times (\nabla \times \mathbf{U}_q)$
4	Virtual mass force	$\mathbf{F}_{\text{VM}} = -\frac{1}{2} \varepsilon_q \rho_q \left[\left(\frac{\partial \mathbf{U}_q}{\partial t} + \mathbf{U}_q \cdot \nabla \mathbf{U}_q \right) - \left(\frac{\partial \mathbf{U}_k}{\partial t} + \mathbf{U}_k \cdot \nabla \mathbf{U}_k \right) \right]$

		$F_k = \sum_{\substack{j=1 \\ j \neq k}}^n (K_{jk} (U_j - U_k)) + \sum_{\substack{j=1 \\ j \neq k}}^n (\dot{m}_{jk} (U_j - U_k))$
5	Momentum Exchange Term	$K_{jk} = \frac{\varepsilon_j \rho_j f_{jk}}{t_{rlx,jk}}$ $t_{rlx,jk} = \frac{\rho_j d_j^2}{18\mu_k}$ $f_{jk} = \frac{C_{D,jk} Re_{jk}}{24}$
6	Morsi- Alexander	$C_{D,jk} = a_1 + \frac{a_2}{Re_{jk}} + \frac{a_3}{Re_{jk}^2}$ $Re_{jk} = \frac{\rho_k U_j - U_k d_j}{\mu_k}$
7	Stress tensor	$-\tau_k = \mu_k (\nabla \cdot U_k + \nabla \cdot U_k^T) + \delta_{ij} (\lambda_k - \frac{2}{3} \mu_k) (\nabla \cdot U_k)$

Table 4 Constants of Morsi-Alexander drag model

Reynolds Number	a₁	a₂	a₃
0 < Re < 0.1	0	18	0
0.1 < Re < 1	3.690	22.73	0.0903
1 < Re < 10	1.222	29.1667	-3.8889
10 < Re < 100	0.6167	46.50	-116.67
100 < Re < 1000	0.3644	98.33	-2778
1000 < Re < 5000	0.357	148.62	-47500
5000 < Re < 10000	0.46	- 490.546	578700
Re ≥ 10000	0.5191	-1662.5	5416700

3.7.3 Volume of fluid model

The volume of fluid (VOF) model first developed by Hirt and Nichols [89]. It is a surface tracking technique applied to the fixed Eulerian mesh. In this method, a single set of momentum equations is shared by the fluids. The volume fraction of each fluid, in each computational cell, is tracked throughout the domain [90]. The VOF formulation is particular advantageous in interface tracking. It is also relatively simple and accurate to apply to boundary fitted grids and accommodates the break-up and formation of interfaces. The governing equations for the VOF model are shown in Table 5:

Table 5 Governing equations of VOF model

No	Equation Name	Equation
1	Equation of Continuity	$\frac{\partial \rho}{\partial t} + \nabla \cdot (\rho \vec{v}) = 0$
2	Momentum Equation	$\frac{\partial(\rho \vec{v})}{\partial t} + \nabla \cdot (\rho \vec{v} \vec{v}) = -\nabla p + \nabla \cdot [\mu(\nabla \vec{v} + \nabla \vec{v}^t)] + \rho \vec{g} + \vec{F}$
3	Volume Fraction Equation; If for qth fluids volume fraction is α_q then; For $\varepsilon_q = 0$; cell is empty (for qth fluid) For $\varepsilon_q = 1$; cell is full (for qth fluid) For $0 < \varepsilon_q < 1$; cell contains interface between qth fluid and other fluids.	$\frac{1}{\rho_q} \left[\frac{\partial}{\partial t} (\varepsilon_q \rho_q) + \nabla \cdot (\varepsilon_q \rho_q \vec{v}_q) = s_{\varepsilon_q} + \sum_{q=1}^n (\dot{m}_{pq} - \dot{m}_{qp}) \right]$
	Continuum	$\sum_{q=1}^n \varepsilon_q = 1$
	surface force (CSF) Model; Surface Tension	$\frac{\varepsilon_q^{n+1} \rho_q^{n+1} - \varepsilon_q^n \rho_q^n}{\Delta t} V + \sum_f (\rho_q^{n+1} u_f^{n+1} \varepsilon_{q,f}^{n+1}) = \left[\sum_{p=1}^n (\dot{m}_{pq} - \dot{m}_{qp}) \right] V$
4	Continuum surface force (CSF) Model; Surface Tension	$F_{vol} = \sigma_{ij} \frac{\rho K_s \nabla \varepsilon_i}{\frac{1}{2}(\rho_i + \rho_j)}$
5	Courant number	$Co = \frac{\Delta t}{\Delta x_{cell} / v_{fluid}}$

3.7.4 Selection of multiphase model

A wide range of chemical engineering equipment involve the flow of multiple phases in the form of free surfaces. Various methods are available for dynamic characterization free surfaces such as the front tracking, level set, marker particle, shock capturing and volume of fluid (VOF) [90]. But they all have their merits and drawbacks as shown in Table 6. Due to its simplicity and straight forward application to breaking and coalescing surfaces, the VOF method as selected for analyzing all three reactor types. In order to conduct a comparative assessment, the EE model was also used for one of the reactor types (namely, the rotating disc reactor).

3.8 Summary

An overview of the various methodologies and models of CFD has been presented in this chapter. The numerical solution from the CFD calculations is entirely dependent on the user's understanding of the physics of the process. For example, in order to determine an appropriate multiphase model, the user must roughly know *a priori* the flow regime expected under given operating and process conditions. Since all of the three reactor types to be investigated in this study have the presence dynamically coalescing and breaking interfaces, the VOF method emerged as the model of choice for the current study.

Table 6 Comparison of multiphase models [90].

No	Method	Advantages	Disadvantages
1	Front tracking	Extremely accurate Robust Accounts for substantial topology changes in interface	Mapping of interface mesh onto Eulerian mesh Dynamic re-meshing required Merging and breakage of interfaces requires sub-grid model
2	Level set	Easy to implement Conceptually simple	Limited accuracy Loss of mass (volume)
3	Shock capturing	Straightforward implementation Abundance of advection schemes is available	Numerically diffusive Limited or small discontinuities Fine grids required
4	Marker particle	Extremely accurate Robust Accounts for substantial topology changes in interface	Computationally expensive Re-distribution of marker particles required
5	VOF	Conceptually simple Straightforward extension to three dimensions Merging and breakage of interfaces occurs automatically	Numerically diffusive Limited accuracy

6	PLIC VOF	Relatively simple and accurate Merging and breakage of interface occurs automatically	Difficult to implement in three dimensions Extension to boundary fitted grids very difficult
7	Compressive VOF	Relatively simple and accurate Easily adaptable to boundary fitted grids Merging and breakage of interface occurs automatically	Requires very low Courant numbers else becomes inaccurate or unstable

3.9 Nomenclature

A_j	area of j th face of control volume, m^2
C_p	mass ratio (mass of particle/mass of continuous phase)
d	diameter, m
D_k	diffusivity of k th species in bulk fluid, $m^2 s^{-1}$
E	internal energy, $J kg^{-1}$
f_{jk}	drag function
F	force, N
F_{lift}	lift force, N
F_{VM}	virtual mass force, N
$g_{o,ss}$	radial distribution function
H	enthalpy, $J kg^{-1}$
J_k	diffusive flux of k th species, $kg m^{-2} s^{-1}$
K_{jk}	momentum exchange coefficient between k th and j th phase
l	turbulence length scale (large eddies), m
\dot{m}_{jk}	rate of mass transfer from j th phase to k th phase
N	total number of control volumes
p	pressure, $N m^{-2}$
p_s	solid (granular) pressure, $N m^{-2}$
S_ψ	source term in generic transport equation
S_h	source term in energy equation – generation energy, $J m^{-3} s^{-1}$
S_k	source term in continuity equation – generation of k th species, $kg m^{-3} s^{-1}$
S_{mass}	interphase mass exchange rate from dispersed phase to continuous phase, $kg m^{-3} s^{-1}$
S_{mom}	interphase momentum exchange rate from dispersed to continuous phase, $N m^{-3}$
t	time, s

τ_{lx}	particulate relaxation time, s
T	temperature, K
U	velocity, $m\ s^{-1}$
U'	fluctuating component of velocity, $m\ s^{-1}$
U_P	fluid velocity in control volume P, $m\ s^{-1}$
$U_{b, rise}$	bubble rise velocity, $m\ s^{-1}$
V_G	gas superficial velocity, $m\ s^{-1}$
V_L	liquid superficial velocity, $m\ s^{-1}$
x_k	mass fraction of kth species, m
x, y, z	Cartesian coordinate, m
Greek	
α	relaxation factor
ΔV_p	volume of pth control-volume, m^3
δ_{ij}	Kronecker delta, ($\delta_{ij} = 1$ if $i = j$, and $\delta_{ij} = 0$ if $i \neq j$)
δr_{PE}	distance between cell centers P and E, m
δz_{SP}	distance between cell centers P and S, m
ϵ_k	volume fraction of kth phase, dimensionless
ϵ_g	gas holdup (volume fraction of gas phase), dimensionless
ρ	density, $kg\ m^{-3}$
σ	surface tension of water, $N\ m^{-1}$
κ	parameter defined in equation (6-88b)
λ_s	bulk viscosity of solid-phase, $kg\ m^{-1}\ s^{-1}$
ν	frequency of radiation, s^{-1}
τ	stress tensor, $N\ m^{-2}$
μ	viscosity, $kg\ m^{-1}\ s^{-1}$
Λ	diffusivity of generic scalar ψ , $m^2\ s^{-1}$

ψ a general scalar

Subscripts

$\left. \begin{matrix} e, w, s \\ n, t, b \end{matrix} \right\}$ east, west, south, north, top and bottom faces of a control volume

$\left. \begin{matrix} E, W, S \\ N, T, B \end{matrix} \right\}$ east, west, south, north, top and bottom neighbours of a control volume P

k kth phase or specie

P a general control volume

q continuous phase

s solid-phase

4. Slug Flow Capillary Micro-Channel

4.1 Introduction to Micro-technology

Various methods of process intensification were discussed in chapter 2. In all these methods, due to a reduction in size, the microreactor technology offers substantial PI benefits for a wide range of applications [91]. Microtechnology was originally developed and applied in microelectronics for manufacturing integrated circuits which must have hundreds of transistors in a very small volume. Applying the techniques of microelectronics to mechanical systems such as the actuators, sensors etc emerged a completely new field of application called microelectromechanical systems (MEMS) [17]. In recent times various specialised streams, such as micromechanics, microoptics, microfluids microdevices etc, of microtechnology have been fast emerging.

To facilitate the growing demand for the microtechnology, we are seeing a tremendous improvement in the precision engineering technologies. Etching, lithography, electroplating, moulding, polymer microinjection moulding, and embossing techniques are applied to make the microdevices with different cross-

sectional geometries. Equipment of a variety of material of constructions can now be fabricated using these techniques including metals, glass, polymers and ceramics.

It were the biochemists who introduced the concept of microtechnology to chemical and pharmaceutical industry. Engineers and researchers are beginning to become more and more familiar with terms like the lab on chip, microsystems, microfluidics, micro total analysis systems and micro arrays. Forschungszentrum Karlsruhe and the IMM, Germany, have been the first who fabricated multichannel, microreactors, micromixers, and micro-heat-exchangers in metal by using lithography, electroplating, and moulding [25].

The micro-technology has a lot to offer to chemical engineering applications. In early 70's the concept of "process intensification (PI)" was first introduced to the engineers. Since then several engineering designs of PI equipments have appeared which are cheaper to build, operate and maintain without compromising the plant capacity. In the conventional plant design, any form of direct or indirect costs involved with the process is directly proportional to the size of the plant and inversely proportional to its capacity. But novel technologies such as the microtechnology rather reduce the size of the plant by the factor of magnitude from 100 to 1000 time thus providing substantial cost benefits.

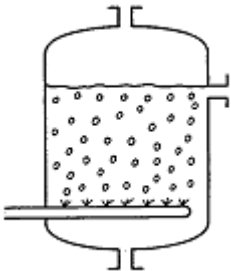
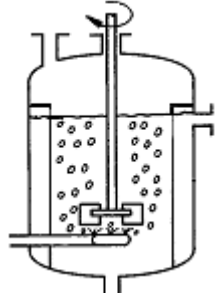
4.2 Gas-Liquid Contactors

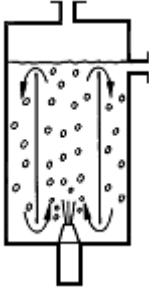
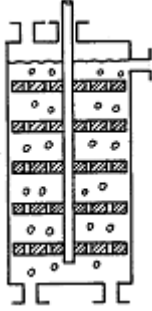
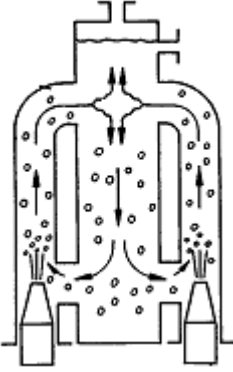
A wide range of gas liquid contactors are used in chemical process technology. These contactors can be classified into two main groups primarily on the principle of operations, namely surface contactors and volume contactors. Also in the literature one may find terms such as the low and high performance contactors. This classification is based on the mass transfer rate that can be achieved. Generally, in high performance contactors the dissipation of mechanical energy results in very high magnitudes of mass transfer coefficients whereas in low performance contactors, the mechanical energy is only used to overcome the hydrostatic pressure difference.

In the surface gas-liquid contactors, as the name suggests the gas-liquid transfer phenomena occurs on the surface of the liquid. Generally an impeller or a jet is submerged near the surface of liquid. The liquid is usually held in low depth pools or basin. In another form of surface contactors, a rotating horizontal liquid drum is submerged in the liquid pool and placed in the bulk of the gas phase. A constant

liquid film is formed over the rotating drum where the mass transfer takes place. Mostly surface contactors are used for biological waste water treatment and related applications.

In a volume gas–liquid contactor, the gaseous phase is dispersed in the form of small or large bubbles with regular spherical or irregular shape. The interfacial area between the two phases is created within the bulk of liquid. The gas dispersion in the liquid may be achieved with the help of spargers, liquid jets through two-mixture nozzles or hollow rotating mixers. Some of volume gas–liquid contactors are shown schematically in Figure 10.

Type of Contactor	Characteristics
 <p data-bbox="406 1153 614 1187">Bubble Column</p>	<ul style="list-style-type: none"> • Cheaper and easier to construct operate and maintain. • Comparatively low mass transfer performance. • Large range of bubble sizes means difficulty in predicting interfacial area. <p data-bbox="805 1131 997 1164">Deckwer [92]</p>
 <p data-bbox="414 1601 598 1635">Stirred Vessel</p>	<ul style="list-style-type: none"> • Smaller bubble sizes can be produced. • High surface area per unit volume as well as through increasing the level of turbulence in the liquid. • Difficult to scale up. • Mechanical Complexity and high maintenance cost. <p data-bbox="805 1680 949 1713">Judat [93]</p>

 <p style="text-align: center;">Jet Loop Reactor</p>	<ul style="list-style-type: none"> • The shear field induced by the liquid jet at the nozzle outlet causes gas dispersion and generates bubbles of very small size. • They have good mixing properties. • They do not have dead volumes. • Better mass transfer characteristics. • Good performance in limited range of flow rates. <p style="text-align: right;">Blenke [94]</p>
 <p style="text-align: center;">Reciprocating Jet Reactor</p>	<ul style="list-style-type: none"> • Small bubble size distribution can be achieved • Unlike stirred bubble column size distribution can be easily controlled. • Mechanical complexities add to setup and operating cost. <p style="text-align: right;">Brauer [95]</p>
 <p style="text-align: center;">Impinging Stream Reactor</p>	<ul style="list-style-type: none"> • Very high turbulence and very large interfacial areas are achieved in impinging zones. • Gas liquid mass transfer is comparatively greater than bubble column. • Limited flow ratios can be used. • Not useful when two phases have small density difference. • Higher operating costs and difficulties in scale-up. <p style="text-align: right;">Gaddis [96]</p>
<p>Figure 10 Various gas-liquid contactors [97]</p>	

A common drawback of conventional equipment is their inability to condition the bubble size precisely and the non-uniformities that arise due to the complexities of the underlying hydrodynamics. There has been extensive work done to understand the underlying transport phenomenon affecting the hydrodynamics of the conventional systems. But due to the complex nature of these systems, generally there are issues such as [98]:

- Interfacial areas are defined poorly.
- Scaled up design are generally do not provide optimum output.
- Uncertainties and lack of confidence in the design.

Thus a novel technology must be developed to overcome these limitations.

4.3 Microchannel

Capillary microchannels offer superior mass transport and selectivity over the conventional gas-liquid (-solid) contactors. Due to their small dimensions, the microchannels have high surface to volume ratio, and consequently exhibit high heat and mass transfer coefficients. Secondly, they offer simplicity in the scale up by replication or bundling of microreactor units. This minimizes the costly redesigning, thus shortening the development time from the lab scale to commercial production. For these reasons the microchannels are finding increasing applications in process intensification.

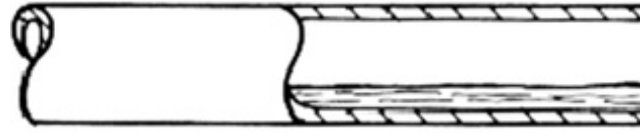
Numerous researchers over the past decade have used microchannels for various applications. Some of these applications include, the solid catalysed gas-liquid reactions [1-4], hydrogenation [5, 6, 8], and Fischer-Tropsch synthesis [7]. The performance of these microchannels largely depends on the underlying hydrodynamics of the gas-liquid (-solid) flow. Depending on the operating conditions and design parameters, the gas-liquid flow in a microchannel exhibits various flow regimes as shown in Figure 11 viz. bubbly, churn, slug and annular flow [9-12, 14, 15, 91, 99].



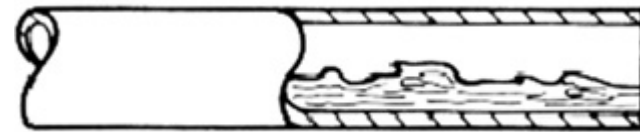
Bubbly Flow



Plug Flow



Stratified



Wavy



Slug



Annular

Figure 11 Flow regimes observed in horizontal two phase flow [100]

Over a wide range of operating conditions of interest to gas-liquid reactions, the slug flow regime characterised by alternate bullet shaped bubbles separated by free gas-entrained liquid slugs is observed. This type of slug flow regime is called the Taylor flow regime [10]. In the Taylor flow, there is a very thin liquid film between the gas bubble and channel wall. The gas-liquid mass transfer; pressure drop and residence time distribution are largely function of the liquid film thickness and slug length [91].

The mass transfer characteristics in the Taylor flow regime have been widely studied [4, 9, 99], which roughly depends on the slug properties like bubble rise velocity, liquid film thickness, gas liquid slug lengths and liquid diffusivity. van Baten and

Krishna [101] proposed a CFD model to predict this mass transfer coefficient as function of the slug properties. Their CFD model for mass transfer co-efficient assumes the flow to be ideal and uniformly distributed along the length of the channel. The model requires geometric properties (length, shape etc.) of the slug as an input. Depending on the operating and design parameters, the geometric properties of the slug will change. A hydrodynamic model capable of predicting slug properties for various operating and design parameters will be highly useful. This model can then provide the input needed to detailed computational models like that proposed by van Baten and Krishna [101] to compute the mass transfer coefficients. Some efforts in this direction are reported in the literature [91, 102, 103].

Besides the design and operating parameters, the hydrodynamics of fluids in slug flow capillary microchannels is also dictated by physical properties of the fluids such as the viscosity, surface tension and wall adhesion. In this work, we focus on studying the effect of various process parameters and physical properties on gas and liquid slugs. The gas-liquid flow in Taylor slug flow regime for a microchannel has been modelled using the volume of fluids method. Different inlet geometry configurations (angle of entry) and channel diameters (4mm, 2mm, 1mm and 0.5mm) are simulated. The effect of gravity, superficial velocities of both the phases and contact angle has also been studied.

4.4 Flow characterisation

It is customary to express the quantitative analysis of a problem in terms of dimensionless groups which reduces the number of independent variables and enhances the generality of results. The hydrodynamics and mass transfer in the slug flow capillary microchannels can be characterised using the dimensionless numbers and parameters mentioned in the Table 7. The definitions of those numbers for the slug flow are based on flow of two alternate phases. However, in some cases, the surface properties are dominant which result in the formation of a film on the capillary surface. The continuous phase, generally a liquid, forms a film around the gas bubble is termed as the carrier or continuous phase while the gas phase is called as the slug.

One of the important dimensionless number for the characterisation of all types of flows is the Reynolds number, Re , which relates the inertial force to the viscous force. In microchannel, due to low flow velocities and micrometer sizes, the

Reynolds number is very low meaning the viscous force is dominant over the inertial force. Besides, the capillary force is also significant which is related to the viscous force by the capillary number, the ratio of the viscous force to the capillary force.

These groups of dimensionless numbers can be used to represent the so called flow maps in Figure 12. These flow maps allow well defined operating conditions for slug flow regime in microchannels. Typically, the flow maps are constructed of liquid superficial velocity versus gas superficial velocity. In these maps, experimentally determined flow patterns are plotted with distinct markers, and the boundaries, i.e., the transitions of one flow pattern to the other are plotted by lines. Which flow pattern actually occurs in a given capillary channel depends on the gas and liquid properties ($\rho_G, \mu_G, \rho_L, \mu_L, \sigma$), duct geometry (at least d) and gas and liquid velocities (U_l, U_g). The number of relevant dimensionless groups is large, and most experimental flow maps in the literature are applicable only to the specific systems under which they were obtained. But some experimental studies have presented flow maps independent of fluid properties. Suo and Griffith [104] performed such experiments using octane, heptane and water as liquids and helium, nitrogen and argon as gases. No significant changes were found for the different gases and the groups (ρ_G/ρ_L) and (μ_G/μ_L) were eliminated from consideration.

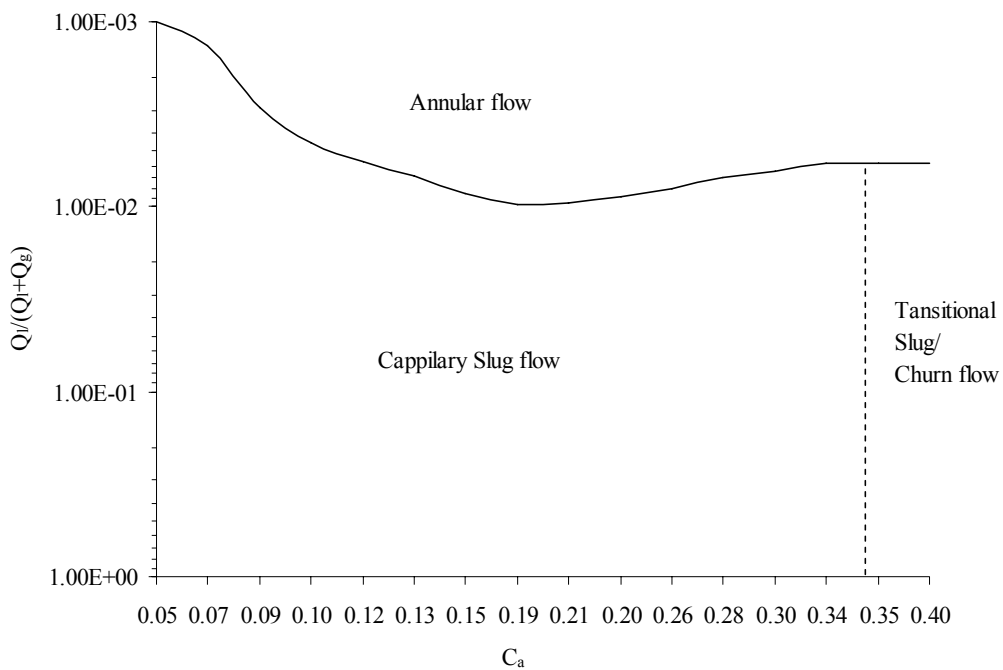


Figure 12 Flow map of Suo and Griffith for $Ca/Re=1.5 \times 10^{-5}$ [104]

In addition to this, the viscosity and density ratio are also important for characterising the system because of the large difference in the densities of the liquids and gas makes the flow patterns more complex due to the influence of the buoyancy forces. Furthermore, the mixing within the slugs is characterised by the Peclet number. Although in this study, the mass transfer rates were not calculated, it is important to take a note of dimensionless numbers that characterize the mass transfer in multiphase microchannel. These include the interfacial diffusion which is characterised by the Fourier number. The Peclet number relates the convective and diffusive mass transport and the Fourier number gives an idea about the progress of the diffusive transport process. Finally, the diffusivity ratio and partition coefficient give an idea about the possible progress of the mass transfer.

Table 7 Dimensionless quantities used to characterize flow in microchannel

Name	Definition	Mathematical representation
Reynolds Number	Ratio of inertial force vs viscous force	$\frac{\rho U d}{\mu}$
Capillary Number	Ration of viscous force vs capillary force	$\frac{\mu U}{\lambda}$
Viscosity ratio	Ratio viscous force of each phase	$\frac{\mu_1}{\mu_2}$
Bonds or Eötvös Number	Ratio of gravitational force to surface tension force	$\frac{\rho g r^2}{\sigma}$
Peclet number	Ratio of convective mass transfer to molecular diffusivity	$\frac{d_s^2 U_s^2}{DL}$
Diffusivity ratio	Ration of diffusivity of species A in liquid phase to gas phase	$\frac{D_l}{D_g}$

4.5 Computational model

4.5.1 Model Geometry

An inverted capillary microchannel as shown in Figure 13 was used for modelling. It comprised of a mixing tube and two inlet tubes each for water and air respectively. All three tubes were separated at angles θ_1 , θ_2 and θ_3 on a single plane.

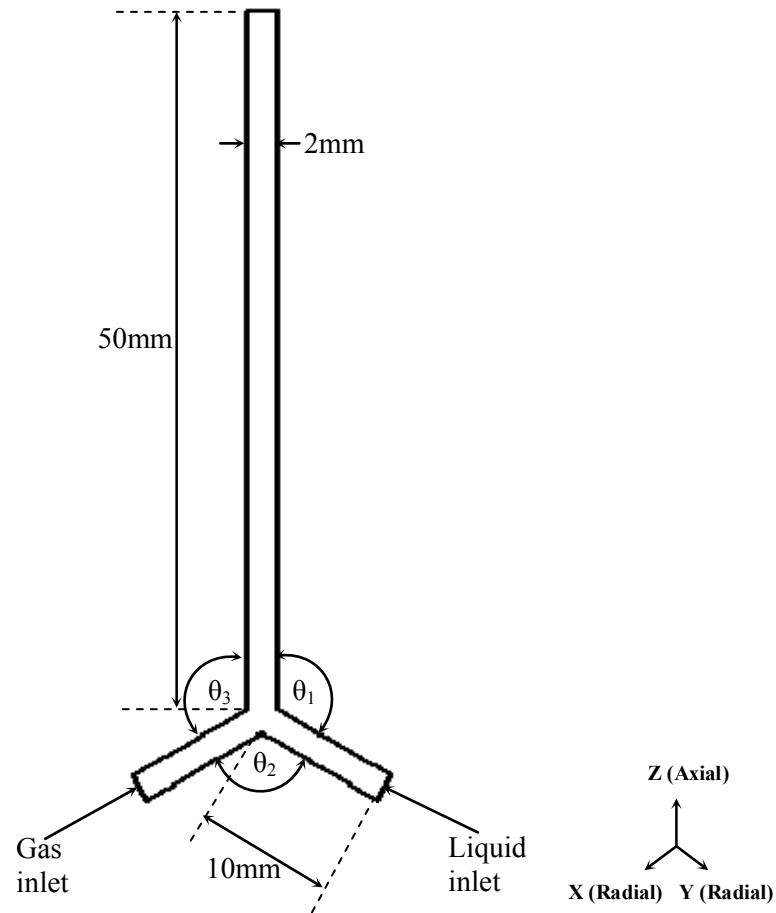


Figure 13 Schematic of microchannel used in modelling.

Table 8 Geometry configurations for studying the effect of entry angle

Configuration number	θ_1	θ_2	θ_3
1	180°	60°	120°
2	120°	120°	120°
3	180°	90°	90°
4	90°	180°	90°

These angles were then varied across the same plane as listed in Table 8 to study the effect of angle of entry. Finally, an equiangular (120° , inverted Y-junction) channel was selected for further investigations.

4.5.2 Model Parameters

The flow in slug flow capillary microchannel is characterised by segregated gas and liquid phases separated by a sharp interface. Various methods are available for the dynamic characterization of free surfaces such as front tracking, level set, marker particle, shock capturing and volume of fluid (VOF) [90]. They are detailed in Chapter 3 Section 3.7.4. The VOF formulation was used due to its particular advantages in the interface tracking over the other approaches. It is also relatively simple and accurate to apply to boundary fitted grids and accommodates the breakup and formation of interfaces. In the VOF approach, a single set of momentum equations is shared by the fluids. The volume fraction of each fluid, in each computational cell, is tracked throughout the domain [83]. The flow inside the channel was assumed to be incompressible since the pressure drop along the channel is very small. Furthermore, the flow is essentially laminar, dominated by surface tension forces over the gravitational forces. A finite volume based CFD package FLUENT (Release 6.3) was used for simulations in this study.

4.5.3 Simulation Parameters

A capillary microchannel exhibits the Taylor flow regime at superficial gas (U_g) and liquid (U_l) velocities ranging from 0.01 to 0.25 ms^{-1} [105]. A working range from 0.01 to 0.1 ms^{-1} was used for the CFD simulations. Air and water were used as the gas and liquid phases respectively. The geometry was meshed using GAMBIT software, a CFD pre-processor and then imposed into FLUENT for simulations. Transient simulations were carried out for a given set of gas and liquid velocities. At the outlet a pressure outlet boundary condition was imposed with gauge pressure equal to zero (in equilibrium with atmosphere). The PRESTO (pressure staggering option) scheme was used for the pressure interpolation. The pressure-velocity coupling was done using the SIMPLE scheme was used. A second order upwind discretization was applied for momentum equation. For interpolating the gas-liquid interface, the geometric reconstruction scheme was used. These parameters are detailed in Table 9 given below. Adequate time step (usually 1×10^{-5} s) was used to limit the global courant number to 0.25. The results were considered to attain steady

state and converged when the global mass fluxes were balanced and all the residuals were maintained below 1×10^{-3} . After the steady state was achieved, the time averaged data were collected for a quantitative analysis.

Table 9 Simulation parameters (SFR)

Parameter	Value
Flow parameters	Laminar Incompressible Isothermal
Boundary Conditions	Gas Inlet - Velocity Inlet Liquid Inlet - Velocity Inlet Outlet – Pressure Outlet Liquid Wall contact angle specified at Wall
Pressure Interpolation	PRESTO (Pressure Staggering Option)
Pressure Velocity Coupling	SIMPLE
Momentum Equation	Second Order Upwind
Interface Interpolation	Geometric Reconstruct

4.6 Results and Discussion

4.6.1 Comparison of 2D and 3D model

CFD simulations of multiphase flows can be computationally intensive for large computational meshes. A simplification is often sought to reduce the computational time without compromising the results. One commonly used simplification is representing the three dimensional real system as a two dimensional model. In previous studies, mathematically, premixed fluids were used to compare 2D and 3D geometries of capillary microchannels [91, 99]. By premixing the two fluids one ignores the inertial forces produced in the mixing zone, which determines the slug behaviour in the microchannel. Therefore, in this study, simulations were carried out for non-premixed fluids using a 2D and 3D geometry.

In the capillary microchannels, the surface tension force dominates over the gravitational and inertial forces. The pressure difference across the interface between two fluids due to the surface tension is given by Equation 1, the Young Laplace equation [106].

$$\Delta p = \frac{2\sigma}{r_{Curv}} \quad 31$$

The Laplace pressure is a strong function of the shape of the interface. For several randomly selected points, the Laplace pressure was calculated from the average pressure drop across the front and back interfaces of different bubbles, for both 2D and 3D simulations. Table 10 lists the calculated Laplace pressure from simulations, using Equation 31 and the experimentally observed values of Qian and Lawal [105]. The Laplace pressure compares well for both 2D and 3D simulations. Due to the radius of curvature in 3D, the Laplace pressure in case of 3D is twice that in 2D. The minor discrepancy in predicted and theoretical Laplace pressure is due to finite grid resolution.

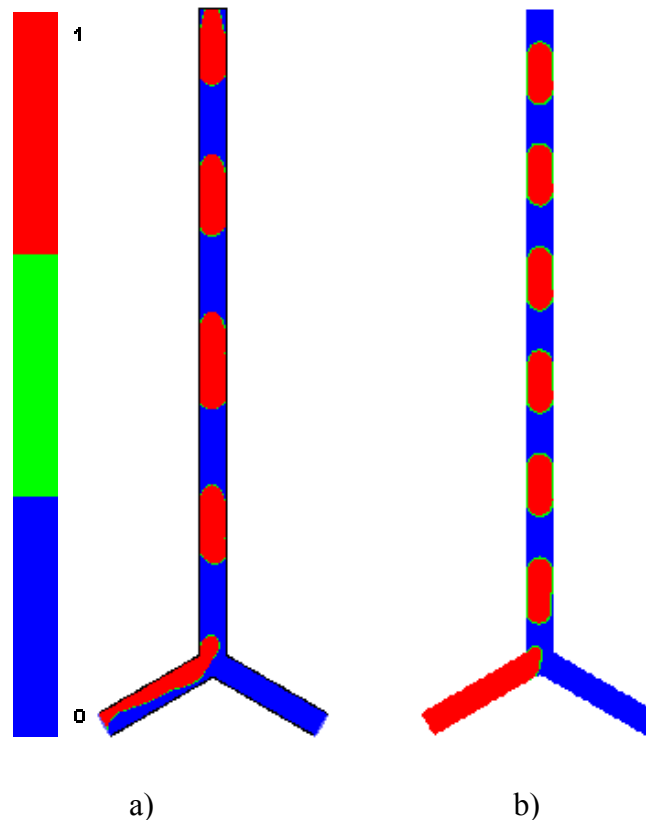


Figure 14 a) Slug flow development in 2D $L_g = 6.36$ mm b) Slug flow development in 3D; $L_g = 4.96$ mm (red- gas slug and blue- liquid slug)

The snapshots of gas phase volume fraction at liquid and gas superficial velocities equal to 0.1 ms⁻¹ is shown in Figure 14 for both 2D (Figure 2a) and 3D (Figure 2b) geometries. These snapshots were used to calculate the mean gas and liquid slug lengths using an open source image processing software ImageJ [107]. The calculated slug lengths were compared with the data of Qian and Lawal [105] and Vandu et al [108]. The values reported here are the experimental data used by them in their analysis. The slug lengths are reported in Table 10. As can be seen, the predicted slug lengths for 2D simulation were greater than those for 3D simulations. However, the calculated mean gas and liquid slug lengths for 3D model were in reasonable agreement with the previous studies. Hence for all subsequent simulations 3D model geometry was used.

Table 10 Comparison between 2D and 3D results

Type of Geometry	2D	3D
Pressure Drop (pa)		
Simulation	82.3	145.6
Young-Laplace theory	72.8	175
Qian and Lawal [22]	75	180
Liquid slug length (mm)		
Simulation	6.36	4.96
Qian and Lawal [22]	4.7	4.7

4.6.2 Effect of mesh size

The results of any CFD calculation depend on the computational mesh quality and size. Therefore, it is important to resolve the mesh to an extent that the solution is mesh independent i.e. the solution does not change significantly on further mesh refinement. However, the mesh refinement has a computational cost. Not only the computational time increases due to the increased number of mesh points, it also has an effect on the stability of the solution. The stability and convergence of numerical solution of a transient partial differential equation is depends on the Courant-Friedrichs-Lewy Condition (CFL) commonly known as the Courant number determines the condition of convergence [109]. The Courant number defined by

Equation 32 is a dimensionless number that compares the time step in a calculation to the characteristic time of transit of a fluid element across a control volume.

$$Co = \frac{\Delta t}{\Delta x_{cell} / v_{fluid}} \quad 32$$

The Courant number is inversely proportional to the characteristic mesh dimension. Hence, to keep the Courant number low (usually < 0.25) one needs to use appropriately low time step. This increases the demand on computational resources. Therefore, a balance needs to be achieved between the desired accuracy of the solution and the size of the computational mesh.

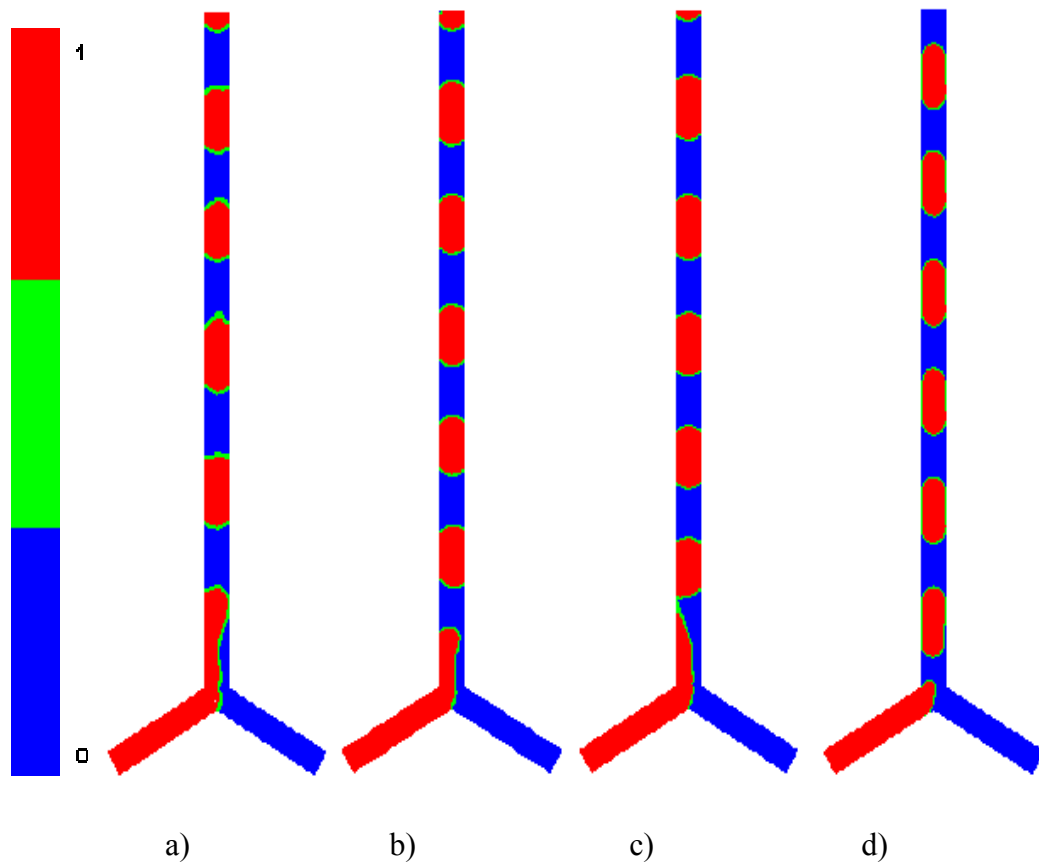


Figure 15 Slugs at different mesh resolution ($U_g = 0.1 \text{ ms}^{-1}$, $U_l = 0.1 \text{ ms}^{-1}$, $t = 0.5 \text{ s}$); a) Grid size 0.4mm b) Grid size 0.3mm c) Grid size 0.25mm & d) Grid size 0.2mm.

Four different mesh sizes (from 0.4 mm to 0.2 mm) were used to evaluate the effect of mesh size. The resulting gas volume fraction contours are shown in Figure 15. For the coarser grid the interfaces were twisted and finer grids reported sharper and accurate interfaces. The Laplace pressure calculated using the shape of the interface for all the mesh sizes is shown in Figure 14. As the mesh size was reduced, the

discrepancy between the analytical and computed Laplace pressure reduced. Any further reduction in the mesh size would result in only marginal improvement in the solution and that too at significantly increased computational time. Hence 0.2 mm mesh was used for further studies. At this mesh resolution, the film around gas slug was not captured. In the slug flow regime, for all capillaries, the film thickness is in the range of 1-20 μm . With our current computational resources, mesh resolution to this detail implied practically impossible computational times.

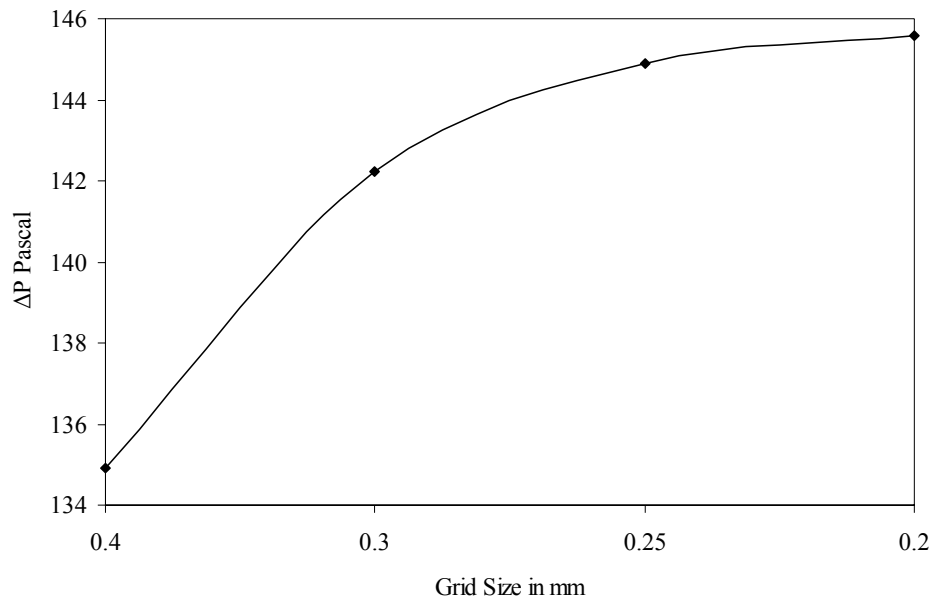
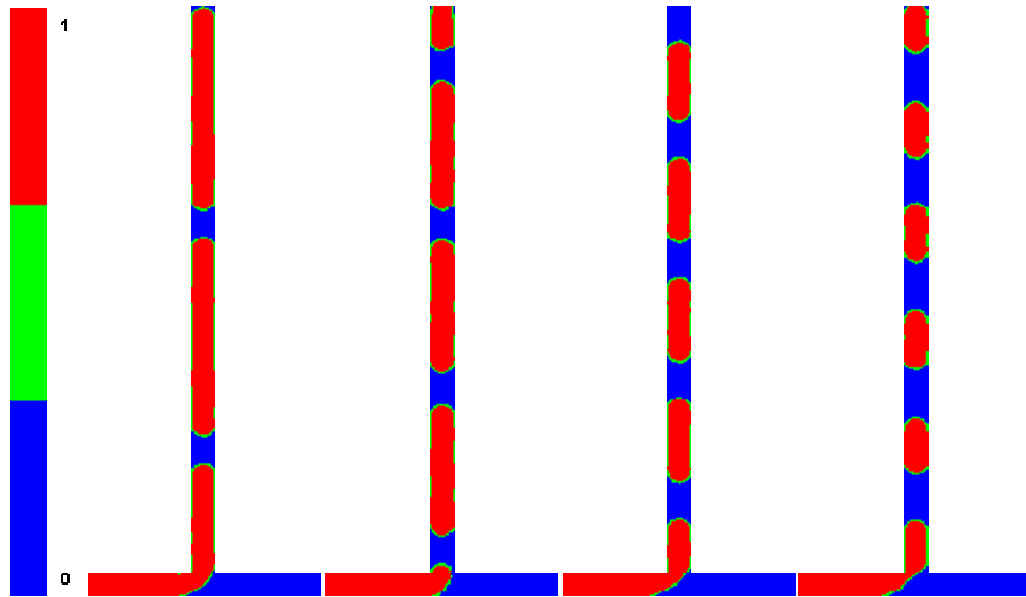


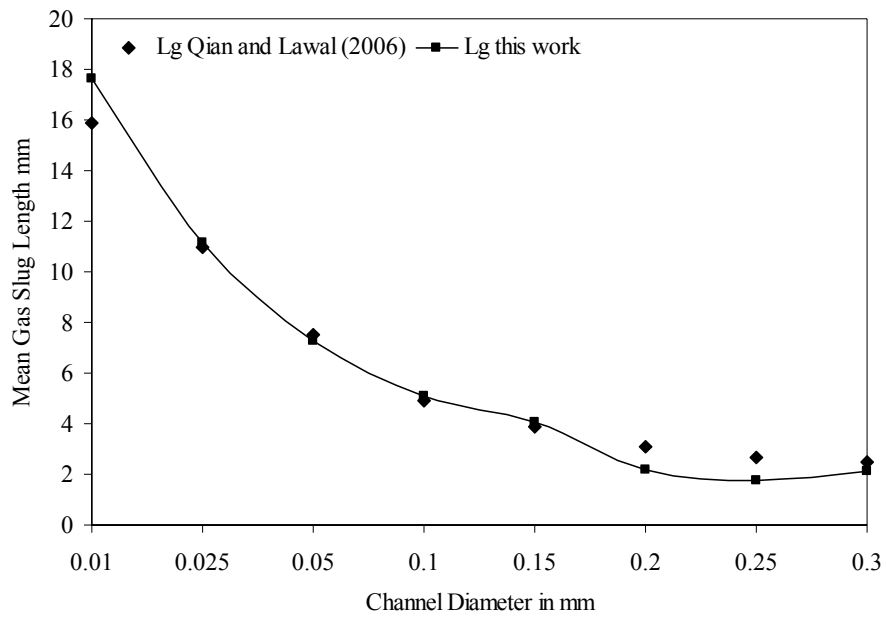
Figure 16 Effect of grid size on analytical Laplace pressure drop across the interface.

4.6.3 Comparison with previous work

The liquid superficial velocity directly influences the slug length [99]. Qian and Lawal [105] have reported data for mean gas slug lengths as a function of liquid superficial velocity for a T junction microchannel. This data was used to validate the model. The superficial gas velocity was kept constant and superficial liquid velocity was varied from 0.01 ms^{-1} to 0.3 ms^{-1} . The contours of gas volume fraction Figure 17a) and corresponding mean gas slug lengths (Figure 17b) for various liquid superficial velocities are shown in Figure 17. As can be seen from Figure 17a, with the increase in U_l the mean slug length L_g decreases. A Similar trend was also observed when U_l was kept constant and U_g was varied. This property was studied to validate our model. It can be seen from Figure 17bb that our results are in reasonable agreement with previous work published by Qian and Lawal [105].



a)



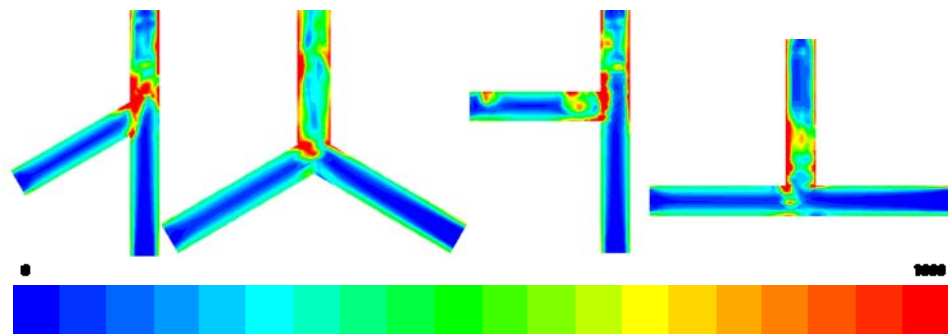
b)

Figure 17 a) Contours of volume fraction of air $U_l = 0.1, 0.05, 0.025$ & 0.01 ms^{-1} (left to right); b) Effect of liquid velocity on mean gas slug length. $U_g = 0.1 \text{ ms}^{-1}$, $t = 0.5\text{s}$.

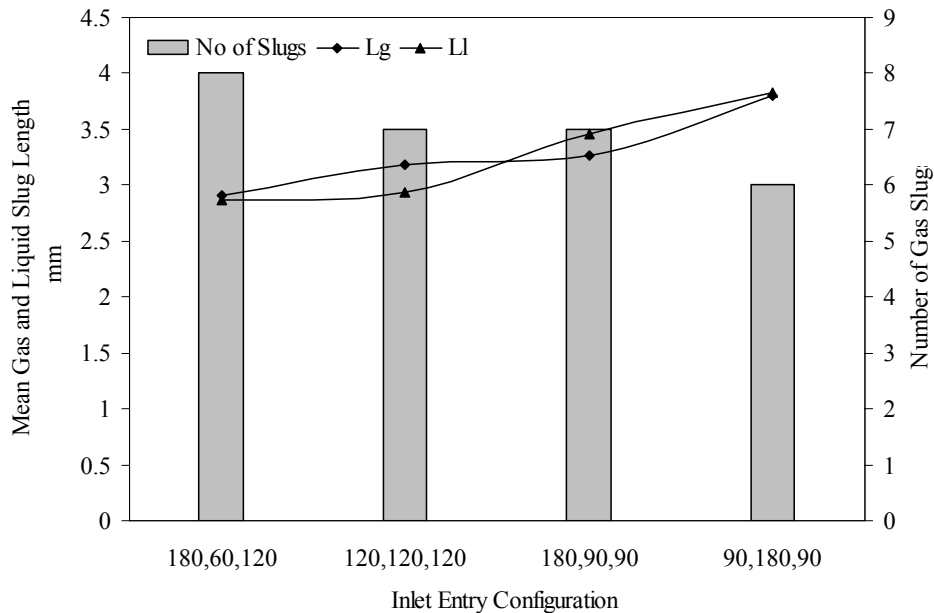
4.6.5 Effect of angle of entry

To understand the effect of inertial forces, generated during the slug formation, on the resulting slug properties, angle of entry ($\theta_{1,2,3}$) shown in Figure 13 was varied on the same plane. Table 8 lists different configurations used in this study. The contours

of vorticity magnitude in the mixing zone (Figure 18a) and resulting mean gas and liquid slug lengths and number of gas slugs (Figure 18b) are shown in Figure 18 for varying angles of entry. It can be seen from Figure 18b that for fixed length of mixing channel varying $\theta_{1,2,3}$ has significant effect on the number of slugs formed and the mean slug size. Introducing gas feed at an angle smaller than 90° reduces the slug length. Thus it might be beneficial to introduce the gas at an angle smaller than 90° as opposed to introduce gas and liquid feed head to head or perpendicular as suggested in some of the previous published work [91, 105]. The reason for smaller slug lengths is the presence of bigger toroidal vortices in the mixing zone as seen in Figure 18a.



a)



b)

Figure 18 a) Contours of vorticity magnitude in mixing zone for various inlet geometries b) Mean gas, liquid slug length and number of gas slugs for varying angle of entry $U_g = 0.1 \text{ ms}^{-1}$, $U_l = 0.1 \text{ ms}^{-1}$, $t = 0.5\text{s}$.

Toroidal vortices occur when fluid flows back on itself. Generally they produce large centrifugal forces and high Reynolds numbers. These vortices are dominant in the mixing zone where the dimensions are small and decay rapidly once the slug is detached. It is commonly accepted that larger toroidal vortices in the mixing zone will produce smaller slugs [105]. Consequently, these vortices help the slugs to detach easily resulting in more slugs per unit length of channel. For the current study, we have selected configuration 2 (Table 8) for further investigation on the effect of various operating parameters.

4.6.6 Effect of channel diameter

The effective channel diameter is an important constraint in designing microchannels. Smaller the channel diameter, smaller will be the mixing zone which will increase the toroidal vortices. It is desirable to generate bigger toroidal vortices to increase the number of slugs and decrease the slug size for a given channel length. In this study, we have characterized four channel diameters (4mm, 2mm, 1mm and 0.5mm). Figure 19 shows that for smaller channel diameter larger number of small slugs can be generated. For the subsequent investigations, the 2mm channel was selected.

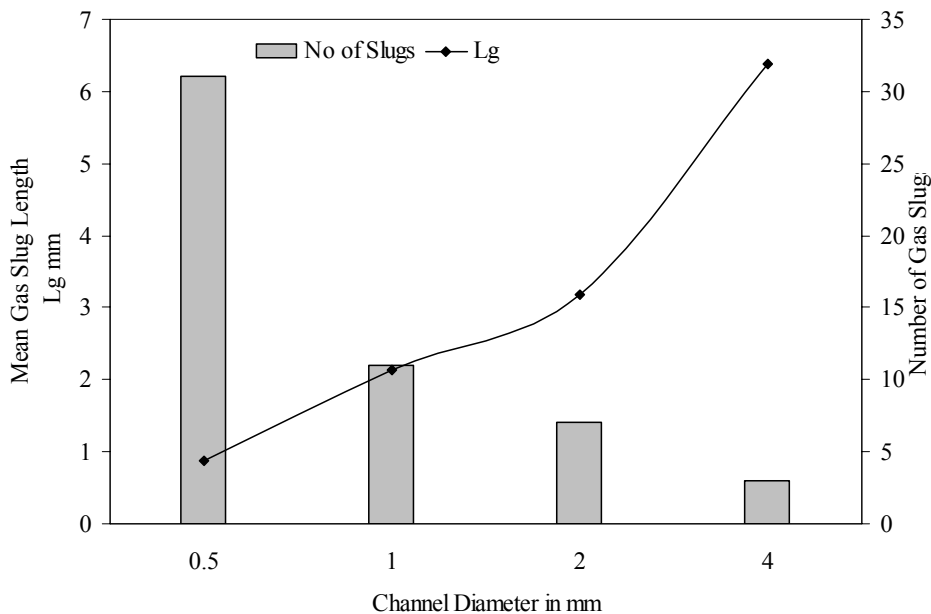


Figure 19 Mean gas slug length and number of gas slugs for varying channel diameter; $U_g = 0.1 \text{ ms}^{-1}$, $U_l = 0.1 \text{ ms}^{-1}$, $t = 0.5 \text{ s}$.

4.6.7 Effect of gravity

Hydrodynamic behaviour of fluids in microchannels is different from that in the conventional pipe flows. At submillimeter range, the importance of surface tension force over gravitational forces can be explained by the dimensionless Bond number (Equation 33).

$$Bo = \frac{\rho g r^2}{\sigma} \quad 33$$

Systems with higher Bond number are largely dominated by the body forces (gravitational) and the surface tension force has a lesser effect. The effect of radius on the Bond number is plotted in Figure 20. As the Bond number reduces, consequently the effect of gravity is minimal. Hence, placing the channel vertically or horizontally will not change the slug shape or size for a fixed capillary diameter. But at higher Bond numbers (i.e. larger capillary diameter), when the channel is placed horizontally it is difficult for slug to detach. To study the effect of gravity, the ratio of the axial length required for slug detachment between horizontal and vertical channels was compared for various channel diameters. It can be seen from Figure 21 that for the bigger channel diameters, axial length required for the slug detachment in horizontal channel is 1.5 times greater as compared to that required in vertical channel. It is evident that for channel diameter 0.5mm, the effect of gravity is negligible and for channel diameter 4 mm the gravity has significant effect.

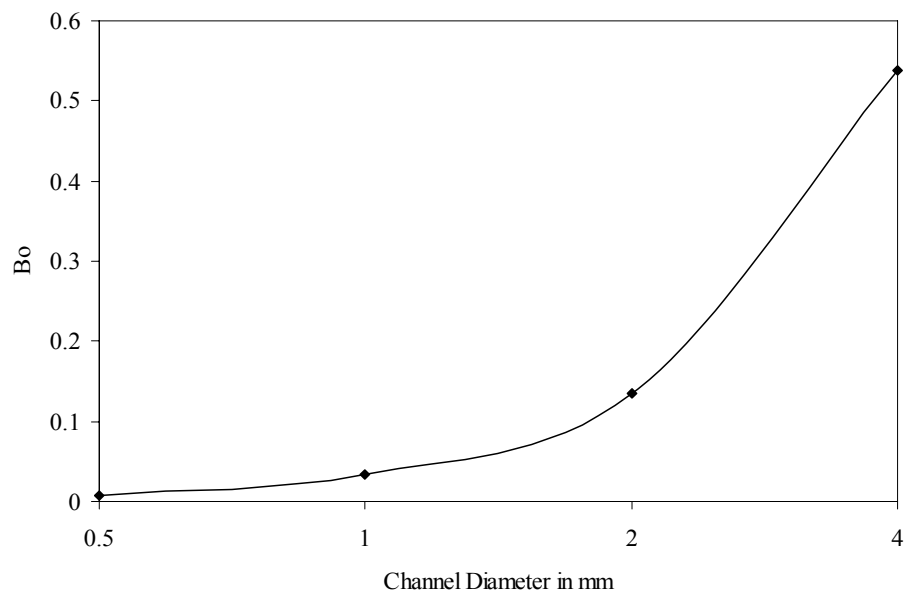


Figure 20 Bond number versus effective channel diameter.

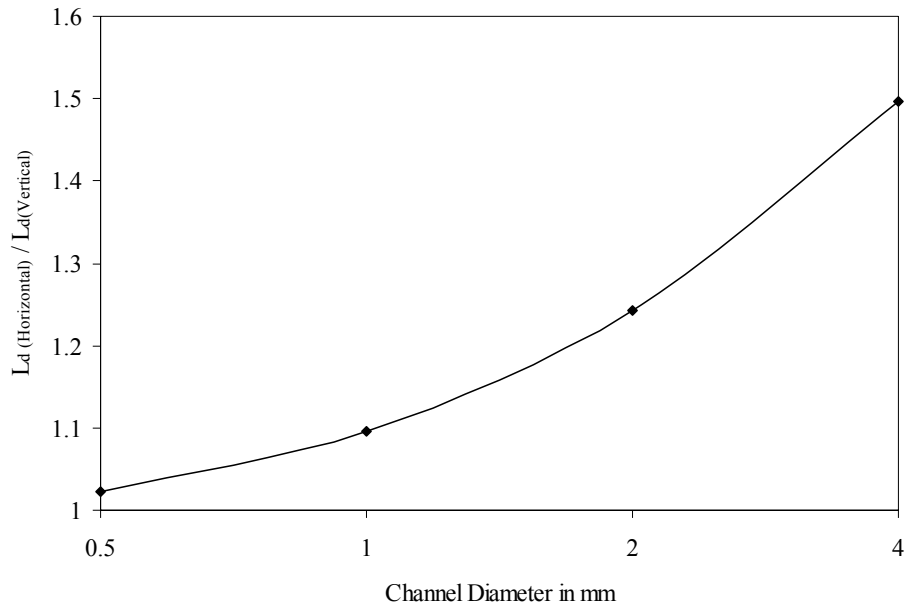


Figure 21 Ratio of slug detachment length required between horizontal and vertical channel for varying channel diameters $U_g = 0.1 \text{ ms}^{-1}$, $U_l = 0.1 \text{ ms}^{-1}$.

4.6.8 Effect of Contact angle

To enhance the reliability of our CFD simulations it is important to understand the effect of the wetting properties of fluids on the slug behaviour. The wetting properties of liquid were studied by varying the liquid contact angle on the wall from 0° to 120° . It can be seen from Figure 21 that the mean gas and liquid slug lengths decrease with the increase in wall contact angle. It was also observed that the shape of the slug changes from concave to convex for the gas slugs and vice versa for the liquid slugs with the increase in liquid wettability.

4.6.9 Pressure drop

It is extremely important to have accurate knowledge of the pressure drop while scaling up a microchannel to maintain identical flow characteristics and stable operating conditions. This is generally known as the hydrodynamic stability [110]. Thus to maintain this hydrodynamic stability in a full scale microchannel a detailed knowledge of the pressure drop in single capillary microchannel is essential. Also the performance of full-scale microchannel is underlined by characteristics power required due to the total pressure drop created along the length of the channel. Hence in this section using empirical correlations and raw data from CFD simulations, pressure drop characteristics are elaborated.

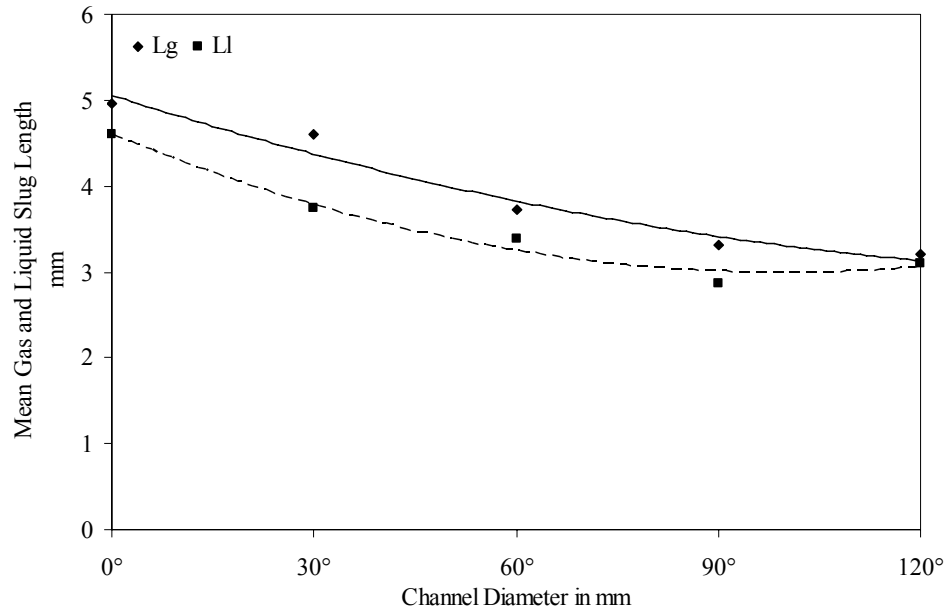


Figure 22 Effect of contact angle on mean gas and liquid slug length.

Predicting pressure drop along the microchannel can be a challenging task. Although there are various numerical algorithms available in literature and the concept is well detailed but these numerical algorithm require important hydrodynamic properties such as the slug length, liquid and gas holdups etc. as inputs. Thus for predicting the correct pressure drop we require a numerical model that can provide inputs for the analytical approach to predict pressure drop along the microchannel. From the above detailed CFD model, important hydrodynamic properties were collected and used in the below described correlations.

The total pressure drop in gas–liquid flow consists of the pressure drop caused by the friction, acceleration, gravity and the shape of the bubbles:

$$\Delta P_{tot} = \Delta P_{fric} + \Delta P_{acc} + \Delta P_{grav} + \Delta P_B \quad 34$$

Where ΔP_{tot} is the total pressure drop,

ΔP_{fric} is the pressure drop due to friction,

ΔP_{acc} is the pressure drop due to acceleration,

ΔP_{grav} is the gravitational pressure drop and

ΔP_B is the pressure drop due to the shape of the bubble.

Frictional pressure drop is calculated using the following equation:

$$\Delta P_{fric} = L_c f \rho_l \varepsilon_l U^2 \frac{2}{d} \quad 35$$

Where L_c is the channel length, ρ_l is the density of liquid phase, ε_l is the liquid phase hold up, d is the channel diameter, for multiphase flow U can be given as;

$$U = U_g + U_l \quad 36$$

An important term in equation 37 is f which is the friction factor. For the Taylor flow, various correlations are available in the literature and are presented in the Table 11 below;

Table 11. Various correlations to calculate friction factor

Reference	Equation	
Standard, one phase laminar flow	$f = \frac{16}{R_e}$	37
Bretherton, analytical solution [111]	$f = \frac{16}{R_e} \left[1 + 0.465 \frac{d}{L_s} \left(\frac{1}{C_a} \right)^{0.33} \right]$	38
Kreutzer et al, [110]	$f = \frac{16}{R_e} \left[1 + 0.17 \frac{d}{L_s} \left(\frac{1}{C_a} \right)^{0.33} \right]$	39

Horvath et al. [112] used the Bretherton law and measured the pressure drop at different slug lengths, *ceteris paribus*, and found that the pressure drop increased when the slugs were shorter than 15 times the channel diameter. The authors also discussed the slug length dependence in relation to mass transfer from short slugs. Although a plot of ΔP versus $(Lslug/d)$ was consistent with equation 38, because the author did not include the Laplace term, for constant L and U , Δp was only roughly equal to $a + b/L_l$.

Fujioka and Grotberg [113] investigated the steady propagation of a liquid slug within a two dimensional channel lined by a uniform, thin liquid film. They used the Navier-Stokes equations with free-surface boundary conditions and calculated numerically the pressure drop across the slug and found that for short slugs, the Laplace terms dominate, and hence that the pressure drop is a slug-length dependent parameter [113].

Equation 38 was modified by Kreutzer et al after performing a series of experiments in a 2.3mm diameter vertical channel. They discovered that the friction factor was

function of the fluid properties and slug length only and apparently independent of velocities. Also that the inertia can be taken into account with the dimensionless group $Re/Ca = \mu^2/\rho d \gamma$, which is independent of velocities and all data, could be accurately represented by equation 39. Thus for this study to calculate the frictional pressure drop equation 39 was used.

Ca is the capillary number and is defined as the ratio of the viscous forces versus surface tension acting across the interface between the liquid and gas. Numerically the capillary number can be written as;

$$C_a = \frac{\mu U_b}{\sigma} \quad 40$$

Where, μ is the viscosity of the liquid, U_b is the bubble rise velocity and σ is the surface tension.

Pressure drop due to the acceleration is calculated using equation 33, where m is the mass flux, L_c is the channel length, x is the mass transport fraction ρ is the density of the corresponding phase and ε is the hold up.

$$\Delta P_{acc} = m^2 \left\{ \left(\frac{x_g^2}{\rho_g \varepsilon_g} + \frac{x_l^2}{\rho_l \varepsilon_l} \right)_{L=L_c} - \left(\frac{x_g^2}{\rho_g \varepsilon_g} + \frac{x_l^2}{\rho_l \varepsilon_l} \right)_{L=0} \right\} \quad 41$$

Various investigators have numerical and experimental proven and concluded that it could be safely assumed that the pressure drop due to acceleration can be neglected [114-116]. Otherwise the increase in the gas holdup and therefore in the volumetric flow rate due to the pressure drop will lead to an increase in the velocities.

Depending on the geometrical configuration and operating conditions gravitational pressure drop may either play a significant role in determining the overall pressure drop or can be neglected. One of the important criteria that determine the effect of gravity in microchannel is the dimensionless bond number as described in the above section. Also if the channel is placed horizontally the effect of gravity on the total pressure drop can be neglected. According to Bretherton [111] and Hazel and Heil [117] the effect of gravity in either horizontal or vertical channel can be neglected for low bond numbers. This phenomenon was also observed when the mean slug lengths were compared for horizontal and vertical channels of varying effective Bond numbers. Although some of the operating conditions selected have significant effect

of gravity, in pressure drop calculations gravitational pressure drop was given consideration.

In microchannel gravitational pressure drop can be calculated from,

$$\left(\frac{\Delta p}{\Delta L}\right)_{grav} = (\varepsilon_g \rho_g + \varepsilon_l \rho_l) g \sin \omega \quad 42$$

Where, g is the force due to gravity and ω is the angle of inclination. Thus one can see in horizontal column pressure drop due to gravity will have no effect.

The pressure drop over a moving bubble due to the different shape of the bubble front and bubble tail, caused by surface tension effects, was found by Bretherton [111] to be,

$$\Delta P_B = 3.58 \frac{\sigma}{r} \sqrt[3]{9C_a^2} \quad 43$$

Where, r is the bubble radius which in this case can be safely assumed to be the channel radius. It has been experimentally observed by many researchers that this pressure drop caused due to the shape of the bubble can be assumed to have negligible effect on the channel pressure drop.

Pressure drop was calculated and reported for varying operating conditions. A single set of conditions (detailed in

Table 12.) was selected for a comparison between the analytically calculated pressure drop and the raw data of pressure values obtained directly from the simulation. In experimental investigation performed by Fries et al, they calculated the pressure drop between the liquid inlet and liquid outlet. Whereas in the current geometric parameters liquid outlet is not defined separately thus, to maintain logical similarity between the experimental work and computational results time and area weighted average pressures were obtained at the outlet only for liquid phase. The pressure drops were then calculated and presented as raw data below. Also all hydrodynamic data required for analytical calculations of equations 34-43 (including bubble rise velocities, liquid slug length and liquid and gas holdups) were time averaged once the steady state was achieved.

Values of the individual components of the pressure drop are presented in Table 13.

Table 12 Operating conditions and physical properties for calculating pressure drop

Parameter	Value
Length, L_c	50mm
Diameter, d	2mm
Channel type	Inverted-Y/Vertical
U_g	0.1 m/s
U_l	0.1 m/s
ρ_g	1.225 kg/m ³
ρ_l	1000 kg/m ³
σ	0.0729 N/m
μ_l	1×10 ⁻³ Pa.s
g	± 9.81 m/s ²

ζ - ± indicate the direction of the force acting

From the above case study it can be clearly seen that the gravitational pressure drop plays a significant role. This is because of two reasons, one that the channel is operated vertically and hence a larger contributor to pressure forces is the gravitational effect. And secondly the Bond number lies in the upper range for small channel. This highlights the benefit that CFD simulations can offer in providing valuable information for characterising the flow conditions in microchannel, thus avoiding the need for the costly experimentation.

Table 13 Comparison of analytical and CFD calculated pressure drop

Variable	Value
U_b	0.216 m/s
L_s	3.74 mm
ε_g	0.53
ε_l	0.47

ΔP_{fric}	43.9 Pa
ΔP_{grav}	± 232.66 Pa
ΔP_{B}	11.47 Pa
ΔP_{Total}	± 177 Pa
P Inlet (CFD)	± 13.46 Pa
P Outlet (CFD)	± 193.99 Pa
$\Delta P_{\text{(CFD)}}$	± 180.53 Pa
Error%	$\pm 1.9-2.0$ %

4.6.10 Internal recirculation

Various researchers have notably predicted numerically and experimentally that when the gas bubbles and liquid slugs move through the capillary, depending on the prevailing physical properties and operating conditions, there exist internal circulations within the slugs. A typical gas-liquid slug flow in a capillary microchannel is shown in Figure 23. The shear between the wall surface and slug axis produces internal circulations within the slug which reduce the thickness of boundary layer at the phase interface thereby enhancing the diffusive penetration. These circulations are illustrated schematically in Figure 24 which shows two zones: a recirculation zone at the centre of the slug and a stagnant zone where the liquid velocity is effectively zero. Similar type of circulation inside liquid slugs of bubble train flow has also been reported by other researchers (Kashid et al, 2007 (a-c), 2008), (Kreutzer et al, 2005 (a), (b)), (Thulasidas et al, 1997) and (Gruber, 2001) [91, 110, 118-120]



Figure 23 Typical alternate gas-liquid slug flow in microchannel

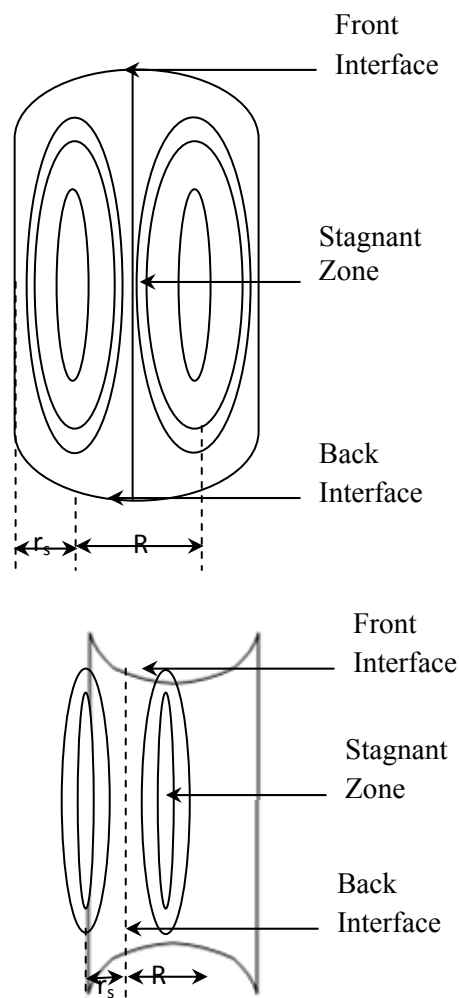


Figure 24 Schematic of the internal recirculation in gas bubble and liquid slug

4.6.10.1 Phenomenological model

Model geometry comprised of two dimensional gas bubble and liquid slug as shown in Figure 25. Each unit was considered separately as a two-dimensional, single phase domain and solved individually as a decoupled system. The length of the slug was obtained from the 3D simulations carried out earlier and are reported in the section above. The diameter of the slug was obtained by subtracting the film thickness from the channel diameter. Film thickness was estimated from the correlation of Aussilous and Qu ere for round capillaries [121]

$$\frac{\delta}{D} = \frac{0.66Ca^{2/3}}{1 + 3.33Ca^{2/3}} \quad 44$$

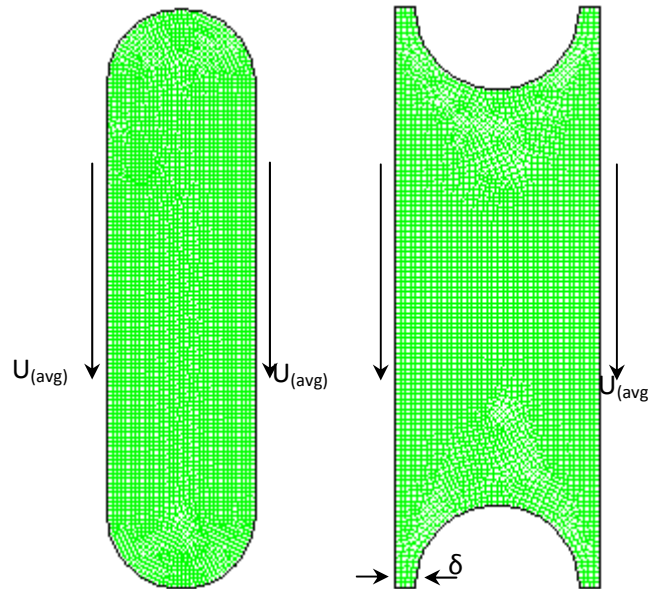


Figure 25 Grid display of gas bubble and liquid slug

For computational simulations following assumptions were made for both the gas bubble and liquid slug simulations:

- Front and back interface of each slug had same geometry.
- 2D non-stationary model was assumed.
- The slug size was the same for all flow velocities.
- The fluid in each slug was considered to be Newtonian, incompressible and isothermal.

List of simulation parameters are presented in Table 14.

Table 14 Simulation parameters for single phase simulation

Parameter	Value
Flow parameters	Laminar Incompressible Isothermal
Boundary Conditions	Moving Wall at $U_{(avg)}$ Fluid – Air (Bubble) Water (Liquid Slug)
Pressure Interpolation	PRESTO (Pressure Staggering Option)
Pressure Velocity Coupling	SIMPLE
Momentum Equation	Second Order Upwind

It can be seen from the velocity contours presented in Figure 26 and Figure 27 that maximum velocity is at the centre and minimum velocity at the wall. This indicates a fully developed parabolic (Poiseuille) profile. The contours of the internal circulations (velocity vector magnitude) within the gas bubble and liquid slug are shown in Figure 27 clearly showing circulation patterns and stagnant zones (zero vector magnitude). Two flow patterns were observed within each slug: a recirculation zone at the centre and in the proximity of wall and two stagnant zones in between them. When the slug moves through the capillary, due to the shear between slug axis and capillary wall, the liquid in the centre moves to the front end of the slug, where it touches the front interface and returns back along the wall of the capillary. While at the back end, the liquid moves from the wall to the centre of slug and thus circulation take place. Therefore, the parabolic profile is bidirectional in nature showing a maximum velocity at the centre of the slug, zero velocity at some radial position r_s (stagnant zone) and negative velocity at the wall surface. The velocity profiles shown in Figure 28 were taken at the centre of the slug which shows a fully developed parabolic velocity profile.

Also particle tracks were generated for both gas bubbles and liquid slug and recirculation patterns are shown in Figure 29. These recirculation patterns are strongly influenced by the slug geometry. With an increase in the curvature of the

extreme ends of the slug the circulation area within the slug decreases. In addition the slug length plays an important role in determining the recirculation pattern. This parametric study will remain the area of interest for future research.

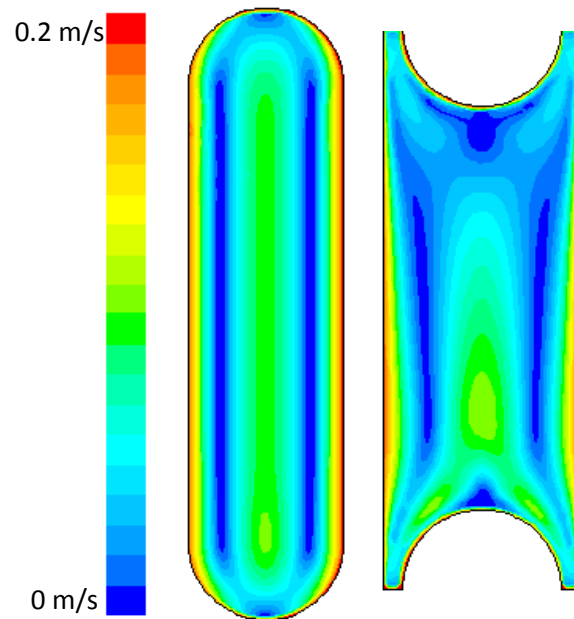


Figure 26 Contours of velocity gas bubble(Left) and Liquid Slug(Right) ($L_g = 4.7\text{mm}$, $L_s = 3.7\text{mm}$, $U_{(avg)} = 0.2\text{ m/s}$)

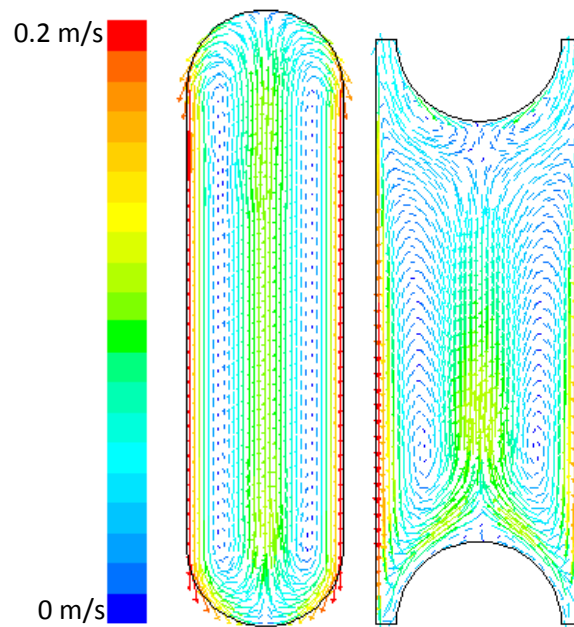


Figure 27 Velocity vectors within gas bubble and liquid slug, internal recirculation, gas bubble(Left) and Liquid Slug(Right) ($L_g = 4.7\text{mm}$, $L_s = 3.7\text{mm}$, $U_{(avg)} = 0.2\text{ m/s}$)

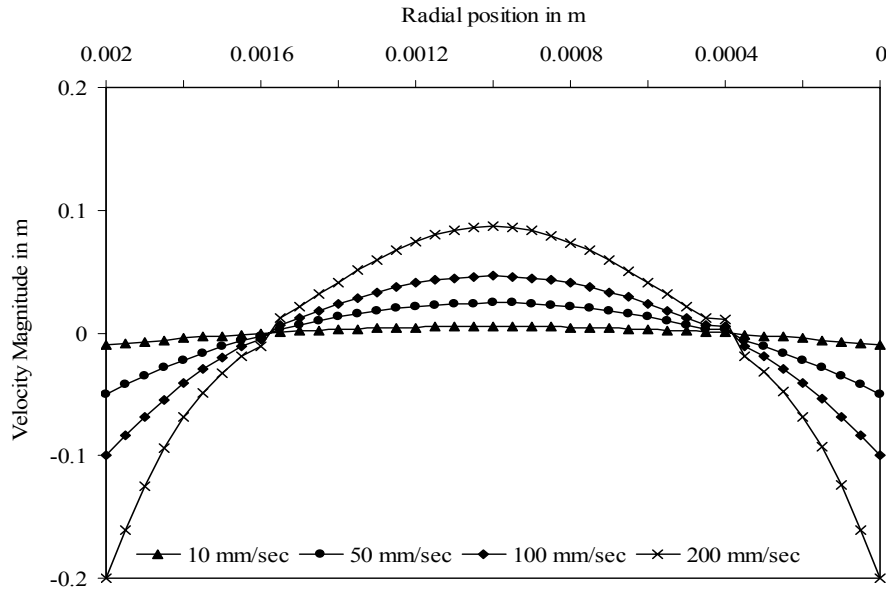


Figure 28 Parabolic velocity profile within the liquid slug ($L_s = 3.7\text{mm}$, $D = 1.8\text{mm}$ and $\delta = 0.1\text{mm}$)

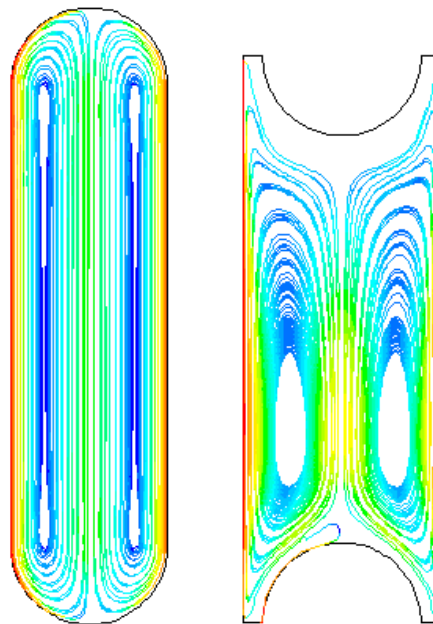


Figure 29 Internal circulations by particle tracing in gas bubble and liquid slug ($L_g = 4.7\text{mm}$, $L_s = 3.7\text{mm}$, $U_{(avg)} = 0.2\text{ m/s}$)

4.6.11 Chemical reaction

When a slug flow capillary microchannel is utilised to perform operations involving mass transfer or chemical reactions they are generally known as microreactors. In this section the channel performance will be evaluated for a selected set of

multiphase reaction. Also the terminology microreactor will be used in the section to address the above described microchannel. In the gas-liquid slug flow capillary microreactor, the phases are present as a series of alternating gas bubbles and moving slugs, constituting a series of well-defined individual sub-volumes which give an excellent accessibility for modelling. A number of theoretical models have been developed to describe mass transfer with and without chemical reactions between two immiscible liquid phases. However, the theoretical models do not give detailed information about the hydrodynamics involved as it governs the performance of the system. The recent developments in the CFD simulations have attracted chemical engineers for its use in the design of chemical equipment involving mass transfer and chemical reactions. Some mathematical models have already been developed for benchmarking reactor performances for various applications and are listed in Table

15

Table 15 Literature review on numerical models for mass transfer with and without chemical reaction in the gas-liquid microreactor.

System	Description	Researcher
Carbon dioxide absorption in a falling film microstructured reactor.	Experiments and Modelling: Two-dimensional model was formulated and solved for CO ₂ absorption in NaOH solution in a falling-film microstructured reactor	M. Zanfir and A. Gavriilidis [122]
Reactor model for fast reactions in the micro-bubble column.	The catalytic oxidation of butyraldehyde to butanoic acid and the CO ₂ absorption into NaOH were simulated. Direct fluorination of toluene was also studied and compared with previously published experimental data	V. Haverkamp et al [123]
Mass transfer with chemical reaction in segmented (slug) flow	CFD Simulations using fixed interface techniques for system involving Kerosene (+acetic acid) – water (+NaOH)	Harries et al [124]
CFD simulations of mass transfer from Taylor bubbles rising in capillaries	Fundamental CFD model to predict mass transfer in gas liquid flow	Van Baten and Krishna [101]
Liquid-liquid mass transfer and chemical reaction	CFD model for 2D single phase was develop to evaluate mass transfer performance in liquid-liquid extraction with and without chemical reaction	Kashid et al [120]

The role of gas bubbles and liquid slug lengths on mass transport in the Taylor flow through capillaries.	Gas-liquid mass transfer coefficients were measured by physical absorption of methane in water, The measured data were fitted into the proposed expression, which was developed by assuming plug flow of the liquid slug	Bercic et al. [125]
DC process for manufacturing Hydrogen peroxide	Series of three papers have presented the detailed analysis of experimental and theoretical model to evaluate the reaction chemistry of this process.	Voloshin et al [126-128] Inuone et al [129] Chen et al [130]

In summary, there are various models developed by researchers over the past decade to resolve mass transfer characteristics in slug flow capillary micro channel and these can be divided into two categories: (i) a mathematical/phenomenological approach and (ii) CFD simulations. Generally mathematical models require important hydrodynamic characteristics as input to resolve the mass transport. Commonly due to barriers such as flow complexities and demand for high computational resources required for CFD simulations, the effect of mass transfer and reaction is ignored. However, due to strong bidirectional coupling these parameters can sometime strongly influence the flow patterns within the slugs. In this work species mass transport model is incorporated in conjunction with a 3D VOF multiphase model to assess the effect of chemical reaction within the gas bubble and liquid slug.

Dehydrogenation of hydrogen peroxide reaction was selected a model reaction. It is an elementary reaction in three step process of well known direct synthesis for manufacture of hydrogen peroxide. Hydrogen peroxide is a widely used industrial chemical and its largest consumer is pulp and paper industry. Due to environmental concerns in using chlorine-based bleaches, environmentally friendly hydrogen peroxide serves as a good replacement [131]. Conventionally hydrogen peroxide is produced in Reidl-Pflederer process commonly known as AO (anthraquinone autoxidation). But, AO process is energy intensive since high concentration hydrogen peroxide are produced through steam distillation in high volumes at large centralized plants. Moreover, higher cost of transportation expenses are required to deliver the products from the plant to the end-user, and additional expenses are incurred by the end-user for the dilution of the concentrated H_2O_2 . Whereas, these challenges do not exist in DC process and hence it is an attractive alternate for production of H_2O_2 .

Generally DC process involves contacting of gas phase (H_2 and O_2) and liquid solvent over solid catalyst to produce liquid products. Although this process seems promising and simple, it has not been applied commercially mainly due to two major drawbacks [127]:

1. The DC of hydrogen and oxygen involves several reaction pathways that result in either the synthesis of H_2O_2 and water, or consumption of H_2O_2 . The challenge is to find the right catalyst that maximizes the rate of H_2O_2 synthesis while minimizing the side reactions.

2. Hydrogen/oxygen mixtures are flammable in the range of 5–76 vol% of H₂ in air.

The later is a major concern in commercialization of this process. To avoid any explosion, very high operating pressures must be used usually in the range of few thousand PSI [126-129, 132-138], this significantly increases the operating costs and makes the DC process less viable. However, hydrogen and oxygen can be reacted in an inherently safe manner in a microreactor similar to the one explained in the above sections. The width of microchannels is smaller than the quenching distance of hydrogen and oxygen radicals hence an explosive chain reaction is practically impossible [126-128, 139-141].

o Reaction mechanism and kinetics

In DC process for manufacturing of hydrogen peroxide a series of reaction occur as shown in Table 16. From the process point of view it is desirable to maximize the selectivity of production of H₂O₂ by step 1 over its decomposition by steps 3 and 4.

Table 16 Reactions in series for DC process

Step	Reaction	Rate
1	$H_2 + O_2 \rightarrow H_2O_2$	$R_{H_2O_2}^1$
2	$H_2 + \frac{1}{2}O_2 \rightarrow H_2O_2$	$R_{H_2O_2}^2$
3	$H_2O_2 + H_2 \rightarrow 2H_2O$	$-R_{H_2O_2}^3$
4	$H_2O_2 \rightarrow H_2O + \frac{1}{2}O_2$	$-R_{H_2O_2}^4$

$$\text{Overall Rate of production of H}_2\text{O}_2 = R_{H_2O_2}^1 + R_{H_2O_2}^2 - R_{H_2O_2}^3 - R_{H_2O_2}^4$$

In the present work, reduction of H₂O₂ in step 3 was selected for modelling. Kinetics data for CFD modelling was obtained from experimental work of Voloshin et al [127]. According to them, the reaction follows first order kinetics with rate expression described as [127]

$$R_{H_2O_2}^3 = \frac{C_{H_2O_2,in} - C_{H_2O_2,out}}{W} \frac{34gH_2O_2}{mol} \quad 45$$

Where,

$R_{H_2O_2}^3$ is the overall rate of reduction of hydrogen peroxide,

$C_{H_2O_2,in}$ is the concentration of hydrogen peroxide entering in mol L⁻¹

$C_{H_2O_2,out}$ is the concentration of hydrogen peroxide leaving in mol L⁻¹

W is the weight of catalyst in grams.

o Methodology

Reaction kinetics was modelled using the species transport formulation in FLUENT.

For the kinetics of the reaction following assumptions were considered reasonable:

- Reaction is not mass transfer limited, internal or external mass transfer has no effect on the reaction kinetics [127].
- Reactions are assumed to be volumetric.
- Both fluids are assumed to be Newtonian, viscous and incompressible.
- Shape and size of the slugs do not change in the reaction zone.
- The flow is assumed to be laminar.

Interfacial mass transfer of each of the species were calculated analytically based on the kinetic model derived from experimental work by Voloshin et al [127] and is presented in Appendix A. The conservation equations for all chemical species namely, H₂O₂, H₂, Water and N₂ were solved in each of the individual phases. Using the reaction kinetics data of Voloshin et al [127] volumetric mass generation and consumption rates of each species were calculated. The reactor used for studying the chemical reaction in micro channel consisted of horizontal 2mm diameter T-junction microchannel with the configuration number 3 in Table 8. A schematic of the reactor used in shown in Figure 30.

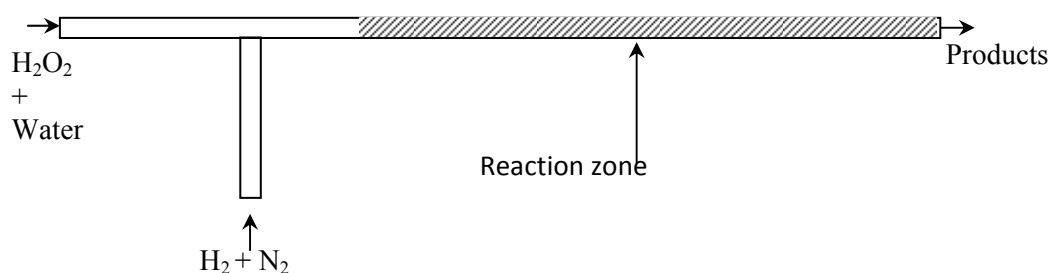


Figure 30 A Schematic diagram of the microchannel for reaction.

Total length of the mixing zone was 50 mm, which consisted of reaction zone of length 40mm. Both inlets were 2mm diameter and 10mm long. Structured mesh of size 0.2mm was generated using CFD pre-processor Gambit version 2.4.

o Governing equations

In addition to the VOF formulations explained in Chapter 2 the conservation equation for each species was solved to predict the local mass fraction of each species. The generalized form of this equation for i th species can be written as

$$\frac{\partial}{\partial t} \rho Y_i + \nabla \cdot (\rho \vec{v} Y_i) = \nabla \cdot \vec{j}_i + R_i + S_i \quad 46$$

Where,

\vec{j}_i is the diffusion flux of species i , which arises due to the concentration gradients, calculated by,

$$\vec{j}_i = -\rho D_{i,m} \nabla Y_i \quad 47$$

R_i is the net rate of production of species i by chemical reaction, zero for this case.

S_i is the is the rate of creation by addition from the dispersed phase plus user-defined source/sink.

An equation of this form was be solved for N-1 species where N is the total number of fluid phase chemical species present in the system. Since the mass fraction of the species must sum to unity, the N^{th} mass fraction is determined as one minus the sum of the N-1 solved mass fractions.

o Simulation parameters

The geometry was meshed using GAMBIT software, a CFD pre-processor and then imported into FLUENT for simulations. Transient simulations were carried out for a given set of operating conditions detailed in Table 17 . At the outlet a pressure outlet boundary condition was imposed with gauge pressure equal to zero (in equilibrium with atmosphere). PRESTO (pressure staggering option) scheme was used for pressure interpolation. The pressure-velocity coupling was done using the SIMPLE scheme. A second order upwind discretization was applied for momentum, energy and species conservation equation. For interpolating the gas-liquid interface, a geometric reconstruction scheme was used.

Table 17 Operating conditions for simulating chemical reaction

Parameter	Value
Gas velocity	0.57 m/s
Liquid velocity	0.18 m/s
Mass fraction of H ₂	0.291
Mass fraction of H ₂ O ₂	0.1156 (0.34mol/l)
H ₂ O ₂ conversion	14 %

Table 18 Simulation parameters for species transport model

Parameter	Value
Flow parameters	Laminar Incompressible Isothermal
Fluid	Gas Phase – H ₂ + N ₂ Liquid Phase - H ₂ O ₂ + H ₂ O
Boundary Conditions	Gas Inlet - Velocity Inlet Liquid Inlet - Velocity Inlet Outlet – Pressure Outlet
Pressure Interpolation	PRESTO (Pressure Staggering Option)
Pressure Velocity Coupling	SIMPLE
Momentum Equation	Second Order Upwind
Interface Interpolation	Geometric Reconstruct
Energy equation	Second Order Upwind
Species Conservation equation	Second Order Upwind

These parameters are detailed in Table 18 given above. Adequately small time step (usually 1×10^{-5} s) was used to limit global courant number to 0.25. The results were

considered to attain steady state and converged when global mass fluxes were balanced and all the residuals were maintained below 1×10^{-3} . After steady state was achieved, time averaged data were collected.

o CFD Analysis

Chemical reaction was modelled along with the hydrodynamics in a 3D model. It can be seen from Figure 22 and 23 that a fully developed Taylor flow regime existed for the operating conditions used. Figure 22 indicates that the amount of hydrogen peroxide progressively decreased along the capillary length and was converted to water. Simultaneously the amount of hydrogen also decreased.

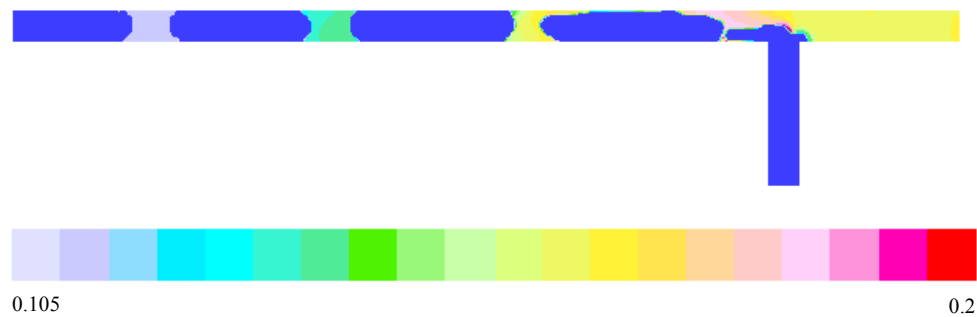


Figure 31 *Contours of mass fraction of hydrogen peroxide*



Figure 32 *Contours of mass fraction of hydrogen*

To perform a quantitative analysis, mass balances and stoichiometric calculations were performed on the overall system using the extrinsic kinetic data of Voloshin. The details of the stoichiometric and mass balance calculations are presented in Appendix A. Overall species mass fractions calculated from the CFD simulations are compared with the values obtained from the reaction kinetics data in Table 19. The raw data obtained from CFD simulations were in good agreement with the experimental kinetics data of Voloshin [127]. Figure 33 and Figure 34 shows mass concentration profiles of the reactants getting consumed along the length of the

reactor. Thus it can be safely concluded that knowing the correct extrinsic reaction rates, CFD model can provide and insight into intrinsic analysis of the reaction kinetics. Furthermore, interfacial mass transfer can also be incorporated along with the chemical reaction for mass transfer limited reactions.

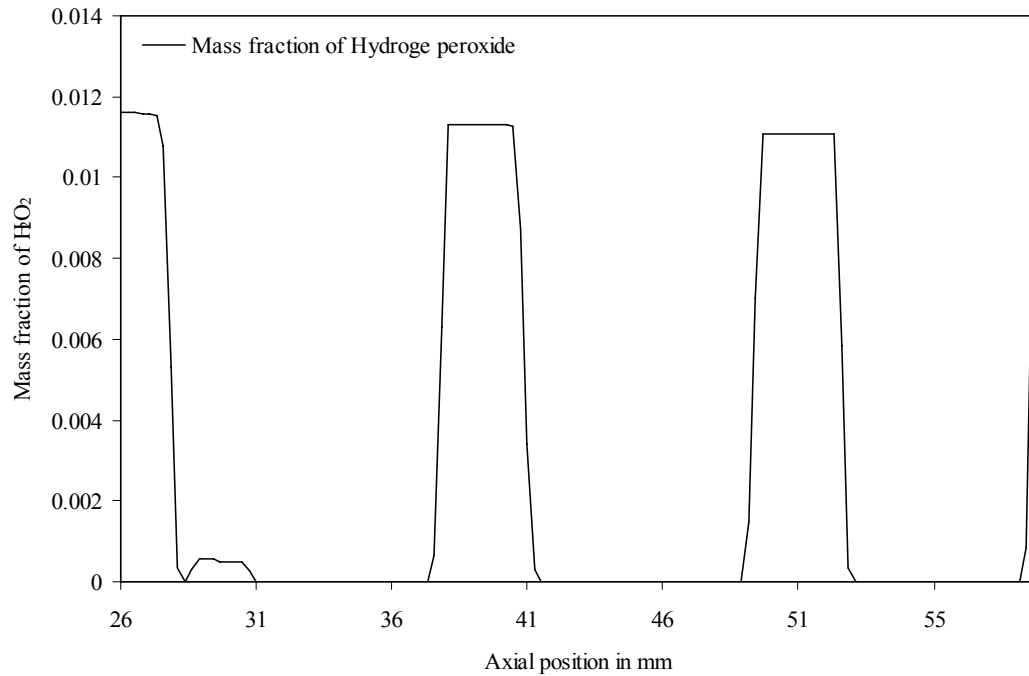


Figure 33 Mass fraction of hydrogen peroxide along the reaction zone

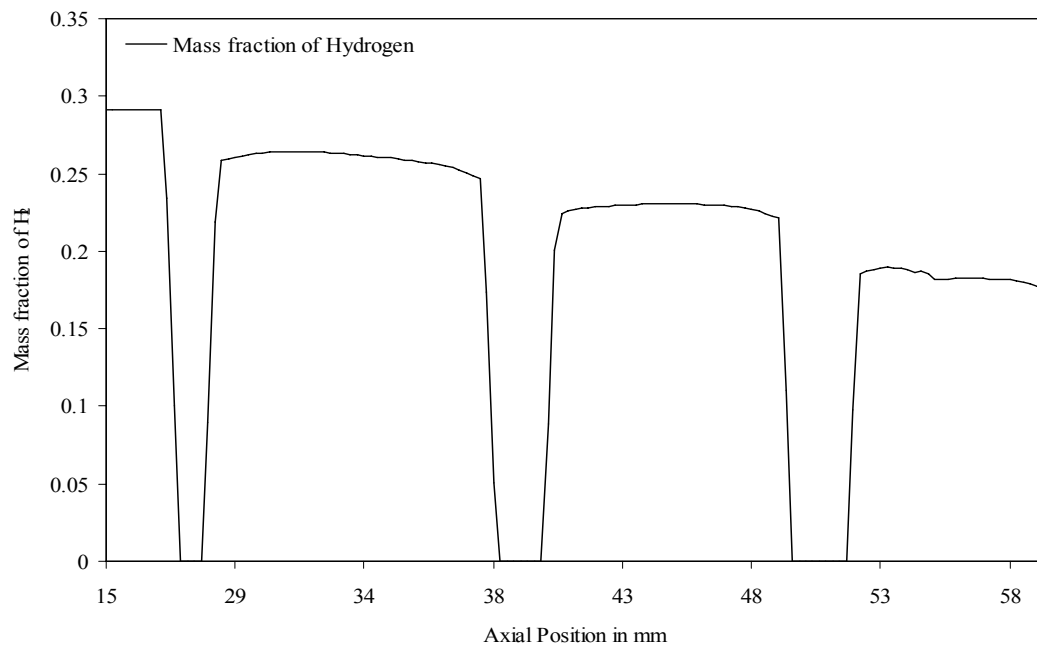


Figure 34 Mass fraction of hydrogen along the reaction zone

Table 19 Comparison of species mass fraction

Component	Mass Fraction (Extrinsic reaction data)	Mass Fraction Calculated from CFD simulation
H ₂ O ₂ (In)	0.01156	0.01156
H ₂ O ₂ (Out)	0.0109	0.010423
H ₂ (In)	0.291	0.29097
H ₂ (Out)	0.17	0.17098
H ₂ O (In)	0.98844	0.98844
H ₂ O (Out)	0.9891	0.9891

4.7 Summary

Simulations were carried out to investigate the flow regimes, slug size, internal recirculation and pressure drop under various operating conditions with different mixing elements and various downstream capillaries. The geometrical configurations of the mixing elements and microchannel dimensions showed a significant effect on the slug size and its hydrodynamic behaviour. The pressure drop was also measured along the length of the slug flow capillary microchannels. A theoretical prediction for pressure drop along slug flow capillary was developed based on the correlations for capillary pressure and hydrodynamics pressure drop and compared with simulation results. In comparison with conventional contactors superior hydrodynamic performances were noted which includes key features such as well defined flow patterns, minimal pressure losses, and improved interfacial and specific areas.

CFD simulations were also conducted to understand the mechanism of slug flow generation and characterizing the internal circulation therein. The qualitative analysis of the simulated results showed the position of the stagnant zone for a given set of operating conditions. Simulations were also carried out to investigate the reaction kinetics in the slug flow capillary microreactor. Kinetics controlled reaction was modeled in the T junction microchannel and the simulations results were compared with previously published experimental work. Simulation results were in good agreement with the experimental work. It was observed that the smaller dimensions of the reactor provide excellent control over the reaction kinetics.

4.8 Nomenclature

D	Internal channel diameter, mm.
L	Slug length, mm.
t	Time, s.
U	Superficial velocity, ms ⁻¹ .
V	Velocity, ms ⁻¹ .
g	Gravitational acceleration, ms ⁻² .
Bo	Bond Number, dimensionless.
Co	Courant Number, dimensionless.
F	Force, N.
Greek Letters	
θ	Angle, degrees.
σ	Surface tension, Nm ⁻¹ .
ρ	Density kgm ⁻³ .
Δt	Time step
Δx_{cell}	Length interval.
Suffixes	
g	Gas.
l	Liquid.
min/max	Minimum/Maximum.
d	Slug detachment.
curv	Curvature.
surf	Surface tension.

5 Spinning Disc Reactor

5.1 Introduction

Commonly used concepts like “completely mixed” and “Ideal Plug flow Conditions” are nothing more than a *Cliché* to current trends in chemical engineering. In the past two decades researchers have identified major disadvantages in conventional concepts and approaches. For example, if we consider an exothermic multiphase reaction performed in a conventional gas-liquid contactor in a mixing tank equipped with an agitator and a cooling jacket as shown in Figure 35, we can identify that the performance of these contactors are predominantly governed by its size.

In such systems, the surface area per unit volume varies inversely with the vessel diameter [17]. Thus, larger vessels are more difficult to cool, because the heat generated by a reaction under a potential runaway situation is proportional to the vessel volume, whereas, the surface area per unit volume available for dissipating the heat is decreased. Thus, the thermodynamic performance of the reactor is directly influenced by its size. Secondly, the mixing efficiency under a constant impeller speed reduces as the size of the vessels increases. Also, turnover time of the vessel contents increases with its size.

Hence, it is rather easy to achieve higher degrees of heat and mass transfer at a smaller scale than for large scale production. These fundamental shortcomings of the stirred vessel have generated a considerable degree of uncertainty especially when designing high value, fine chemical or pharmaceutical processes for full-scale operation [142]. When a new system is developed conventionally a synthesis paths are developed at lab scales using beakers and flasks. It is then scaled up to a full scale batch operation with capacities ranging from 100 to 1000 tons/year. However, it is worth observing that an output of say 500 tons/year of an active substance corresponds to a continuous process flow rate of around only 70 ml/second. This can be easily handled by a continuous operation in smaller intensified equipments of the size that can be safely operated at laboratory scale without compromising the plant capacities. This approach is commonly known as a “Desktop Continuous Reactor”.

With growing interest in such intensified equipments, a variety of small intensified designs have been put forward in the past decade. One of the promising approaches is to apply centrifugal forces to generate thin, unstable and wavy liquid films over the disc, commonly known as spinning disc reactor. Turbulence within the liquid film enhances the heat and mass transfer characteristics of spinning disc reactor. Particularly when performing fast liquid-liquid reactions such as nitration, sulphonation and polymerization spinning disc reactors have shown special advantages [17]. These reactors have also shown potential benefits in unit operations such as the absorbers, humidifiers, dust collectors, dryers, evaporators etc [18]. SDR has also found various applications in the manufacturing of high value fine chemicals and pharmaceuticals [19].

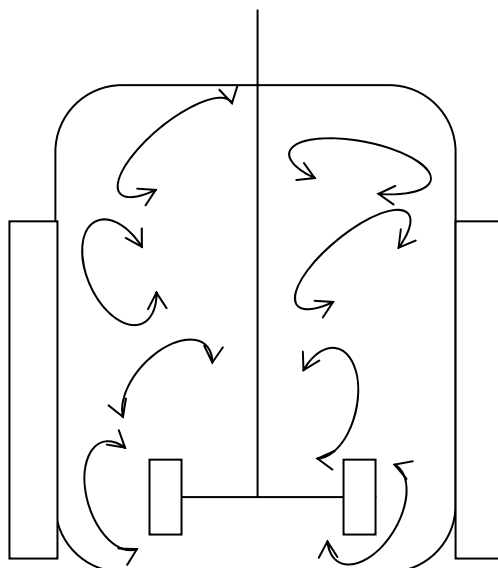


Figure 35 Schematic of agitated vessel fitted with cooling jacket

5.2 Literature Review

Considerable amount of theoretical and experimental investigations has been performed on the transport phenomena of the film flow on the spinning disc [21, 143-150]. Majority of the work has concentrated on the hydrodynamics of the most commonly investigated configuration includes the one with liquid being supplied at the centre of the disc by a falling jet. This configuration maximizes the contact between the disc surface and the liquid, as well as between the liquid and the bulk gas phase above the film. Majority of the investigations have confirmed the findings of Woods [149] experimental results that there exist several wavy regimes in concentric zones across the radius of the disc for a given flow rate, rotational speed,

and liquid properties. Nature of these waves is strongly dependent on the operating conditions and the size of the disc. Espig and Hoyle [147] in their experiments have observed three flow regimes over the spinning disc, namely, the waveless flow, the flow accompanied by axisymmetric wave formation, and the flow comprising combinations of axisymmetric and helical waves [147]. Contrary to these early findings Butuzov and Puhovoi [148] identified not three but four flow regions across the radius of the disc. It was observed that the inlet region had a smooth film surface, followed by a region containing the axisymmetrically travelling waves, the first laminar-wave region, which, in turn, was followed by a turbulent region displaying three-dimensional surface waves; finally, this region was followed by the second laminar-wave region wherein the amplitude of these waves decayed. Similar decay in the amplitude of the waves was also observed in experiments by Charwat et al [146]. Woods [150] photographed the behaviour of a fully wetting dilute film of ink as it travelled over a spinning glass disc. In his experiments, the dependence of the wave characteristics on the system parameters was carefully measured. Woods observed a constant inner film that eventually broke into an array of spiral ripples. Some chaotic waves were also formed at higher disc speeds.

Modelling of the hydrodynamics of the liquid films was first performed in 1916 when Nusselt modeled the downward flow of a condensing liquid film. He assumed that the liquid film falling under the gravity was stable and no shear exists at the gas-liquid interface. But this is not true in case of liquid films forming over the spinning discs. Hence, it is vital to make some modifications into his theory to predict film flow under the influence of the centrifugal force. Espig and Hoyle [147] modelled this class of flow numerically and found that the theoretically predicted film thickness were around 40% less than the experimental values [147]. After this study there has been various correlations developed to describe the stationary waveless flows and their linear stability [151-156] by various researchers based on the asymptotic analysis. Some of these correlations are summarized in Table 20.

Another group of researchers [21, 157, 158] have studied the instabilities of the liquid film and presented numerical methods to elaborate these instabilities. According to the researchers the existing spiral waves were found to be stationary [158]. Matar et al [21] extensively elaborated the phenomena of formation of large finite amplitude waves over the liquid film. They have also suggested numerical equations for the film thickness, volumetric flow rate and total angular momentum.

These equations are not discussed in this work since significant experimental work has been performed on linear liquid films that will be used to validate our CFD model.

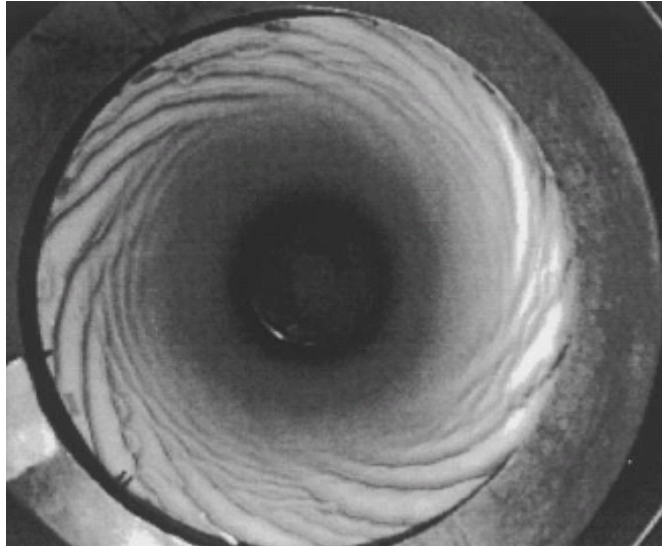


Figure 36 Liquid film behaviour on a rotating disc observed by Woods [150]

Table 20 Various models for liquid flow over spinning discs

No	Researcher	Equation	Comments
1.	Charwat et al [146]	$h = 2h_n \left(\frac{Qv}{r^5 \omega^2} \right)^{1/5}$	<ul style="list-style-type: none"> • Correlation was developed based on experimental values. • Film thickness was measured using optical absorption. • About 50% variance from experimental value and 30-70% variance from Nusselt theory.
2.	Wood and Watts [149]	<p>a) $h_n = \left(\frac{3Qv}{2\pi r^2 \omega^2} \right)^{1/3}$</p> <p>b) $u \frac{\partial u}{\partial r} - \frac{v^2}{r} = -\frac{12\pi^2 r^2 K_1 v}{Q^2} u^3$</p> <p>c) $u \frac{\partial v}{\partial r} + \frac{uv}{r} = -\frac{12\pi^2 r^2 K_2 v}{Q^2} (r\omega - v)u^2$</p>	<ul style="list-style-type: none"> • Two dimensional model. • Nusselt film thickness as described by Wood and Watts. • Assumes fully developed laminar flow over the disc. • Also known as Pigford model.

<p>3.</p>	<p>Lepekhin and Riabchuck [159]</p>	<p>a) $h = 0.886Q^{0.348} \nu^{0.328} \omega^{-0.676} r^{-0.70}$</p> <p>b) $u_r = \frac{w^2 r h^2 \left[1 - \left(1 - \frac{z}{h} \right)^2 \right]}{2\nu}$ [151]</p> <p>c) $h = 0.782Q^{0.333} \nu^{0.333} \omega^{-0.667} r^{-0.667}$</p>	<ul style="list-style-type: none"> • Three dimensional model. • Assumes laminar axis-symmetrical flow. • Inertial forces have negligible effect over centrifugal and coriolis forces. • These two equations for h were compared by Leshev and Peev (2003) [18] experimentally using needle with micrometric watch.
-----------	-------------------------------------	--	--

5.3 Flow characterisations

In general, when experimental investigations are performed there are numerous dependent variables which govern the end results such as the geometrical configurations and varying operating parameters. Hence, it is rather important to perform some sort of quantitative analysis of a problem in terms of dimensionless groups and reduce the number of dependent variables to enhance the generality of the results. The hydrodynamics of the liquids on horizontal spinning discs can be characterized using the dimensionless numbers and parameters detailed in the Table 21. The definitions of those numbers are based on the flow of continuous liquid in the presence of the gas phase

Table 21 Dimensionless numbers for flow characterization in spinning disc

Dimensionless number	Mathematical Formula	Description
Reynolds number	$\frac{Qr}{\nu}$	Ratio of inertial force vs viscous force
Ekman Number	$\frac{\nu}{\omega r^2}$	Relativity of viscous force to coriolis force
Rossby Number	$\frac{U}{\omega r}$	Relativity of inertial force to coriolis force (Can be represented as Ekman number for known Reynolds number)
Weber Number	$\frac{\sigma}{\rho \omega^2 r^3}$	Relative importance of the fluid's inertia compared to its surface tension

In some cases, the coriolis forces are dominant which result in the formation of unstable films on the disc surface. The important dimensionless number for characterization of the flows driven by centrifugal force is the Ekman number, E, which relates the coriolis force to the viscous force. Alternatively, the Rossby number can also represent the effect of inertial force in correspondence with the coriolis force to characterize the film under influence of centrifugal force. Generally, it would be significant to express the flow characteristics in terms of the Rossby number for low Reynolds numbers or highly viscous fluids. Although, in the spinning disc, due to rotational shear, the Ekman

numbers are generally small, therefore, the centrifugal forces are dominant over the viscous forces. Besides, the Weber number is also significant which is due to the gas phase present above the liquid film.

5.4 Computation of film thickness (VOF)

The hydrodynamic behaviour of the film directly influences the heat and mass transfer performance of the spinning disc reactors [20]. The performance of liquid films can be closely related to the falling film theory, and a considerable amount of theoretical and experimental work has been done to evaluate the falling films [21]. But there is still very little understanding on the behaviour of the films under the influence of the centrifugal force. The flow over the rotating disc is characterized by very thin liquid film over the rotating boundary surface with a sharp gas liquid interface that changes continuously in shape. Therefore, in order to reliably design these reactors for industrial scale productions, it is essential to clearly resolve the fluctuating motion of the film. In this study, a computational fluid dynamics (CFD) model has been used to obtain the understanding of the hydrodynamic behaviour of these liquid films under influence of the centrifugal force.

5.4.1 Computational model

Various methods are available for the dynamic characterization free surfaces such as the front tracking, level set, marker particle, shock capturing and the volume of fluid (VOF) [90]. In this study, the VOF formulation was used due to its particular advantages in interface tracking over other approaches. It is also relatively simple and accurate to apply to the boundary fitted grids and accommodates breaking and forming of interfaces. In the VOF approach, a single set of momentum equations is shared by the fluids. The volume fraction of each fluid, in each computational cell, is tracked throughout the domain [83]. The governing equations of the VOF formulation for multiphase flows are listed in Chapter 3. The flow inside the channel was assumed to be incompressible laminar, dominated by the centrifugal forces. It is very important to understand the importance of the grid size when simulating the flows involving very small dimensions.

In the VOF model at a given instance, a cell in the computational domain has either of three conditions; completely filled, or empty or interface. Hence an initial estimate of the

expected minimum film thickness must be made to decide the grid size. In the experimental investigation by Burns et al [20], film thicknesses of around 100 microns were observed. Hence to achieve grid independent solution uniform grid of size 500 micron was created in both 2D and 3D. In 2D, the mapping scheme was used, where unit aspect ratio was maintained, whereas in 3D the Hex-cooper scheme was used where unit aspect ratio was maintained near the disc but gradually increased in the Z direction. Increased aspect ratio in Z direction will not have any effect on the results since the physics of the system suggest that the liquid phase only occupies small heights over the disc.

The spinning disc used in this study, consists of a 30 cm diameter disc. Centre of the disc consists of a recess with 40mm diameter and 2mm height. Liquid (water) was fed to the centre of the disc into the recess through the jet inlet. The jet is situated 10mm above the recess and 8 mm above disc with the diameter of 5 mm. A schematic of the geometry modeled is shown in Figure 37. Computational domain selected for modeling was 30cm in diameter and 10mm high.

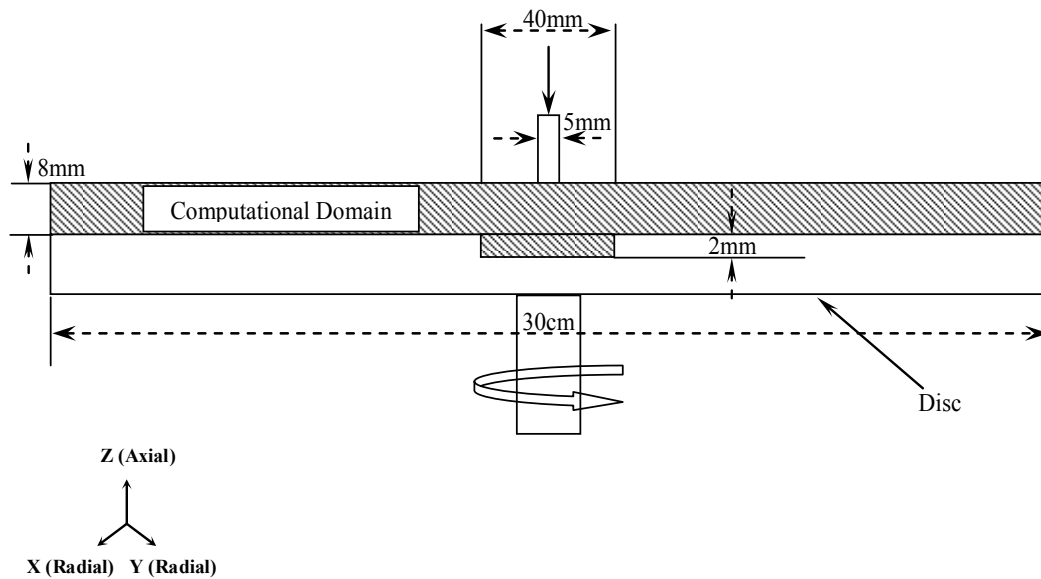


Figure 37 Schematic of the computed domain for model validation

Table 22 Operating conditions for computing liquid film thickness

No.	Parameter	Value
1	Volumetric flow rate	10-18 ml/sec
2	Rotational speed	0-84 rad/sec
3	Liquid	Water
4	Gravity orientation	Horizontal
5	Liquid wall contact angle	30°

A structured mesh was created using GAMBIT and then imported into FLUENT for simulations. Transient simulations were carried out for the operating conditions as described in

Table 22. A velocity inlet condition for the inlet and a pressure outlet boundary condition for the outlet was used with gauge pressure equal to zero (in equilibrium with atmosphere). The PRESTO (pressure staggering option) scheme was used for pressure interpolation. The pressure-velocity coupling was done using the SIMPLE scheme. A second order upwind discretization was applied for the momentum equation.

For interpolating the gas-liquid interface geometric reconstruction scheme was used. Adequate time step (usually 1×10^{-5} s) was used to limit global courant number to 0.25. The results were considered to attain steady state and converged when global mass fluxes were balanced and all the residuals were maintained below 1×10^{-3} . After the steady state was achieved, the time averaged data were collected for a quantitative analysis.

5.4.2 Analytical approach

Various correlations to characterize the liquid film flow over the spinning discs have been proposed in the open literature, some of which are summarized in Table 20. In this work, an analytical model developed by Lepehin and Riabchuk [153, 159] is described and used to validate the CFD results.

Table 23 Simulation parameters for computing liquid film thickness

Parameter	Value
Flow parameters	Laminar Incompressible Isothermal Axis-symmetric Flow - 2D
Boundary Conditions	Inlet - Velocity Inlet Outlet – Pressure Outlet Liquid Wall contact angle specified at wall-disc
Pressure Interpolation	PRESTO (Pressure Staggering Option)
Pressure Velocity Coupling	SIMPLE
Momentum Equation	Second Order Upwind
Interface Interpolation	Geometric Reconstruct
Other	*2D (MRF) Moving Reference frame *3D Wall rotational.

It is assumed that the flow is laminar and axisymmetrical as shown in Figure 38. The inertial forces, weight, surface tension and friction with air have been neglected as they are much smaller than the centrifugal and Coriolis forces. The pressure in the film has been considered constant and equal to that of the surrounding. In a cylindrical coordinate system, with a condition $(z/r) = (h/R) = \epsilon \ll 1$ on the continuity equation, it follows that $V_z \sim V_r \epsilon$. Therefore, the equation of motion may be simplified to:

$$v \frac{\partial^2 v_r}{\partial z^2} - 2\omega v_\phi + \omega^2 r = 0 \tag{48}$$

$$v \frac{\partial^2 v_\phi}{\partial z^2} - 2\omega v_r = 0 \quad 49$$

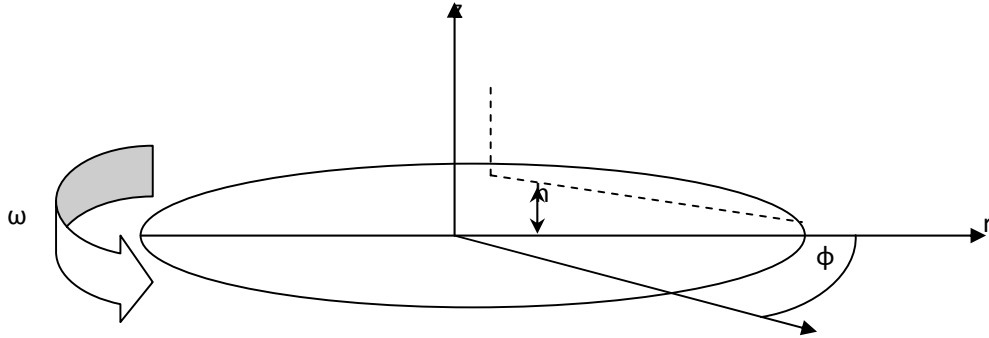


Figure 38 Assumed flow schematic

The radial and azimuthal velocities are given by:

$$v_r = \omega r f_1(\delta)$$

$$v_\phi = \omega r f_2(\delta)$$

where $\delta = z(2\omega/v)^{1/2}$

The solution to equation 48 and 49 given

$$f_1(\delta) = e^\delta (C_1 \sin \delta - C_2 \cos \delta) + e^{-\delta} (C_4 \cos \delta - C_3 \sin \delta) \quad 50$$

$$f_2(\delta) = e^\delta (C_2 \cos \delta - C_1 \sin \delta) + e^{-\delta} (C_3 \cos \delta - C_4 \sin \delta) \quad 51$$

Where the integration constants C_1, C_2, C_3 and C_4 should be determined from the boundary conditions:

$$\delta = 0, f_1(\delta) = 0, f_2(\delta) = 0$$

$$\delta = h_0, f_1(\delta) = 0, f_2(\delta) = 0$$

$$h_0 = h(2\omega/v)^{1/2}$$

Continuity equation in integral form yields:

$$Q = 2\pi r \int_0^h v_r dz = \frac{\pi \omega r^2}{(2\omega/v)^{1/2}} (C_1 + C_2 - C_3 + C_4) \quad 52$$

The numerical analysis of equation 52 performed by Lepehin and Riabchuk shown that:

$$C_1 + C_2 - C_3 + C_4 = 0.2615h_0^{2.87} \quad 53$$

Where from we can derive the equation

$$h = 0.886Q^{0.348} \nu^{0.328} \omega^{-0.676} r^{-0.70} \quad 54$$

Rauscher et al. [151] neglected the terms $2\omega v_\psi$ and $2\omega v_r$ and put forward equation 55 for computing the radial velocity:

$$u_r = \frac{\omega^2 r h^2 \left[1 - \left(1 - \frac{z}{h} \right)^2 \right]}{2\nu} \quad 55$$

Substituting the radial velocity from equation 55 into the integral of continuity equation:

$$h = 0.782Q^{0.333} \nu^{0.333} \omega^{-0.667} r^{-0.667} \quad 56$$

Equation 54 and equation 56 will be used to obtain the analytical values of the film thickness for various operating conditions and compared with the results obtained from CFD. A numerical solution foresees an increase of the film thickness after the liquid supply as a result of the inertial forces. Hence, neither equation 54 or equation 56 predict the hydraulic jump observed by Thomas et al. [160]. But literature suggests that hydraulic jump will not occur for the selected operating conditions investigated in this work [18].

5.4.3 Results and Discussion

5.4.3.1 Comparison of 2D and 3D model

Sometimes, symmetrical flows can be computed over two dimensional flow domain to reduce the computational power required. With an aim to quantitatively study the effect of third dimension on the behaviour of liquid films over spinning disc, computational domain was first converted into a logical 2D axis-symmetrical geometry and then compared with 3D geometry.

It has been found experimentally in literature [18, 20] that the liquid film thickness can reach dimensions of up to 0.2mm. Hence, to track the gas-liquid interface correctly very fine grids must be used. Adversely, this increases the demand on the computational resources. It is easier to tackle this problem in 2D but for 3D geometries grid sizes of up to 1 million elements will be needed, which is difficult to simulate with the available

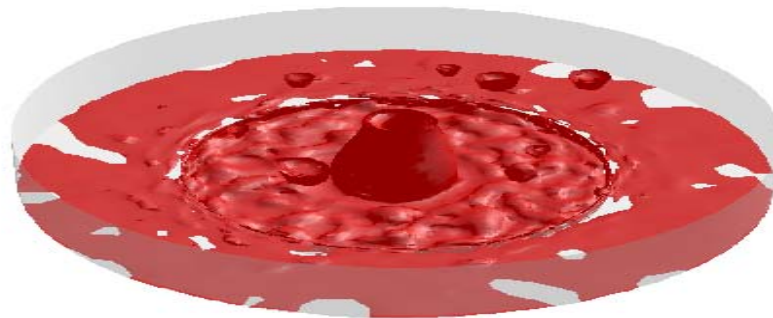
computational resources. A section of the geometry with a radial distance of 3.5 cm from the centre was simulated in 3D and average film thicknesses were computed for several randomly selected points at given radial position. Film thicknesses were calculated for 2D and 3D model and compared with experimentally measured film thickness by Burns et al [20] .

It was found that the results obtained from the 3D model may impose some uncertainties. This was due to the fact that the predicted film flow had characteristic irregularities which was not observed experimentally by Burns et al [20]. Also, the random selection of the data collection points may lead to unreliable information. Whereas, 2D model showed a well known constant linear film with reducing film thickness in radial direction as shown in Figure 39. Although the measured film thickness in case of 3D model was higher than the 2D model due to the uncertainty of the reliability of the 3D results, 2D model was selected for further investigation.



(a)

ζ - Due to large aspect ratio and very small film thickness, a section of radial distance 5cm is shown for quantitative analysis. Disc diameter = 30cm



(b)

Figure 39 Computed volume fraction of water for 2D (a) and 3D (b) model. $Q = 18\text{ml/sec}$, $\omega = 21\text{ Rad/sec}$, 2D radius 15cm, 3D radius 3.5cm.

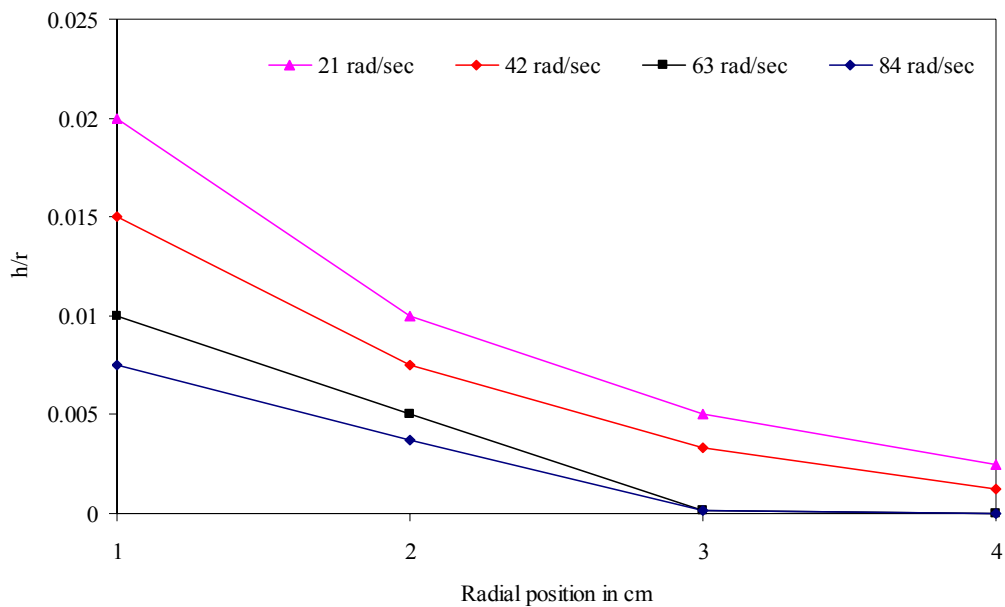
■ - Liquid Phase

Table 24 Measured film thickness in mm

Method	Film thickness in mm
Equation 54	0.232
Equation 56	0.255
Burns et al (Experimental)	0.33
2D model	0.2
3D model	0.36

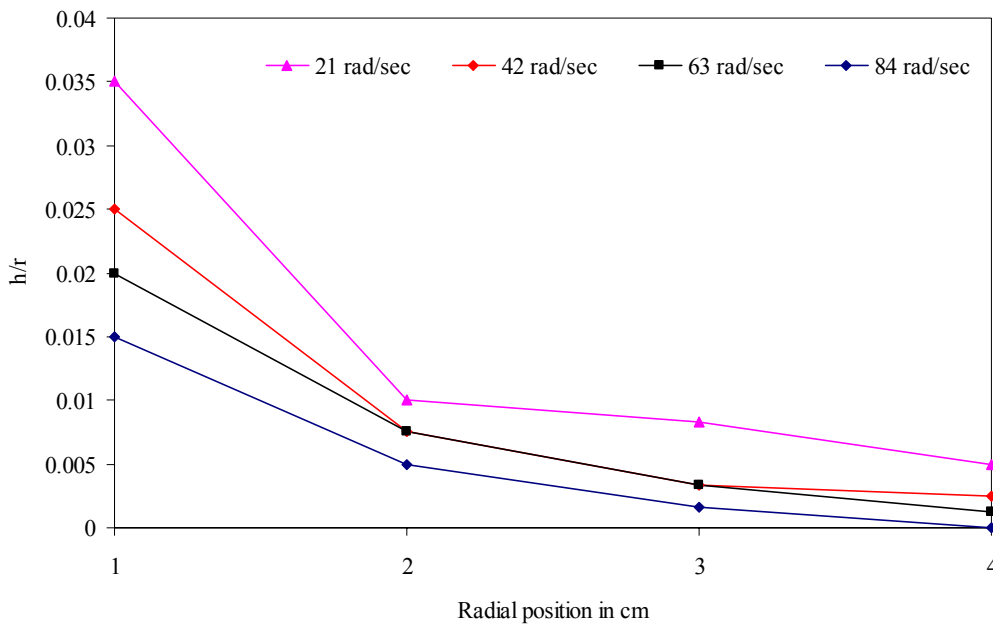
5.4.3.2 Effect of rotational speed

Figure 40 demonstrates the effect of the rotational speed on the calculated dimensionless mean liquid film thickness for various rotational speeds. The profiles indicate that the liquid film thickness is largest near the entrance of the disc and reduces linearly along the radius of the disc. With an increase in the rotational speed, the liquid film thickness reduces. It can be seen from Figure 40 that at 84 rad/sec the liquid film becomes unstable. At higher rotational speeds a constant liquid film collapses as we move away from the centre.



**Figure 40 Effect of rotational speed on the non dimensional liquid film thickness
 $Q = 10\text{ml/s}$ Disc diameter = 10cm**

This is due to the fact that larger centrifugal forces overcome the surface inertial and viscous forces. The resulting film thickness can be incorporated in the Wood and Watts model [149] to compute the radial velocity component within the liquid film [20]. As shown in Figure 41 and Figure 42, simulations with higher liquid flow rates gave qualitatively similar result, albeit with relatively larger film thickness.



**Figure 41 Effect of rotational speed on the non dimensional liquid film thickness
 $Q = 14\text{ ml/s}$ Disc diameter = 10cm**

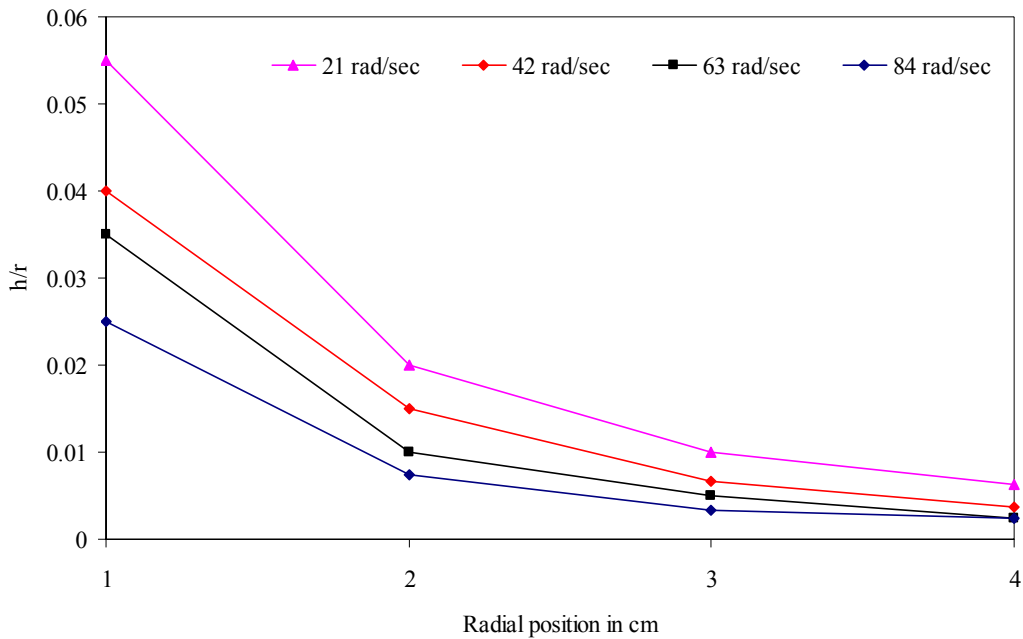


Figure 42 Effect of rotational speed on the non dimensional liquid film thickness
 $Q = 18 \text{ ml/s}$ Disc diameter = 10cm

5.4.3.3 Effect of Volumetric Flow rate

It is evident from equation 46 and 48 that the volumetric flow rate at which the liquid enters at the centre of the disc plays an important role in determining the hydrodynamics of the liquid film. To study the effect of volumetric flow rate on the non-dimensional mean liquid film thicknesses, simulations were carried out at constant rotational speed for uniform disc with a diameter 10cm without the liquid recess. Computed film thickness are compared with the analytically calculated and experimental obtained film thickness by Burns et al [20] and shown if Figure 43.

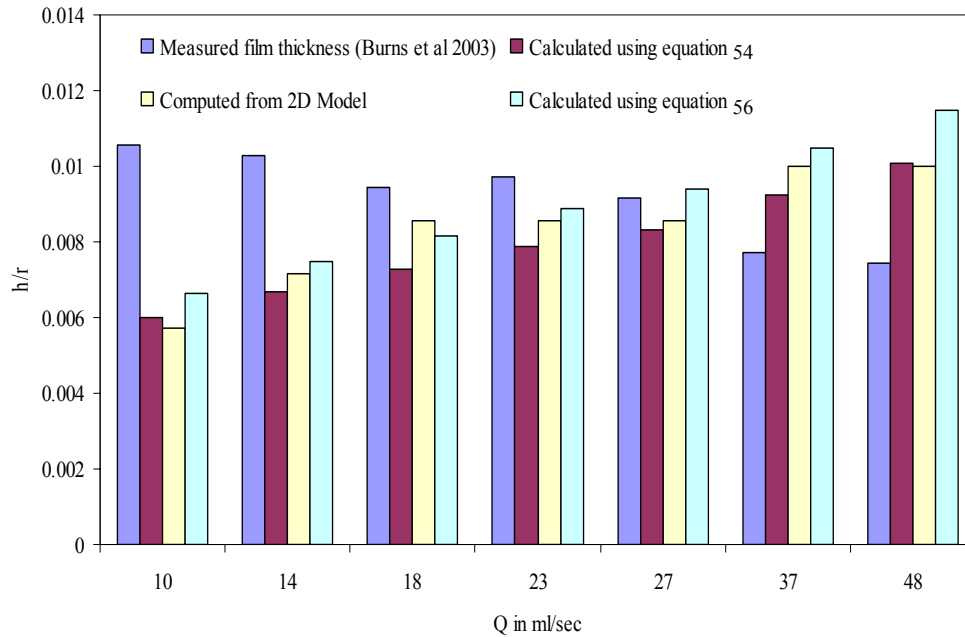
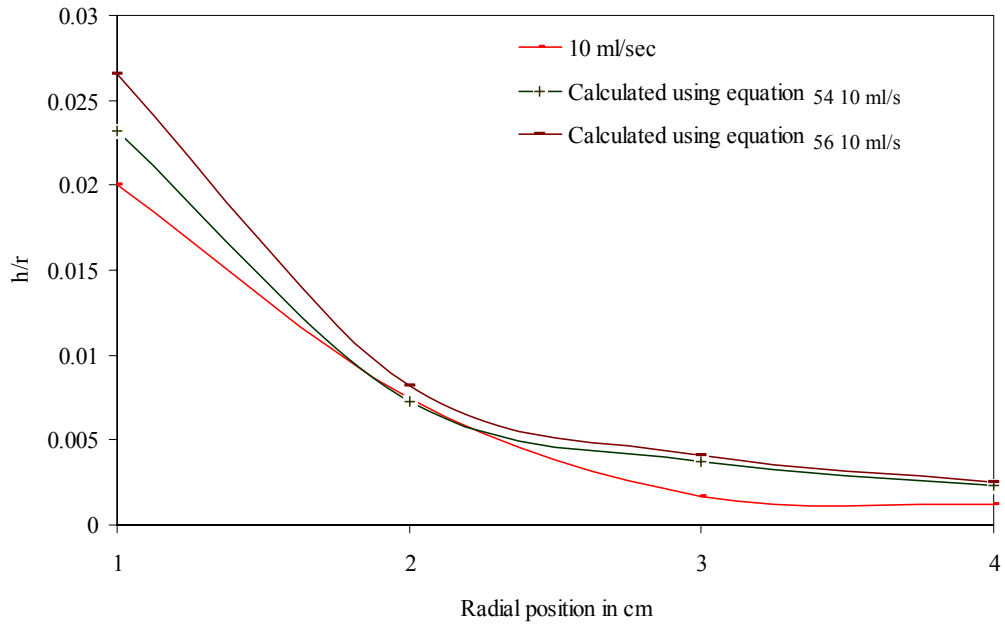


Figure 43 Effect of volumetric flow rate on measured and calculated non dimensional film thickness compared with the experimental data Burns et al.

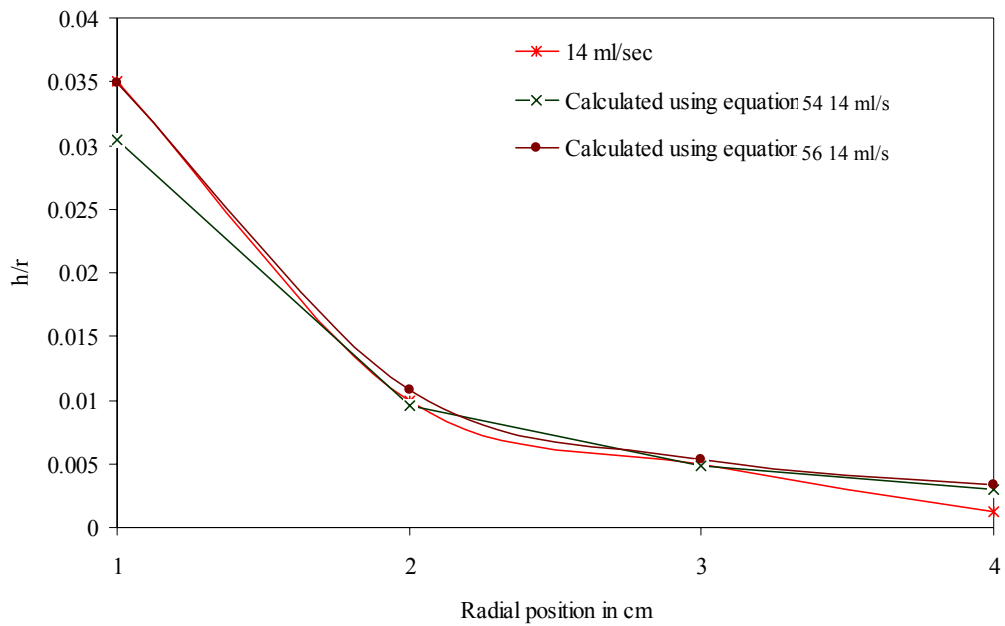
It can be seen from Figure 43 that the results of the CFD are in good agreement with analytical solutions and experimentally measured film thickness. It is evident that equation 54 over predicts and equation 56 under predicts the film thickness. This is because the empirical constants in analytical equations are approximates. But it will appear that the CFD results are more or less close to average values of those obtained with the two equations. In the experimental work by Burns [20] it has been seen that the liquid film thickness reduces with the increase in flow rate. Such phenomenon was not observed in our model. There are various reasons for such phenomenon to occur. One of them could be the presence of liquid recess minimizes the inertial effect at the inlet. Secondly, the film thickness for Burns [20] data listed in Figure 43 were indirectly calculated from the reported average radial velocity using the correlations provided [20]. Therefore, it appears that there is some inconsistency between Burns [20] data and the their correlation.

Figure 44 shows the film thickness as a function of radial position without the presence of recess and it is clear that calculated film thicknesses are similar to those with recess. Hence, subsequent simulations were performed on a 10cm diameter disc without the

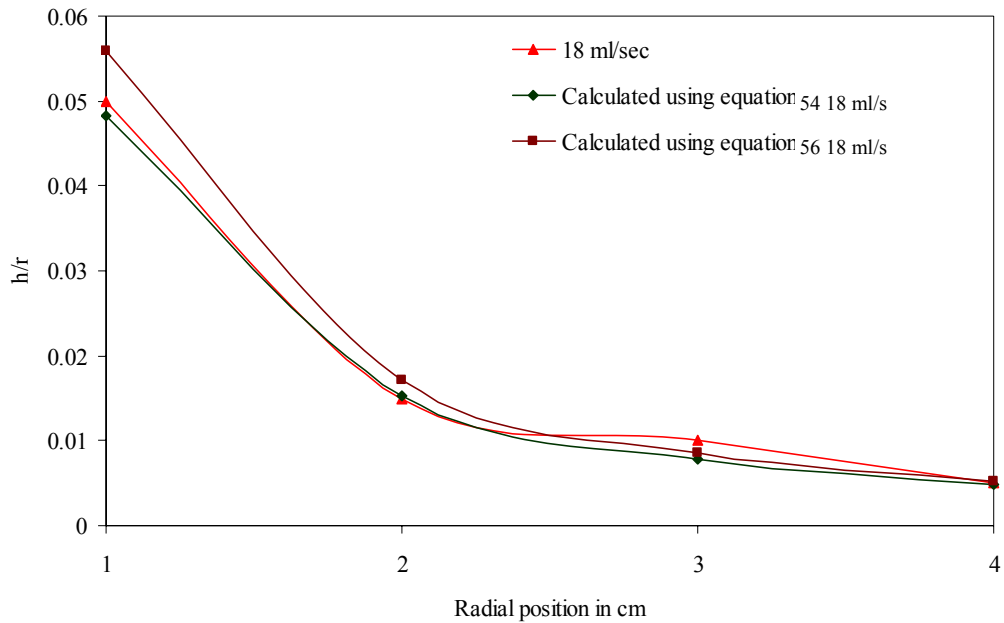
liquid recess at constant rotational speed of 21 rad/sec and varying volumetric the flow rates as shown in Figure 44.



a)



b)



c)

Figure 44. Non dimensional film thickness in a 5cm radius disc for varying volumetric flow rate.

5.4.4 Computation of velocities

To simulate the linear liquid film thickness, a computational domain in the vicinity of the disc was used in the above calculations. In practice, intense centrifugal and shear forces are applied to the fluids in the spinning disc reactor. These forces results in a higher degree of mixing of the fluid even after it have left the disc surface. Therefore, it is important to develop a methodology to analyse the hydrodynamic characteristics of the fluid in a fully developed reactor system. To the best of our knowledge no attempt has been made to understand the hydrodynamics of the fluid after it has left the disc surface. In this section, we attempt to resolve the velocity profiles in and around the disc surface and generate velocity maps for a fully developed three dimensional reactor using the Eulerian-Eulerian multiphase model.

In the Eulerian-Eulerian simulations, separate phases are treated as interpenetrating fluids. This means that at a certain position, all phases can be present with a certain

volume fraction, and no clear interface between the phases. Provided appropriate numerics are defined this model can produce results at significantly less computational power.

5.4.4.1 Phenomenological model

The Eulerian multiphase model in FLUENT allows for the modeling of multiple separate, yet interacting phases [83]. In Eulerian-Eulerian approach the numerical solution of the governing equations for each of the phases is performed in the same way as for single-phase flows. Although the approach may seem simpler but there exists numerical complexity. For example, in single-phase flow, there is one continuity equation and it can be unambiguously used in velocity-pressure coupling algorithms such as SIMPLE or any of its variants [68, 82] but, in the Eulerian-Eulerian framework for multiphase flow there are n-number of continuity equations for n-number of phases. Thus modifications such as phase coupled SIMPLE (PC-SIMPLE) algorithm for the pressure-velocity coupling must be applied. PC-SIMPLE is an extension of the SIMPLE algorithm to multiphase flows. The velocities are solved coupled by phases, but in a segregated fashion. The block algebraic multigrid scheme used by the density-based solver is used to solve a vector equation formed by the velocity components of all phases simultaneously. Then, a pressure correction equation is built based on total volume continuity rather than mass continuity. Pressure and velocities are then corrected so as to satisfy the continuity constraint [83].

In general, the calculation steps involved in the Eulerian-Eulerian model can be summarized as follows:

1. Momentum balance equations are solved for all the phases without the coupling term and in an assumed pressure field.
2. If there are n phases, continuity equations are solved for n-1 phases. This will give volume fractions of all but one phase.
3. The momentum equations is solved again, this time taking into account the interphase exchange term to obtain velocity and pressure profiles.
4. The pressure correction equation is solved using the overall continuity equation

5. The velocity and pressure fields are adjusted, based on the pressure correction in step 4.
6. Step 2-6 are repeated iteratively until convergence is achieved.

Dimensions of the reactor modelled in this work were derived from the prototype reactor SDP-100 developed by Protensive group [161]. This reactor has been extensively used by Professor Colin L. Raston [162] and his fellow researchers to perform ground breaking research in the field of nano-particle technology at University of Western Australia. Some logical modifications were performed in the original design for computational simplification [163, 164].

A schematic of the geometry modelled is shown Figure 45 it consists of the disc with a diameter of 30cm driven by the shaft. Liquid enters near the centre of the disc through the inlet. Outside walls are 5 cm from the disc surface on each side. The geometry was meshed using GAMBIT software, a CFD pre-processor and then imported into FLUENT for simulations.

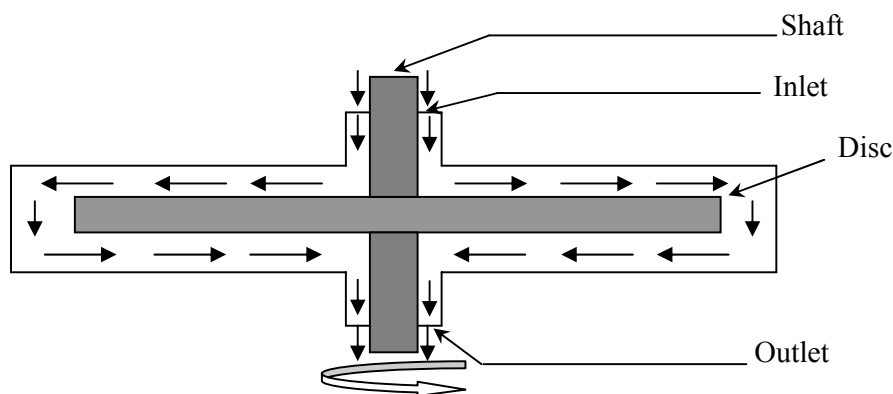


Figure 45 Schematic of the spinning disc reactor used for Eulerian- Eulerian model

Transient simulations were carried out for a given set of gas and liquid velocities. At the outlet a pressure outlet boundary condition was imposed with a gauge pressure equal to zero (in equilibrium with atmosphere). The pressure-velocity coupling was done using the phase-coupled-SIMPLE scheme. In this algorithm, the velocities are solved in a segregated manner but coupled with the phases. A pressure correction equation based on total volume continuity is solved and pressure and velocities are then corrected so as to satisfy the continuity constraint [83]. In finite volume, when the generic transport

equation is integrated over a control volume, very often the resulting equation contains the face values of a variable ψ (ψ_e, ψ_w, ψ_n and ψ_s) (Figure 6). These variables should be expressed in terms of the nodal values of the variable ψ (i.e., $\psi_E, \psi_W, \psi_P, \psi_S$ and ψ_N).

FLUENT provides several choices of algorithms to accomplish this task including first and second order upwind scheme, and QUICK (quadratic upstream interpolation for convective kinetics) [77]. Second order upwind discretization was applied for momentum and volume fraction equation. These parameters are detailed in

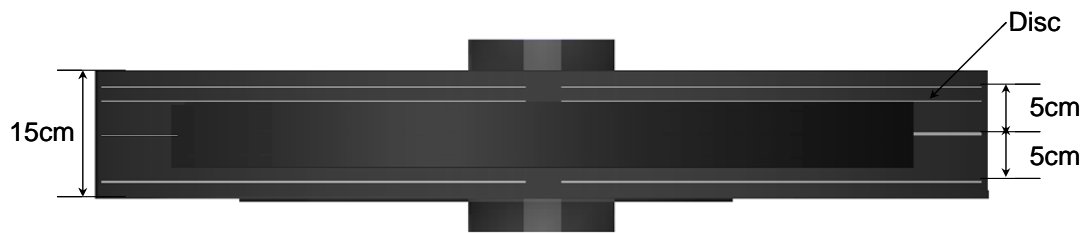


Figure 46 Sections of geometry for velocity mapping

Table 26 given below.

Geometry was divided into three sections, axially equidistant from each other as depicted in Figure 46. Another section was created just above the disc to elaborate the fluid performance on the disc. Liquid was introduced through the inlet at a constant superficial velocity and the disc speed was varied to investigate the influence of rotational speed on the steady state velocity that fluid attained.

Table 25 Operating parameters (SDR)

No.	Parameter	Value
1	Superficial Velocity	0.1 m/sec
2	Rotational speed	0-300 RPM
3	Liquid	Water
4	Gravity orientation	Horizontal

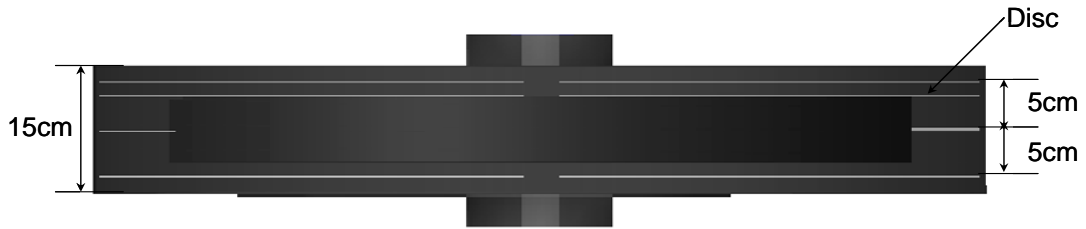


Figure 46 Sections of geometry for velocity mapping

Table 26 Simulation parameters for Eulerian-Eulerian model.

Parameter	Value
Flow parameters	Laminar
	Incompressible
	Isothermal
Boundary Conditions	Inlet - Velocity Inlet
	Outlet – Pressure Outlet
	3D Wall rotational.
Drag coefficient	Morse Alexander
Pressure Velocity Coupling	Phase Coupled SIMPLE
Momentum Equation	Second Order Upwind
Volume Fraction	Second Order Upwind

Simulations were performed for a stationary disc and the one rotating at 300 RPM and. Steady state converged results were obtained; velocity vectors on the disc surface were generated and are qualitatively compared in Figure 47. It can be observed from Figure 47 that the tangential velocities remain constant for a given radial position whereas the velocity changes significantly as liquid moves away from the centre of the disc. The Velocity was highest at the tip of the disc and lowest near the entrance.

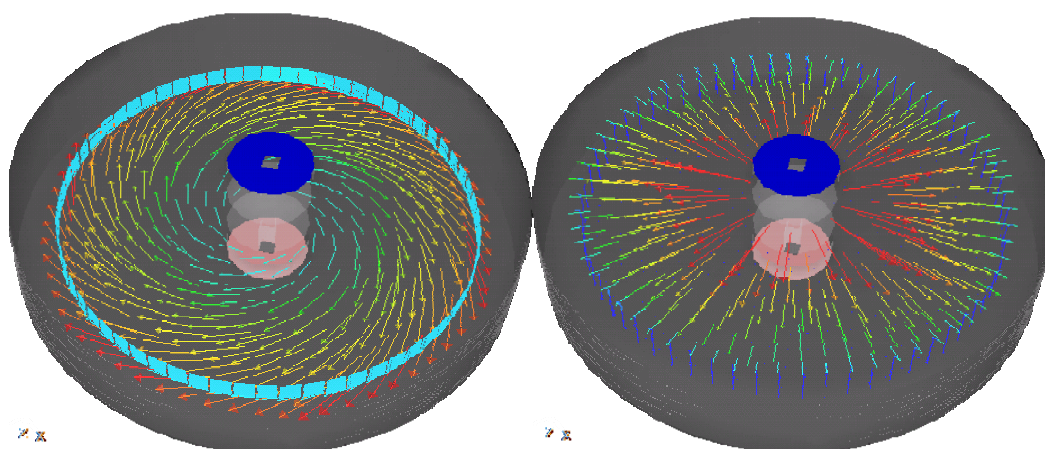


Figure 47 Velocity vectors rotational speed 300 RPM (Left) and 0 RPM (Right)

The flow in the SDR can be classified into four main zones as described below:

1. Acceleration zone: the region above the disc and below the inlet of the liquid.
2. Disc spin-up zone: the flow regime over the disc.
3. Central mixing zone: the region between the disc wall and the outer wall.
4. Disengagement zone: the liquid disengagement zone below the disc surface.

Depending on the liquid and gas holdups and hydrodynamic characteristic of all the above mentioned zones can be significant. For example, if multiphase gas to liquid fast reactions is performed in the SDR, it is extremely important consider the overall mixing to be able to predict reactor behaviour. Whereas, for the single phase kinetics driven slow reactions performed on an immobilised catalyst over the spinning disc, it would be significant to elucidate the disc spin-up zone. But in this work, we have presented a versatile model that can provide important hydrodynamic characteristic at all of the above mentioned zones.

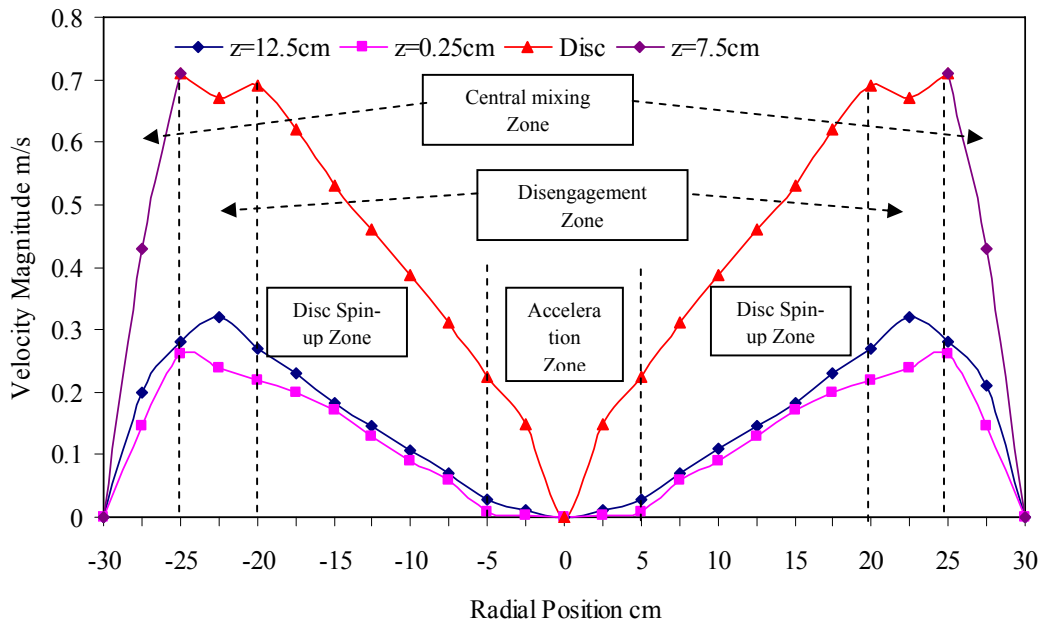


Figure 48 Velocity profile along the radial distance for varying axial lengths. $U = 0.1$ m/s Disc Speed = 300 RPM

Velocity profiles were generated for all the zones and time average data is reported in Figure 49, Figure 50 and Figure 51. After comparing the raw data for the velocity profiles in the acceleration zone and disengagement zone for different rotational speed it can be confidently concluded that the fluid in acceleration zone is under greater influence of the centrifugal shear created by the disc surface. It was observed that the velocities in the acceleration zone were approximately 15-20% greater than the velocities in disengagement zone. Also, in the central spin-up area, the liquid behaviour was influenced by a number of small voids and at some instances phenomenon of instantaneous micro bubbling was also expected. Although, due to the limitations of the eulerian-eulerian model such micro bubbling may not be reproducible. But due to the breaking of the liquid film from the disc surface, larger interfacial areas are expected. The reported velocities near the disc wall were consistent with the velocities reported at the tip of the disc surface and did not change significantly along the axial length of the wall.

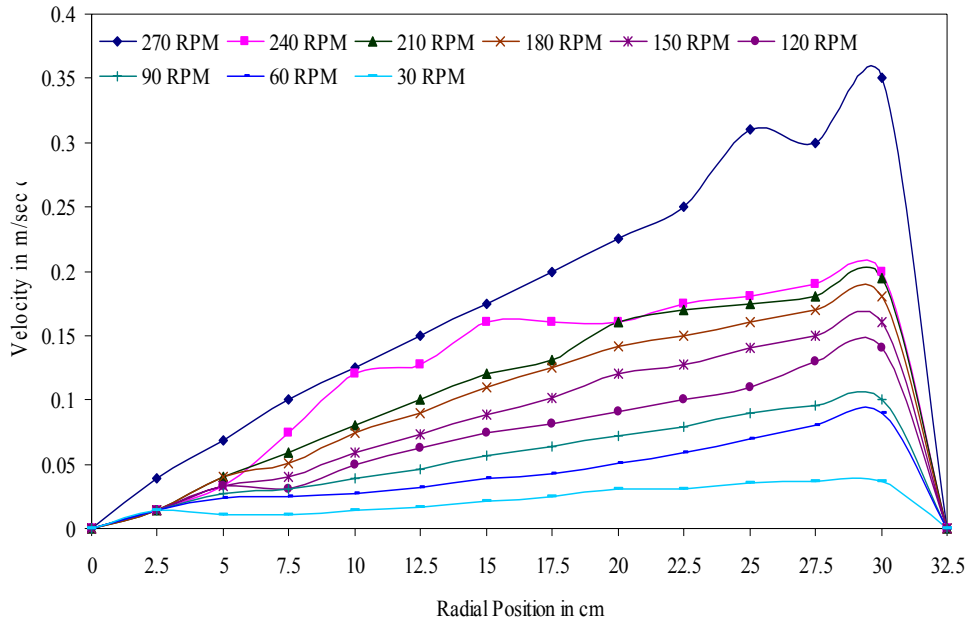


Figure 49 Velocity profile at Z=2.5cm for varying disc speeds.

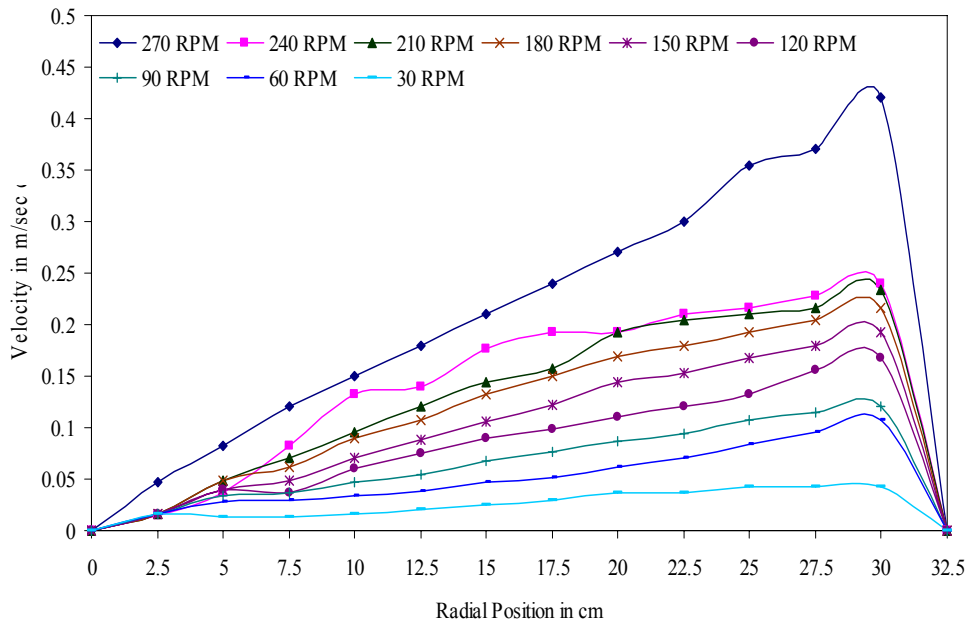


Figure 50 Velocity profile at Z=12.5cm from inlet for varying disc speeds.

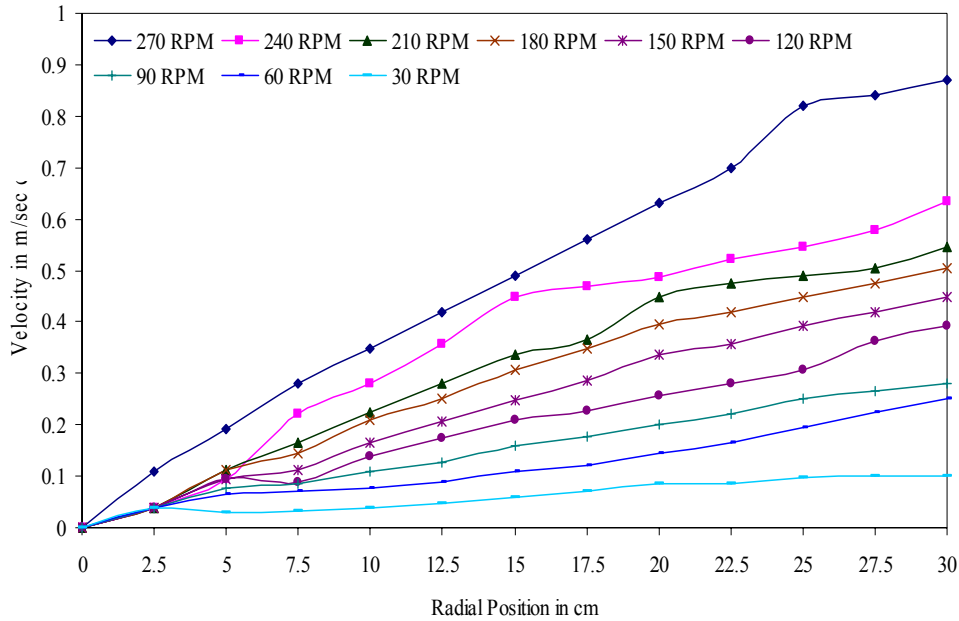


Figure 51 Velocity profile on the disc for varying disc speeds

5.5 Summary

The volume of fluid and Eulerian-Eularian multiphase models were used to study the film hydrodynamics of a fully developed spinning disc reactor. The effect of various operating parameters on the film dynamics was also studied. It was observed that the analytical correlations produced only approximate values of the film thickness. However, CFD simulations predicted the liquid film thicknesses that were in good agreement with previously published experimental data. It was also observed that the physical and operating parameters predominantly controlled the nature of the liquid films produced over the horizontal spinning disc. Fully developed velocity maps suggest that there are immense centrifugal, shear and inertial forces acting on the fluid disengaged from the disc surface. These forces result in a higher degree of mixing in various zones on and around the disc surfaces. Also both viscous and surface tension forces were negligible compared to the coriolis and centrifugal forces, thus macro and micro bubbles were formed freely, which resulted in a enhancement in the specific interfacial areas.

5.6 Nomenclature

Q	Volumetric flow rate. m^3s^{-1}
h	Film thickness, m.
L	Liquid.
D	Disc diameter, m.
r	radius, m.
P	Pressure, Pa.
t	Time, s.
u, v, w	Velocity components in x, y and z direction, ms^{-1} .
V	Velocity, ms^{-1} .
K	empirical constant.
g	Gravitational acceleration, ms^{-2} .
Greek letters	
μ	Dynamic viscosity, $\text{kgm}^{-1}\text{s}^{-1}$.
ν	Kinematics viscosity
σ	Surface tension, Nm^{-1} .
ρ	Density kgm^{-3} .
Suffixes	
r	radial component.
n	Nusselt component.

6 Rotating Tube Reactor

6.1 Introduction

A rotating tube reactor (RTB) is an intensified reactor that uses centrifugal forces to spread thin liquid films of reactants and improve the mixing characteristics. The concept is inspired from the special advantages of film produced in the spinning disc reactor. Thin liquid films are produced in the annulus of the RTB along with the intense mixing. A major difference between the spinning disc and the rotating tube is the retention time of reactants. In the spinning disc reactor the residence time of the reactants can only be controlled by altering the disc speeds [165]. Whereas, in rotating tube reactor residence time is independent of the rotational speed. Also, in the SDR, the centrifugal forces applied to the reactants causes the reactants to move off of the disc quickly, but in the RTB the rotation of the tube swirls the reactants inside the tube, around the longest axis. The RTB can exhibit several advantages such as, an improved controllability over the reactant retention times, improved mixing efficiencies, very little or no back mixing, flexibility to operate either in batch-wise or continuous operation etc.



Figure 52 Image of the tube reactor [162]

Figure 52 shows an image of a prototype rotating tube reactor developed by Professor Roshan Jachuck, Chemical Engineering Department, Clarkson University, NY, USA [162]. Annulus rotational techniques have been previously been utilized to enhance the performance of a processing unit. Some of the apparatus that have previously been developed include rotating packed bed reactor, rotating perforated tube reactor, rotating brush bio-film reactor, cylindrical annulus chromatographic reactor etc. [17, 27, 166-169]. In general, a majority of these techniques have been applied to mass transfer controlled slow reactions. Some of the major applications includes; the rotating cone reactor for the pyrolysis of coal [170], for bio-film processing [171], growth of diamond films by hot filament chemical vapour deposition (HFCVD) utilising rotating substrate reactor [172]. The rotating tube reactor shown in Figure 52 is the first one of its type and has never been investigated before. Thus a complete CFD analysis was performed to provide a foundation for the future development of this reactor type.

6.2 Computational Model

There are two aspects to the flow problem in a rotating tube. Firstly, a constant thin liquid film is formed on the surface of the rotating wall. Secondly, it is important to

characterize the mixing performance within the annulus of the tube. Modeling both the phenomenon simultaneously adds complexity to the problem. Hence, in this work single phase steady state simulations were performed to evaluate the mixing characteristics in the rotating tube. Also, currently there are no experimental data available to benchmark the numerical model.

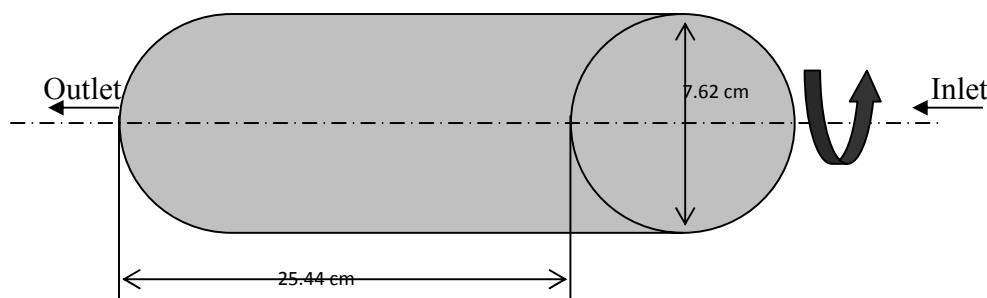


Figure 53 Schematic of the rotating tube used for computational model

6.3 Model Geometry

Model geometry had a horizontal cylindrical tube as shown in Figure 53. It consists of a hollow tube with a diameter of 7.62 cm and length 25.44cm. Reactants are fed through the velocity inlet and propagate through the annulus of the tube. The tube walls are rotated using a central motor. In the annulus of the reactor, strong centrifugal forces are applied due to the rotation of the tube wall. Products are discharged through the pressure outlet. In the computational domain the rotational effect was generated by defining the circular motion on the wall. To model a simple reaction (ethylene-air oxidation), inlet was modified as shown on Figure 56. Air and ethylene were fed separately to the reactor and the product concentrations were calculated at the outlet.

6.4 Simulation Parameters

A structured mesh was created using GAMBIT and then imported into FLUENT [83] for simulations. Simulations were carried out for operating conditions as described in Table 27. PRESTO (pressure staggering option) scheme was used for pressure interpolation. The pressure-velocity coupling was done using the SIMPLE scheme. Second order upwind discretization was applied for momentum equation. The results were considered to attain steady state and converged when global mass fluxes were balanced

Table 27 Operating conditions (RTB)

No.	Parameter	Value
1	Superficial liquid velocity	40 mm/sec
2	Rotational speed	0-500 RPM
3	Liquid	Water
4	Gravity orientation	Horizontal
5	Other	Species: Air-ethylene (reaction)

Table 28 Simulation parameters (RTB)

Parameter	Value
Flow parameters	Laminar Incompressible Isothermal
Boundary Conditions	Inlet - Velocity Inlet Outlet – Pressure Outlet
Pressure Interpolation	PRESTO (Pressure Staggering Option)
Pressure Velocity Coupling	SIMPLE
Momentum Equation	Second Order Upwind

6.5 Results and discussion

In this work, two sets of simulation were carried out. Firstly, single phase simulations were performed to elaborate the hydrodynamics. Velocity profiles were generated at two different rotational speeds. Then air-ethylene reaction was conducted in the model reactor to study the effect of rotation on the propagation of the reaction.

6.5.1 Hydrodynamics

A fully developed velocity profile shown in Figure 54 indicates that the fluid achieves its maximum velocity near the wall. The effect of the centrifugal force is largest near the rotating boundary and lowest at the centre of the tube.

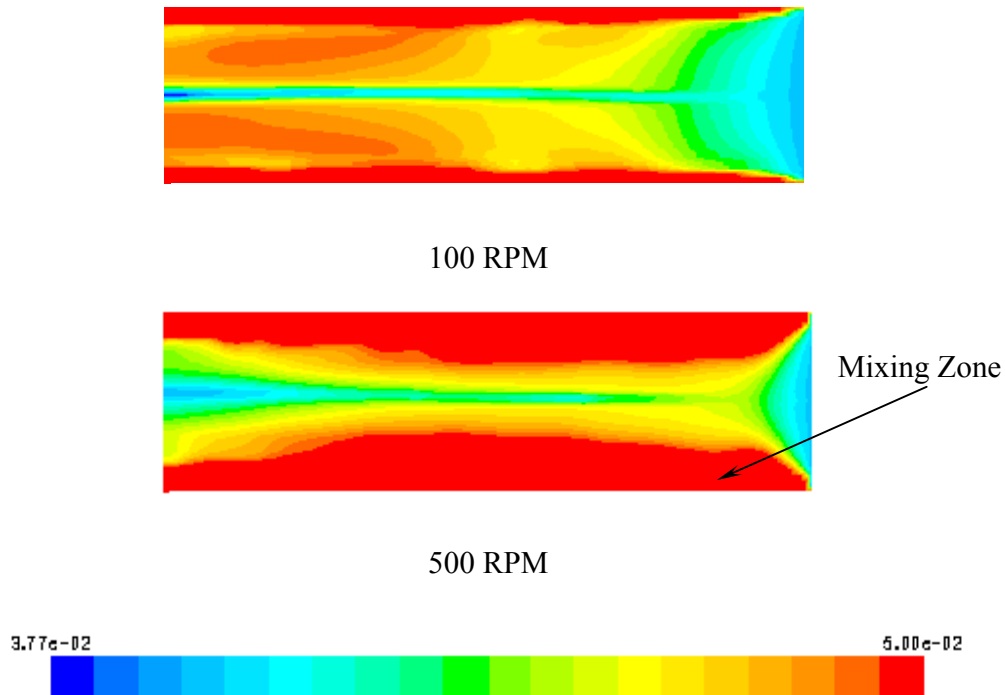


Figure 54 Effect of rotational speed on the velocity profiles $U = 40\text{mm/sec}$

The velocity profile along the radial distance is hyperbolic in nature. As the rotational speed is increased the thickness of the so called mixing zone increases. Consequently, in practice it will also be expected that with the increased rotational speed, the liquid film thickness will reduce. To obtain further insight into the hydrodynamic performance particle trajectories were also generated for the rotating tube and are shown in Figure 55, it can be seen from the particle trajectories that the liquid entering near the wall is likely to spend the maximum time in the tube. Furthermore, it is important to note that the larger coriolis forces must be generated to impose a constant liquid film along the wall of the rotating tube.

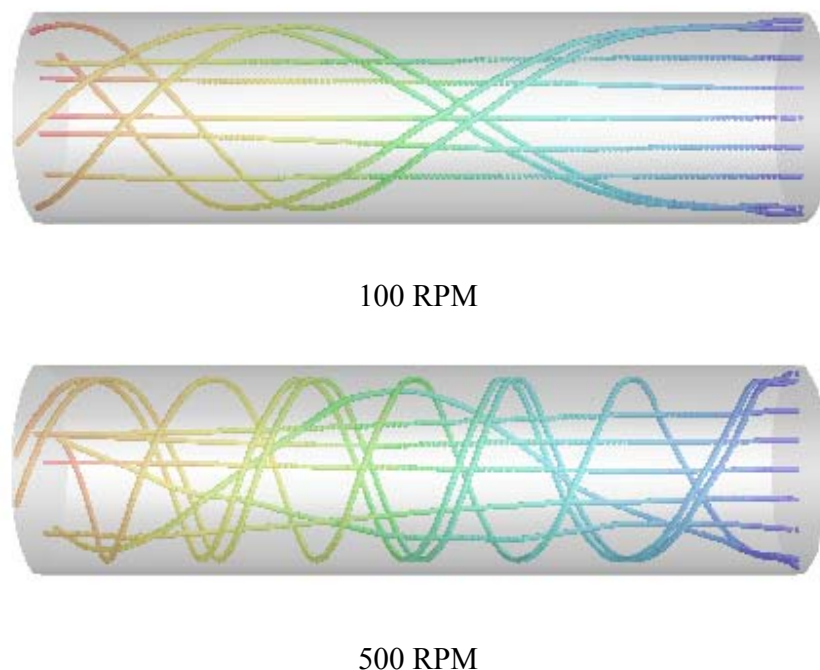


Figure 55 Particle trajectories for rotating tube at varying rotational speed $U = 40\text{mm/sec}$

6.5.2 Modelling of chemical reaction

A simple chemical reaction was simulated in the rotating tube reactor and its performance was compared with the stationary tube reactor. Reaction used for this study is a very well known air-ethylene reaction:

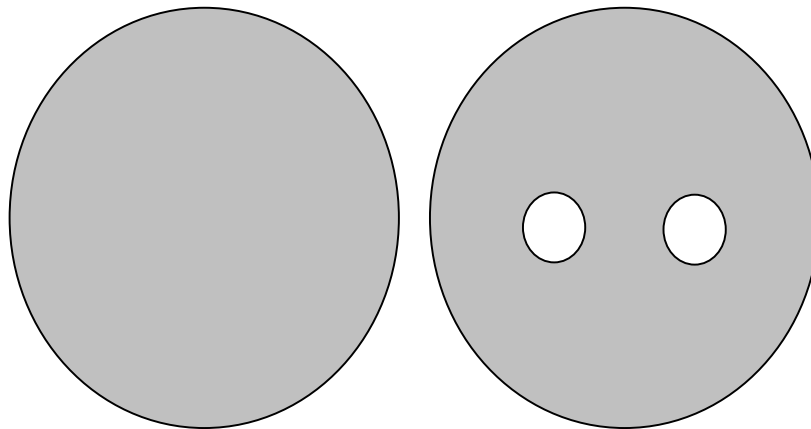


The reaction was assumed to be volumetric, laminar and finite rate. Operating and simulation parameters are detailed in Table 29

Table 29 Operating and simulation parameters of modelling chemical reaction in RTB

No.	Parameter	Value
1	Superficial velocity	Air- 0.1 m/sec Ethylene – 0.1 m/sec
2	Rotational speed	0-200 RPM
4	Gravity orientation	Horizontal

It can be seen from Figure 57 that for the stationary tube the length of the reactor required for the reaction to be complete is approximately 20 cm. Whereas, when the reactor tube is rotated at 200 RPM the same level of conversion can be achieved in about 5cm of the reactor length. Figure 58 demonstrates the particle trajectories for fixed air and ethylene superficial velocities in the stationary and rotating tube reactor. The intense mixing phenomenon is observed when the tube is rotated. It is clear that due to this mixing, the reactor performance is enhanced.



Inlet 1 for simulating hydrodynamics

Inlet 2 for simulating chemical reaction

Figure 56 Inlet configurations

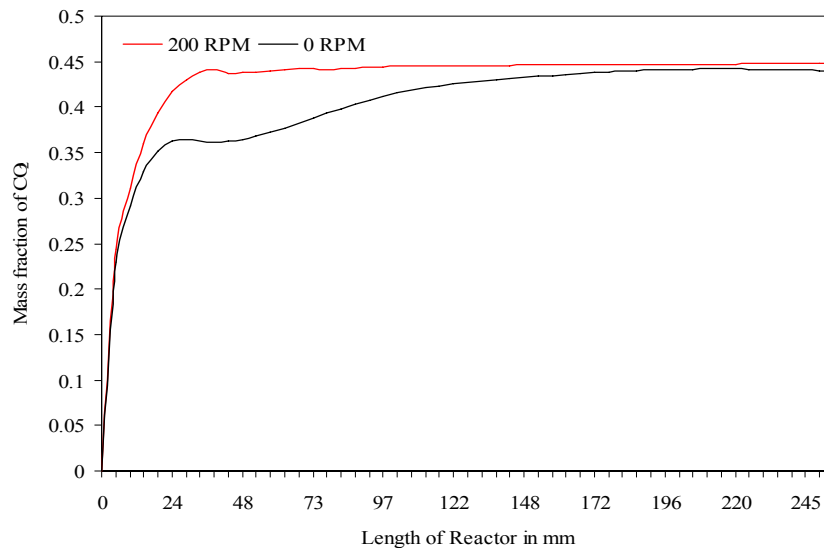


Figure 57 Mass fraction of CO₂ along the length of the tube.

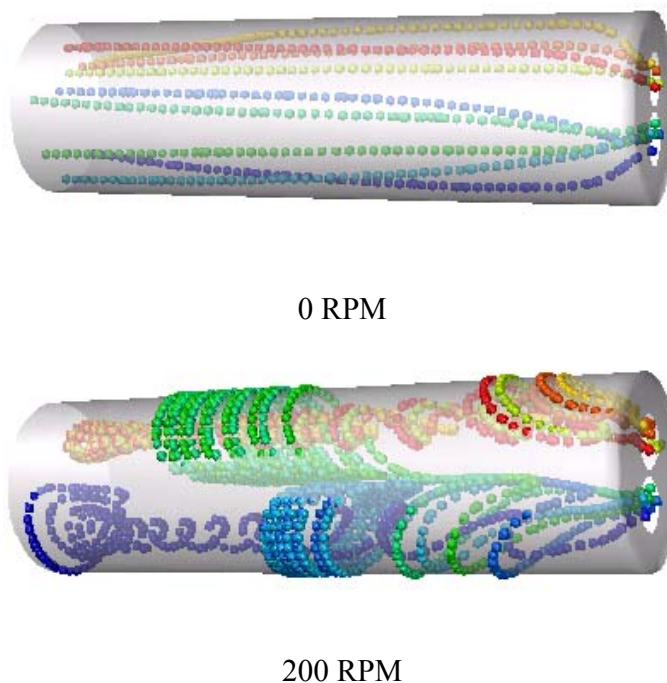


Figure 58 Particle trajectories varying rotational speed $U_{air} = 0.1$ m/s, $U_{ethylene} = 0.1$ m/s

6.6 Summary

In this work, a CFD analysis has been performed to understand the chemical kinetics and the hydrodynamics of a rotating tube reactor. Simulation results showed that the rotation of the tube had a significant effect in improving the reactor performance by large magnitudes. Although the mixing characteristics of the rotating tube are dominated by the physical properties (e.g., density and viscosity) of the fluid, the short-circuiting in fluid element progressively decreased on increasing the rotation speed (Figure 55). Because of the decrease in the short-circuiting, the net amount of conversion per pass from the reactor increased significantly on increasing the rotation speed (Figure 58).

More detailed numerical models and experimental evidence will be required to predict the other important hydrodynamic attributes, such as the liquid film thickness, which will be the subject of future studies.

7 Conclusions and Future Developments

Hydrodynamic and reaction characteristics of three novel multiphase reactors were studied as potential process intensification tools. Detailed quantitative and qualitative analyses were performed on a capillary micro reactor and a spinning disc reactor for multiphase applications. CFD analysis was also performed for rotating tube reactor as a possible alternate for the spinning disc reactor.

7.1 Capillary Microreactor

7.1.1 Hydrodynamics

The hydrodynamic characteristics of the slug flow capillary microreactor were studied using CFD simulations. Both 2D and 3D simulations were performed, and the effect of various fluid and operating parameters were analysed. The effect of gravity was studied, by measuring the difference in axial length of mixing zone for horizontally and vertically mounted microchannels. Various inlet geometries and channel diameters were also investigated. Some of the major conclusions drawn are:

1. Predicted mean gas and liquid slug lengths were found to be in good agreement with the previous published results by Qian and Lawal [105].
2. Pressure profiles due to the shape of the slugs were generated and compared with the Young Laplace theory. It was observed that the calculated and theoretical values of Laplace pressure were consistent with the Young-Laplace Theory [104].
3. It was concluded that to decrease the slug length and increase the number of slugs per unit length of the channel it is advisable to introduce the gas feed at an angle smaller than 90° to the channel.
4. The smaller the channel diameter, the smaller is the slug length and more number of slugs are produced per unit length of the channel.
5. It has been shown by Qian and Lawal that with the increase in U_1 , the mean gas slug length L_g decreases. Our CFD model generated similar results.
6. It was observed that the liquid wall contact angle determined the shape of the slugs.

Internal recirculations within the gas bubble and liquid slugs were separately modelled using a two-dimensional single phase CFD model. Proposed methodology provides significant information about the velocity profile and flow regimes within the gas bubbles and liquid slugs. Velocity profiles within the liquid slug suggest a fully developed flow, which is parabolic in nature. It was also observed that when the slug moves through the capillary, due to the shear between the slug axis and the capillary wall, the liquid in the centre moves to the front end of the slug, where it touches the front interface and returns back along the wall of the capillary while at the back end, the liquid moves from the wall to the centre of the slug resulting into internal recirculations. Thus, the velocities are highest near the wall and at the axis of the slug, which forms a stagnant zone between the axis and the wall of the slug. This stagnant zone exists in both the gas bubble and liquid slugs.

7.1.2 Chemical reaction

Simulations were also carried out to investigate the multiphase chemical reaction kinetics inside a capillary reactor. The formation of H_2O_2 using the DC process involves four simultaneous reactions (synthesis of H_2O_2 , synthesis of water, decomposition of H_2O_2 , and reduction of H_2O_2 by H_2), the overall reaction kinetics must take into account the individual kinetics of these reactions. In this work, we have modelled the reaction kinetics for the reduction of H_2O_2 by H_2 . The CFD model comprised of Navier-Stokes equation with spatially resolved viscosities and densities and species transport equations for individual species was used to obtain the chemical species concentrations profiles for all the reactant and products. The resulting overall mass fractions were compared with the kinetics data obtained experimentally by Voloshin and Lawal [127]. The calculated concentration profiles, the overall mass fraction and reaction rates were in good agreement with the previously published data. In this work, we have incorporated extrinsic kinetics for H_2O_2 reduction in computational fluid dynamics framework. It was observed that gas-liquid microreactors offer superior performance and greater efficiency in comparison to the conventional equipments.

7.2 Spinning disc reactor

A computational fluid dynamics model was developed to characterize the hydrodynamics of this reactor. Simulations were conducted both in 2D and 3D manner. Although 2D axisymmetric simulations were unable to predict the wavy nature of the liquid film, they predicted other hydrodynamic characters reasonably accurately, particularly at low rotational speeds where only uniform films have been reported. However, for larger Ekman numbers, it may be essential to conduct 3D simulations. When 2D and 3D models were compared with the analytical and experimental values from the literature, they both predicted the liquid film thickness and radial velocities which were in good agreement with the previously published data. The effect of various simulation, operating and physical parameters on the hydrodynamics behaviour of liquid films over spinning disc was also studied. It was observed that the film thickness profile for the spinning disc is a complex phenomenon but our model was adequate to capture all of the important hydrodynamic characteristics. Some of the major conclusions from this study can be summarized as follow:

1. A combination of the VOF and Eulerian-Eulerian approach were used to develop a complete flow mapping in a fully developed spinning disc reactor.
2. At lower rotational speed, the film thickness gradually decreased with increase in the flow rate, whereas at higher rotational speed, due to the shear force exerted over the liquid almost constant liquid film thicknesses could be achieved.
3. The computed radial velocities were highest at the tip of the disc and lowest near the centre.
4. Complete velocity maps were developed for various rotational speeds in a fully developed spinning disc apparatus, and the results were consistent with the earlier studies.

7.3 Rotating tube reactor

It was observed that the mixing characteristics in the rotating tube were dominated by the physical properties of the fluid. Gas phase reacting mixture was modelled using the species transport reaction model. Single-phase water simulations were also carried out to study the effect of physical properties on the reactor performance. CFD analysis showed that when water was used at lower rotational speeds there was some degree of short-circuiting whereas, for gas phase even at low rotational speeds intense mixing was achieved. Physical properties of the fluid determine the optimum operating conditions required in the rotating tube reactor. Simulation results showed that the rotational effect is significant and can improve the reactor performance by large magnitudes. More detailed numerical model or experimental evidence will be required to predict the other important hydrodynamic characters of the liquid films.

7.4 Open questions

7.4.1 Microreactor

Although a fully developed 3D model predicted the effect of various operating and geometric conditions, a separate technique was required to predict the internal recirculation. Therefore, one of the open questions here is to develop a methodology that can resolve the internal circulations in the native 3D simulation. Further research can

also be carried out in improving the computational power and simplifying the multiphase modelling numerics.

Although there is ample amount of qualitative data available in the literature for comparison, there is a lack of quantitative analysis in this field. Further experiments are required to characterize the internal circulations quantitatively.

7.4.2 Spinning disc reactor

When 3D model was used, wavy films of varying amplitudes were observed. The question here is to determine a methodology that can predict these wavy flows either in a 2D domain which does not require computational power or quantify the 3D domain to produce quantitative data.

Spinning disc in this work was assumed to be smooth and flat with very low roughness. But in practice, various types of surfaces are used, such as those with single or multiple grooves, to enhance the mixing within the waves. Such complexities are difficult to model since the size of the groove is very small compared to the size of the disc resulting in disparate length scales. More research is required to address this issue.

7.4.3 Rotating tube reactor

CFD simulations have been performed to qualitatively describe the hydrodynamics of this reactor but there are no experimental data to understand the complexities of the reactor.

The above discussion shows some open questions on the hydrodynamics of all the three reactors studied in this research, and below are some specific recommendations for future work.

7.5 Recommendations for Future Work

7.5.1 Capillary Microreactor

Fischer-tropsch reaction: Fischer-Tropsch synthesis is a multiphase process that allows for gaseous hydrocarbons, such as natural gas to be converted into liquid hydrocarbons, such as diesel and methanol. Unlike fuels derived from the refining of crude oil, the synthetic fuels obtained via the FT synthesis are generally much more environmentally

friendly, as they contain virtually zero sulphur and are low in aromatics. As natural gas is available in abundance in remote onshore and offshore locations so its best use could be to produce liquid fuels, which are greater in demand and easy to handle and transport than the gas itself. But the problem lies in designing such a commercialized high capacity reactor, which can be installed on an off shore location. The purpose of the future research must be to develop a scale up to industrial scale F-T microreactor that can deliver commercial production with reduced size to be able to be installed at remote onshore/offshore locations.

Industrial system of kilogram scale production: There are several pharmaceutical and specialty chemicals, which are manufactured in the range of kilogram per hour, or even less than that. Conventionally, these chemicals are being manufactured using batch or semi-batch processes. Nowadays, some microreactor plants are being used for commercial production. One of the best examples is the production of nitroglycerine using a microreactor plant in the range of 15 kg/h that is used as a drug for acute cardiac infraction. The process uses sulfuric and nitric acid, both highly concentrated fuming liquids, which are being handled well using microreactors. The high surface to volume ratio ensures an immediate transfer of the heat released by the reaction. Thus, the higher the yield, the better is the product quality. It also increases the safety and reduces the environmental hazards. In the present work, the production of hydrogen peroxide using DC process was investigated. Although it has been studied at the lab scale, it has not be scaled up to industrial production due to safety considerations. However, as demonstrated in this study, it is possible to conduct this reaction safely in a capillary microreactor, future work should be devoted to identify more of such processes and make them continuous using microreactors.

Scale-up: For large-scale productions, scale-up of microreactors is very important to achieve a throughput in the range of industrial scale. Microreactor technology achieves this target with numbering-up a commonly used scale up techniques for microreactors. The key aspect in scaling up or numbering up these microreactors is to maintain the same flow distribution amongst all the individual units in the bundle. Uniform distribution of flow in all channels is very important as it decides the processing of the

chemicals being used in the process. In the future, the flow distribution techniques must be developed to provide the same treatment for each unit in a bundle or monolith.

7.5.2 Spinning disc reactor

Polymeric materials are being used in a variety of day-to-day products. Although the demand of these materials is ever growing there are complexities in large-scale production of these materials. Variety of process and complicated reaction patterns require special attention. Some of these processes are batch process and produce low volume per batch. The aim is to manufacture the product with an acceptable quality apart from being safe and economic. In this case, it is important to have a precise tuning of the parameters in order to get the desired product. The spinning disc reactor is a powerful equipment for carrying out such processes. Centrifugal force can be used for suspension polymerization as it uses two immiscible liquids in which the monomer is initially dispersed in the continuous aqueous phase by the combined action of the surface-active agents. The monomer and initiator(s) reside in the organic or oil phase. It is commonly used for producing a wide variety of commercially important polymers such as polystyrene and its copolymers (poly-vinyl chloride, poly-methyl methacrylate, poly-vinyl acetate). Commonly used equipment for suspension polymerization is the agitated stirred tank. The agitation intensity and the properties of the suspending agent determine the sizes of the dispersed monomer drops. Whereas in the spinning disc reactor by controlling the disc speed, the inlet flow rate, the radial position of grooves etc., the final polymer particle size and its properties can be precisely tuned. More modelling and experimentation is required to understand these aspects.

With currently available computational capabilities, it is practically impossible to model 3D fully developed spinning disc reactors with grid size of less than 100 micron. It is suggested that in future techniques must be developed that allows the use of finer refined grid sizes. Also in future, the exothermic/endothermic reactions can be incorporated with cooling/heating disc surfaces included to study the heat transfer along with the mass transfer and chemical reactions.

7.5.3 Rotating tube reactor

More detailed modelling is also recommended to fully understand the benefits of this reactor. Experiments should be performed to validate the simulation results from this study.

Bibliography

- [1] S. Irandoust and B. Andersson, "Monolithic catalysts for non automobile applications," *Catalysis Reviews-Science and Engineering*, vol. **30**, pp. 341-392, 1988.
- [2] T. Boger, S. Roy, A. K. Heibel, and Borchers, "A monolith loop reactor as an attractive alternative to slurry reactors," *Catalysis Today*, vol. **79**, pp. 441-451, 2003.
- [3] L. Crynes, R. L. Cerro, and M. A. Abraham, "Monolith froth reactor-development of a novel 3-phase catalytic-system," *American Institute of Chemical Engineers Journal*, vol. **41**, pp. 337-345, 1995.
- [4] F. Kapteijn, T. A. Nijhuis, J. J. Heiszwolf, and J. A. Moulijn, "New non-traditional multiphase catalytic reactors based on monolithic structures," *Catalysis Today*, vol. **66**, pp. 133-144, 2001.
- [5] R. K. Edvinsson, A. M. Holmgren, and S. Irandoust, "Liquid-phase hydrogenation of acetylene in a monolithic catalyst reactor," *Industrial & Engineering Chemistry Research*, vol. **54**, pp. 94-100, 1995.
- [6] T. A. Nijhuis, M. T. Kreutzer, A. C. J. Romijn, F. Kapteijn, and J. A. Moulijn, "Monolithic catalysts as efficient three-phase reactors," *Chemical Engineering Science*, vol. **56**, pp. 823-829, 2001.
- [7] R. M. d. Deugd, R. B. Chougule, M. T. Kreutzer, F. M. Meeuse, J. Grievink, F. Kapteijn, and J. A. Moulijn, "Is a monolithic loop reactor a viable option for Fischer-Tropsch synthesis?," *Chemical Engineering Science*, vol. **58**, 2003.
- [8] R. K. Edvinsson and A. Cybulski, "A comparison between the monolithic reactor and the trickle-bed reactor for liquid-phase hydrogenations," *Catalysis Today*, vol. **24**, 1995.
- [9] T. Fukano and A. Kariyasaki, "Characteristics of gas-liquid two-phase flow in a capillary tube," *Nuclear Engineering and Design*, vol. **141**, pp. 59-68, 1993.
- [10] W. L. Chen, M. C. Twu, and C. Pan, "Gas-liquid two-phase flow in microchannels," *International Journal of Multiphase Flow*, vol. **28**, pp. 1235-1247, 2002.
- [11] P. M. Chung and M. Kawaji, "The effect of channel diameter on adiabatic two-phase flow characteristics in microchannels," *International Journal of Multiphase Flow*, vol. **30**, pp. 735-761, 2004.
- [12] K. A. Triplett, S. M. Ghiaasiaan, S. I. Abdel-Khalik, and D.L.Sadowski, "Gas-liquid two-phase flow in microchannels," *Part I: two-phase flow patterns*, vol. **25**, pp. 377-394, 1999.
- [13] C.-Y. Yang and C.-C. Shieh, "Flow pattern of air-water and two-phase R-134a in small circular tubes," *International Journal of Multiphase Flow*, vol. **27**, pp. 1163-1177, July 2001.
- [14] J. W. Coleman and S. Garimella, "Characterization of two-phase flow patterns in small diameter round and rectangular tubes," *International Journal of Heat and Mass Transfer*, vol. **42**, pp. 2869-2881, 1999.

- [15] M. K. Akbar, D. A. Plummer, and S. M. Ghiaasiaan, "On gas-liquid two phase flow regimes in microchannels," *International Journal of Multiphase Flow*, vol. **29**, pp. 855-865, 2003.
- [16] M. N. Kashid and D. W. Agar, "Hydrodynamics of liquidliquid slug flow capillary microreactors: flow regime, slug size and pressure drop," *Chemical Engineering Journal*, vol. **Volume 131**, pp. 1-13, 1 July 2007.
- [17] A. Stankiewicz and J. A. Moulijn, *Process Intensification: History, Philosophy, Principles*: Marcel Dekker, 2004.
- [18] I. Leshev and G. Peev, "Film flow on a horizontal rotating disk," *Chemical Engineering and Processing*, vol. **42**, pp. 925-929, 2003.
- [19] A. Aoune and C. Ramshaw, "Process intensification: heat and mass transfer characteristics of liquid films on rotating discs," *International Journal of Heat and Mass transfer*, vol. **42**, pp. 2543-2556, 1999.
- [20] J. R. Burns, C. Ramshaw, and R. J. Jachuck, "Measurement of liquid film thickness and the determination of spin-up radius on a rotating disc using an electrical resistance technique," *Chemical Engineering Science*, vol. **58**, pp. 2245-2253, 2003.
- [21] O. K. Matar and C. J. Lawrence, "The flow of thin liquid films over spinning disks: Hydrodynamics and mass transfer," *Physics of Fluids*, vol. **17**, pp. 052102, 2005.
- [22] C. Ramshaw, "HiGee' Distillation - An Example of Process Intensification " *Chem. Engr. - London*, vol. **389**, pp. 13-14, 1983.
- [23] P. Heggs, *Chemical engineering communications*, vol. **394**, 1983.
- [24] J. A. Moulijn, "Process intensification: Transforming chemical engineering," *Chemical Engineering Progress* vol. **96**, 2000.
- [25] J. Baldyga and J. R. Bourne, "A fluid mechanical approach to turbulent mixing and chemical reaction," *Chem. Eng. Commun.* , vol. **28** pp. 231281, 1984.
- [26] W. Ehrfeld, V. Hessel, and H. Lowe, *Microreactors*, 1 ed: Wiley-Vch, 2000.
- [27] R. Herbsthofer, H.-J. Bart, J. Wolfgang, and A. Prior, "Kombination von Reaktion und Trennung im präparativen annularen Chromatographen," *Chem Ing Tech*, vol. **73**, pp. 56-59, 2001.
- [28] F. Kapteijn, J. J. Heiszwolf, T. A. Nijhuis, and J. A. Moulijn, "CATTECH " , vol. **3**, 1999.
- [29] A. Stankiewicz, "Process intensification in in-line monolithic reactor," *Chemical Engineering Science*, vol. **56**, pp. 359 - 364, 2001.
- [30] E. Grolman, R. K. Edvinsson, A. Stankiewicz, and J. A. Moulijn, "Hydrodynamic instabilities in gas-liquid monolithic reactors.," *Proceedings of the ASME Heat Transfer Division*, vol. **HTD-vol. 334**, pp. 171-178, 1996.
- [31] C. H. Phillips and K. T. Symmonds, "Development of Novel Integrated Chemical Reactor-Heat Exchanger," *3rd International Conference on Process Intensification for Chemical Industry*, vol. **38**, pp. 71-87, 1999.
- [32] R. Patel, K. Singh, V. K. Pareek, and M. O. Tade, "Dynamic Simulation of Reactive Batch Distillation Column for Ethyl Acetate Synthesis," *Chemeca*, vol. **2**, 2007.
- [33] R. Taylor and R. Krishna, "Modelling reactive distillation," *Chemical Engineering Science*, vol. **55**, pp. 5183-5529, 2000.

- [34] R. S. Hiwale, N. V. Bhate, Y. S. Mahajan, and S. M. Mahajani, "Industrial applications of reactive distillation recent trends," *International Journal of Chemical Reactor Engineering*, vol. **2** 2004.
- [35] M. M. Sharma and A. K. Nanda, "Extraction with Second Order Reaction," *Trans. Inst. Chem. Eng.*, vol. **46**, pp. T44-T52, 1968.
- [36] R. D. Mhaskar and M. M. Sharma, "Extraction with Reaction in Both Phases," *Chemical Engineering Science*, vol. **30**, pp. 811-818, 1975.
- [37] T. V. Vasudevan and M. M. Sharma, "Some Aspects of Process Design of Liquid-Liquid Reactors," *Industrial & Engineering Chemistry Process Design and Development*, vol. **23**, pp. 100-406, 1984.
- [38] S. M. Mahajani, A. K. Kolah, and M. M. Sharma, "Extractive Reactions with Cationic Exchange Resins as Catalysts (Acetalization of Aldehydes with Alcohols)," *Reactive & Functional Polymers*, vol. **28**, pp. 29-38, 1995.
- [39] K. D. Samant and K. M. Ng, "Systematic Development of Extractive Reaction Processes," *Chemical Engineering Technology*, vol. **22**, pp. 877-880, 1999.
- [40] T. K. Poddar, S. Majumdar, and K. K. Sirkar, "Removal of VOCs from air by membrane-based absorption and stripping," *Journal of Membrane Science*, vol. **120**, pp. 221-237, 1996.
- [41] T. A. C. Oliveira, J. T. Scarpello, and A. G. Livingston, "Pervaporation-biological oxidation hybrid process for removal of volatile organic compounds from wastewaters," *Journal of Membrane Science*, vol. **195**, pp. 75-88, 2002.
- [42] M. Mujiburohman, W. B. Sediawan, and H. Sulisty, "A preliminary study: Distillation of isopropanol-water mixture using fixed adsorptive distillation method," *Separation Purification Technology*, vol. **48**, pp. 85-92, 2006.
- [43] F. Banat, S. Al-Asheh, and N. Al-Lagtah, "Adsorptive distillation using molecular sieves and low-cost biobased adsorbents for the break-up of the isopropanol-water azeotrope," *Adsorption Science Technology*, vol. **21** pp. 821-830, 2003.
- [44] C. Zheng, K. Guo, Y. Song, X. Zhou, D. Al, Z. Xin, and N. C. Gardner, "Industrial Practice of HIGRAVITEC in Water Deaeration," *Second International Conference Process Intensification in Practice*, vol. **28**, pp. 273-287, 1997.
- [45] D. Trent and D. Tirtiwidjojo, "Commercial operation of a rotating packed bed (RPB) and other applications of RPB technology," *Proceedings of the 4th International Conference on Process Intensification for the Chemical Industry*, pp. 11-19, 2001.
- [46] S. K. Dhiman, V. Verma, D. P. Rao, and M. S. Rao, "Process intensification in a trickle-bed reactor: Experimental studies," *AIChE*, vol. **51**, pp. 3186-3192, 2005.
- [47] J. M. Coulson and J. F. Richardson, "Chemical Engineering," vol. 5: Butterworth-Heinemann, 1999, pp. 1123.
- [48] D. J. Peet, M. A. T. Bisschops, S. H. V. Hateren, and L. A. M. V. D. Wielen, "Albumin recovery with centrifugal adsorption technology (CAT)," *Biotechnology and Bioengineering* vol. **78**, pp. 237-250, 2002.
- [49] V. V. Kelkar and K. M. Ng, "Design of reactive crystallization systems incorporating kinetics and mass-transfer effects," *AIChE* vol. **45**, pp. 69, 1999.
- [50] C. R. Bayley and N. A. Vaidya, "Resolution of Racemates by Diastereomeric Salt Formation," *Chirality in Industry*, pp. 70-77, 1992

- [51] R.-y. Lina, J.-y. Zhanga, and Y.-q. Baic, "Mass transfer of reactive crystallization next term in synthesizing calcite nanocrystal," *Chemical Engineering Science*, vol. **61**, pp. 7019-7028, 2006.
- [52] D. J. Safarik and R. B. Eldridge, "Olefin/Paraffin Separations by Reactive Absorption: A Review," *Industrial & Engineering Chemistry Research*, vol. **37**, pp. 2571-2581, 1998.
- [53] M. Ebrahimi-Moshkabad and J. M. Winterbottom, "The behaviour of an intermeshing twin screw extruder with catalyst immobilised screws as a three-phase reactor," *Catalysis Today*, vol. **48**, pp. 347-355, 1999.
- [54] C. Tzaganakis, *Advance Polymer Technology*, vol. 9, 1989.
- [55] F. Lode, M. Houmarda, C. Migliorini, M. Mazzotti, and M. Morbidelli, "Continuous reactive chromatography," *Chemical Engineering Science*, vol. **56**, pp. 269-291, 2001.
- [56] E. Y. Kenig, R. Schneidera, and A. Górak, "Reactive absorption: Optimal process design via optimal modelling," *Chemical Engineering Science*, vol. **56**, pp. 343-350, 2001.
- [57] K. R. Westerterp, T. N. Bodewes, M. S. A. Vrijand, and M. Kuczynski, "Two new methanol converters," *Hydrocarbon Process. ; Vol/Issue: 67:11*, pp. Pages: 69-74, 1988.
- [58] G. C. Vaporciyan and R. H. Kadlec, "Periodic Separating Reactors: Experiments and Theory," *AIChE*, vol. **35**, pp. 831-844, 1989.
- [59] G. Dunnebier, J. Fricke, and K.-U. Klatt, "Optimal Design and Operation of Simulated Moving Bed Chromatographic Reactors," *Industrial & Engineering Chemistry Research*, vol. **39**, pp. 2290-2304, 2000.
- [60] S. R. Wickramasinghe and D. L. Grzenia, "Adsorptive membranes and resins for acetic acid removal from biomass hydrolysates " *Desalination*, vol. **234**, pp. 144-151, 2008.
- [61] K. Smolders and A. C. M. Franken, "Terminology for membrane distillation," *Desalination* vol. **72** pp. 249-262, 1989.
- [62] A. O. Imdakma, M. Khayet, and T. Matsuura, "A Monte Carlo simulation model for vacuum membrane distillation process," *Journal of Membrane Science*, vol. **306**, pp. 341-348, 2007.
- [63] M. Khayet, P. Godino, and J. I. Mengual, "Theory and experiments on sweeping gas membrane distillation," *Journal of Membrane Science*, vol. **165** pp. 261-272, 2000.
- [64] S. Kimura and S. Nakao, "Transport phenomena in membrane distillation " *Journal of Membrane Science*, vol. **33** pp. 285-298, 1987.
- [65] B. Pohlman, H. D. Scharf, U. Jarolimek, and P. Mauermann, "Photochemical Production of Fine Chemicals with Concentrated Sunlight," *Solar Energy*, vol. **61**, pp. 159-168, 1997.
- [66] N. J. Peill and M. R. Hoffman, "Solar-Powered Photocatalytic Fiber-Optic Cable Reactor for Waste Stream Remediation," *Journal of solar Energy and Engineering*, vol. **119**, pp. 229-236, 1997.
- [67] O. Levenspiel, *Chemical Reaction Engineering*, vol. 3: Wiley, 1999.
- [68] H. K. Versteeg and W. Malalasekera, *An introduction to computational fluid dynamics The finite volume method*, vol. 1: Prentice Hall, 1995.

- [69] C. K. Harris, D. Roekaerts, and F.J.J. Rosendal, "Computational Fluid Dynamics for Chemical Reactor Engineering," *Chemical Engineering Science*, vol. **51**, pp. 1569-1594, 1996
- [70] A. D. Gosman, "Developments in industrial computational fluid dynamics," *Trans IChemE*, vol. **76**, pp. 153-161, 1998.
- [71] J. F. Thompson, B. K. Soni, and N. P. Weatherill, *Handbook of grid generation* Boca Raton, 1999.
- [72] P. Kopyt and W. Gwarek, "A comparison of commercial CFD software capable of coupling to external electromagnetic software for modeling of microwave heating process," presented at 6th Seminar in Computer Modelling and Microwave Power Engineering, Austin, Texas, USA, 2004.
- [73] T. Norton, D.-W. Sun, J. Grant, R. Fallon, and V. Dodd, "Applications of computational fluid dynamics (CFD) in the modelling and design of ventilation systems in the agricultural industry: A review," *Bioresource Technology*, vol. **98**, pp. 2386-2414, 2007.
- [74] P. G. Tucker, "CFD Applied to Electronic Systems: A Review," *IEEE Transactions on Components, Packaging, and Manufacturing Technology-Part A*, vol. **20**, pp. 518-529, 1997.
- [75] V. V. Ranade, *Computational flow modeling for chemical reactor engineering*, vol. 1, 2002.
- [76] R. B. Bird, W. E. Stewart, and E. N. Lightfoot, *Transport Phenomena*. New York: N.Y.: Willey, 1960.
- [77] J. H. Ferziger and M. Peric, *Computational Methods for Fluid Dynamics*. Berlin: Springer, 1999.
- [78] G. D. Smith, *Numerical solution of partial differential equation: finite difference methods*, 3rd ed. Oxford: Clarendon Press, 1985.
- [79] B. Carnahan, H. A. Luther, and J. O. Wilkes, *Applied Numerical Methods*. New York: John Wiley and Sons, 1969.
- [80] O. C. Zienkiewicz and R. L. Taylor, *The finite element method: Solid and fluid mechanics*, vol. 2. New York: Mcgraw-Hill, 1991.
- [81] S. V. Patankar and D. B. Spalding, "A calculation procedure for heat, mass and momentum transfer in three-dimensional parabolic flows," *International Journal of Heat and Mass Transfer*, vol. **115**, pp. 1787-1803, 1972.
- [82] S. V. Patankar, *Numerical Heat Transfer and Fluid Flow*. Washington, DC: Hemisphere Publishing Corporation, 1980.
- [83] *Fluent User Manual*, vol. **6.3**, 2007.
- [84] R. Krishna, J. M. v. Baten, and M. I. Urseanu, "Three-Phase Eulerian Simulations of Bubble Column Reactors Operating in the Churn-Turbulent Regime: A Scale Up Strategy," *Chemical Engineering Science*, vol. **55**, pp. 3275-3286, 2000.
- [85] D. A. Drew, "Mathematical Modeling of Two-phase Flow," *Annual Reviews in Fluid Mechanics*, vol. **15**, pp. 261-291, 1983.
- [86] W. D. Deckwer, *Bubble Column Reactors*. New York: John Wiley and Sons, 1984.
- [87] W. D. Deckwer, Y. Louisi, A. Zaidi, and M. Ralek, "Gas Holdup and Physical Transport Properties for the Fischer-Tropsch Synthesis in Slurry Reactor," *AIChE Annual Meeting*, 1979.

- [88] V. K. Pareek, "Application of computational fluid dynamics (CFD) in design and simulation of three-phase photocatalytic reactors " in *Department of Chemical Engineering*. Sydney: UNSW, 2002, pp. 347.
- [89] C. W. Hirt and B. D. Nichols, "Volume of fluid (VOF) method for the dynamics of free boundaries," *Journal of Computational Physics*, vol. **39** pp. 201–225, 1981.
- [90] V. R. Gopala and B. G. M. v. Wachem, "Volume of fluid methods for immiscible-fluid and free-surface flows," *Chemical Engineering Journal* vol. **141** pp. 204–221, 2008.
- [91] M. N. Kashid and D. W. Agar, "Hydrodynamics of liquid-liquid slug flow capillary microreactors: flow regime, slug size and pressure drop," *Chemical Engineering Journal*, vol. **131**, pp. 1-13, 2007.
- [92] W.-D. Deckwer, *Bubble column reactors*. Weinheim: VCH, 1985.
- [93] H. Judat, "Stoffaustausch Gas/Flussigkeit im Ruhrkessel-eine kritische Bestandsaufnahme," *Chemical engineering technology*, vol. **54** pp. 520–521, 1982.
- [94] H. Blenke, "Loop reactors," in *Advances in Biochemical Engineering.*, vol. 13 Berlin: Springer, 1979, pp. 121–214.
- [95] H. Brauer, *Biological Waste water treatment in a reciprocating jet bioreactor*. Weinheim, 1985.
- [96] E. S. Gaddis and A. Vogelpohl, "The impinging-stream reactor: A high performance loop reactor for mass transfer controlled chemical reactions," *Chemical Engineering Science*, vol. **47**, pp. 2877-2882, 1992.
- [97] E. S. Gaddis, "Mass transfer in gas–liquid contactors," *Chemical Engineering and Processing*, vol. **38**, pp. 503–510, 1999.
- [98] J. C. Godfrey and M. J. Slater, *Liquid-liquid extraction equipment*: John Wiley and Sons, 1994.
- [99] C.-Y. Yang and C.-C. Shieh, "Flow pattern of air-water and two-phase R-134a in small circular tubes," *International Journal of Multiphase Flow*, vol. **27**, 2001.
- [100] S. C. K. D. Schepper, G. J. Heynderickx, and G. B. Marin, "CFD modeling of all gas–liquid and vapor–liquid flow regimes predicted by the Baker chart," *Chemical Engineering Journal*, vol. **138**, pp. 349–357, 2008.
- [101] J. M. v. Baten and R. Krishna, "CFD simulations of mass transfer from Taylor bubbles rising in circular capillaries," *Chemical Engineering Science*, vol. **59**, pp. 2535 – 2545, 2004.
- [102] J. R. Burns and C. Ramshaw, "The intensification of rapid reactions in multiphase systems using slug flow in capillaries," *Lab on a Chip* vol. **1** pp. 1015, 2001.
- [103] G. Dummann, U. Quittmann, L. Groschel, D. W. Agar, O. Worz, and K. Morgenschweis, "The capillary microreactor: a new reactor concept for the intensification of heat and mass transfer in liquid liquid reactions," *Catalysis Today*, vol. **7980** pp. 433-439, 2003.
- [104] M. Suo and P. Griffith, "Two phase flow in capillary tubes," *Journal of Basic Engineering*, vol. **86**, pp. 576–582, 1964.
- [105] D. Qian and A. Lawal, "Numerical Study on Gas and Liquid Slugs for Taylor Flow in a T- Junction Microchannel," *Chemical Engineering Science*, vol. **61**, pp. 7609-7625, 2006.

- [106] J. Pellicer, V. Garcia-Morales, and M. Hernandez, "On the demonstration of the Young-Laplace equation in introductory physics courses," *Phys Educ* vol. **35**, pp. 126-29, 2000.
- [107] W. Rasband, "ImageJ ver. 1.41": National Institute of Health, <http://rsbweb.nih.gov/ij/index.html>, 2008.
- [108] C.O. Vandu, H. Liu, and R. Krishna, "Taylor bubble rise in circular and square capillaries." Amsterdam: University of Amsterdam, The Netherlands, 2004.
- [109] R. Courant, K. Friedrichs, and H. Lewy, "On the Partial Difference Equations of Mathematical Physics," *IBM Journal*, vol. **11**, pp. 215-234, 1967.
- [110] M. T. Kreutzer, F. Kapteijn, J. A. Moulijn, and J. J. Heiszwolf, "Multiphase monolith reactors: chemical reaction engineering of segmented flow in microchannels," *Chemical Engineering Science*, vol. **60**, pp. 5895-5916, 2005.
- [111] F. Bretherton, "The motion of long bubbles in tubes " *Journal of Fluid Mechanics*, vol. **10**, pp. 166–188, 1961.
- [112] C. Horvath, B. Soloman, and J. Engasser, "Measurement of Radial Transport in Slug Flow Using Enzyme Tubes," vol. **12**, pp. 431-439, 1973.
- [113] H. Fujioka and J. B. Grotberg, "Steady Propagation of a Liquid Plug in a Two-Dimensional Channel," *Journal of Biomechanical Engineering*, vol. **126**, pp. 567-577, 2004
- [114] A. Kawahara, P. M.-Y. Chung, and M. Kawaji, "Investigation of two-phase flow pattern, void fraction and pressure drop in a microchannel " *International Journal of Multiphase Flow*, vol. **28**, pp. 1411-1435, 2002.
- [115] D. M. Fries, F. Trachsel, and P. R. v. Rohr, "Segmented gas–liquid flow characterization in rectangular microchannels," *International Journal of Multiphase Flow*, vol. **34**, pp. 1108–1118, 2008.
- [116] C. Peter M.-Y, M. Kawaji, A. Kawahara, and Y. Shibata, "Two-Phase Flow Through Square and Circular Microchannels—Effects of Channel Geometry," *Journal of Fluids Engineering*, vol. **126**, pp. 546-553, 2004
- [117] A. L. Hazel and M. Heil, "The steady propagation of a semi-infinite bubble into a tube of elliptical or rectangular cross-section," *Journal of Fluid Mechanics*, vol. **470**, pp. 91–114, 2002.
- [118] R. Gruber, "Radial mass transfer enhancement in bubble train flow.," in *RWTH Aachen*. Germany, 2001.
- [119] T. C. Thulasidas, M. A. Abraham, and R. L. Cerro, "Flow pattern in liquid slugs during bubble train flow inside capillaries," *Chemical Engineering Science*, vol. **52**, pp. 2947–2962, 1997.
- [120] M. N. Kashid, "Experimental and Modelling Studies on Liquid-Liquid Slug Flow Capillary Microreactors," in *Department of Biochemical and Chemical Engineering*, vol. PhD. Dortmund: University of Dortmund, 2007, pp. 213.
- [121] P. Aussilous and D. Quéré, "Quick deposition of a fluid on the wall of a tube," *Physics of Fluids*, vol. **12** pp. 2367–2371, 2000.
- [122] M. Zangir and A. Gavriilidis, "Carbon Dioxide Absorption in a Falling Film Microstructured Reactor: Experiments and Modeling," *Industrial Engineering Chemistry and Research*, vol. **44**, pp. 1742-1751, 2005.
- [123] V. Haverkamp, V. Hessel, M. A. Liauw, H. Lowe, and M. G. Menges, "Reactor Model for Fast Reactions in the Micro-Bubble Column and Validation," *Industrial Engineering Chemistry and Research*, vol. **46**, pp. 8558-8565, 2007.

- [124] N. Harries, J. R. Burns, D. A. Barrow, and C. Ramshaw, "A numerical model for segmented flow in a microreactor," *International Journal of Heat and Mass Transfer*, vol. **46**, pp. 3313–3322, 2003.
- [125] G. Bercic and A. Pintar, "The Role of Gas Bubbles and Liquid Slug Lengths on Mass Transport in the Taylor Flow through Capillaries," *Chemical Engineering Science*, vol. **52**, pp. 3709, 1997.
- [126] Y. Voloshin, R. Halder, and A. Lawal, "Kinetics of hydrogen peroxide synthesis by direct combination of H₂ and O₂ in a microreactor," *Catalysis Today*, vol. **125**, pp. 40–47, 2007.
- [127] Y. Voloshin and A. Lawal, "Kinetics of hydrogen peroxide reduction by hydrogen in a microreactor," *Applied Catalysis A: General*, vol. **353**, pp. 9–16, 2009.
- [128] Y. Voloshin, A. Manganaro, and A. Lawal, "Kinetics and Mechanism of Decomposition of Hydrogen Peroxide over Pd/SiO₂ Catalyst," *Industrial Engineering Chemistry and Research*, vol. **47**, pp. 8119–8125, 2008.
- [129] T. Inoue, Martin A. Schmidt, and K. F. Jensen, "Microfabricated Multiphase Reactors for the Direct Synthesis of Hydrogen Peroxide from Hydrogen and Oxygen," *Industrial Engineering Chemistry and Research*, vol. **46**, pp. 1153–1160, 1997.
- [130] F. Chen, M.-H. Chang, and C.-W. Hsu, "Analysis of membraneless microfuel cell using decomposition of hydrogen peroxide in a Y-shaped microchannel," *Electrochimica Acta*, vol. **52**, pp. 7270–7277, 2007.
- [131] Kirk-Othmer, "Encyclopedia of Chemical Technology," 5th ed: John Wiley and Sons, 2004.
- [132] Y. H. Izumi, S. Miyazaki, and Kawahara, "Process for preparing hydrogen peroxide." US, 1977.
- [133] A. I. Dalton and R. W. Skinner, "Synthesis of hydrogen peroxide." US, 1982.
- [134] M. Kawakami, Y. Ishiuchi, H. Nagashima, T. Tomita, and Y. Hiramatsu, "Process for producing hydrogen peroxide." US, 1995.
- [135] L. W. Gosser, "Catalytic process for making H₂O₂ from hydrogen and oxygen." US, 1988.
- [136] M. Fischer, T. Butz, and K. Masonne, "Preparation of hydrogen peroxide from hydrogen and oxygen." US 2005.
- [137] M. Paoli, "Process for the production of hydrogen peroxide from hydrogen and oxygen." US, 1993.
- [138] K. T. Chuang and B. Zhou, "Production of hydrogen peroxide." US 1994.
- [139] M. T. Janicke, H. Kestenbaum, U. Hagedorf, F. Schuth, M. Fichtner, and K. Schubert, "The controlled oxidation of hydrogen from an explosive mixture of gases using a microstructured reactor/heat exchanger and Pt/Al₂O₃ catalyst," *Journal of Catalysis*, vol. **191** pp. 282–293, 2000.
- [140] G. Vesper, "Experimental and theoretical investigation of H₂ oxidation in a high temperature catalytic microreactor," *Chemical Engineering Science*, vol. **56** pp. 1265–1273, 2001.
- [141] X. Wang, Y. Nie, J. L. C. Lee, and S. Jaenicke, "Evaluation of multiphase microreactors for the direct formation of hydrogen peroxide," *Applied Catalysis A: General* vol. **317**, pp. 258–265, 2007.

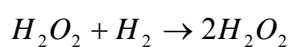
- [142] D. Reay, C. Ramshaw, and A. Harvey, *Process Intensification*, vol. 1. Oxford: IChemE, 2008.
- [143] T. S. Faghri and W. Hankey, "Experimental analysis and flow visualization of a thin liquid on a stationary and rotating disc," *Trans Asme Journal of Fluids Engineering*, vol. **113**, pp. 73-80, 1991.
- [144] F. K. Wasden and A. E. Dukler, "A numerical study of mass transfer in free-falling wavy films," *AIChE* vol. **36**, pp. 1379-1390, 1990.
- [145] N. Brauner, D. M. Maron, and A. E. Dukler, "Modeling of wavy flow in inclined thin films in the presence of interfacial shear," *Chemical Engineering Science* vol. **40**, pp. 923-937, 1985.
- [146] A. F. Charwat, R. E. Kelly, and C. Gazley, "The flow and stability of thin liquid films on a rotating disc," *Journal of Fluid Mechanics*, vol. **53**, pp. 227-255, 1972.
- [147] H. Espig and R. Hoyle, "Waves in a thin layer on a rotating disk.," *Journal of Fluid Mechanics*, vol. **22**, pp. 671-677, 1965.
- [148] A. I. Butuzov and I. I. Puhovoi, "On regimes of liquid film flows over a rotating surface," *Journal of Engineering Physics*, vol. **31**, pp. 217 1976.
- [149] R. M. Wood and B. E. Watts, "The flow, heat and mass transfer characteristics of liquid films on rotating discs," *Transactions of the Institution of Chemical Engineers*, vol. **51**, pp. 315-322, 1973.
- [150] W. P. Woods, "The hydrodynamics of thin liquid films flowing over a rotating disc." Newcastle, U.K.: Newcastle University, 1995.
- [151] J. W. Rauscher, R. E. Kelly, and J. D. Cole, "An asymptotic solution for the laminar flow of a thin film on a rotating disc," *Journal of Applied Mechanics (ASME Series E)*, vol. **40**, pp. 43-47, 1973.
- [152] V. Y. Shkadov, "Some methods and problems of the theory of hydrodynamic stability " *Scientific Proceedings 25 Institute of Mechanics of Lomonosov Moscow State University, Moscow*, 1973.
- [153] I. Lepekhin, G. V. Ryabchuk, N. V. Tyabin, and E. R. Shulman, "Viscous liquid flow on a surface of a spinning plane disc," *Theor. Found. Chem. Eng.* , vol. **15**, pp. 391 1981.
- [154] A. F. Shvets, L. P. Portnov, G. G. Filippov, and A. I. Gorbunov, "Flow of an axisymmetric film of viscous liquid on the surface of a spinning disc," *Theor. Found. Chem. Eng.*, vol. **26**, pp. 895, 1992.
- [155] L. A. Dorfman, "Flow and heat transfer in a viscous liquid layer on a spinning disc," *Journal of Engineering Physics*, vol. **12**, pp. 309 1967.
- [156] G. M. Sisoiev, A. F. Tal'drik, and V. Y. Shkadov, "Flow of a viscous liquid film on the surface of a rotating disc," *Journal of Engineering Physics*, vol. **51**, pp. 1171 1986.
- [157] T. Azuma and M. Nunobe, "Laminar-turbulent transition in radial liquid film flow on a rotating disk " *Trans Jap Soc Mech Eng*, vol. **55 B**, pp. 2139-2147 (in Japanese), 1989.
- [158] G. Lenewit, K. G. Roesner, and R. Koehler, "Surface instabilities of thin liquid film flow on a rotating disk," *Experiments in Fluids*, vol. **26**, pp. 75-85, 1999.
- [159] G. I. Lepekhin and G. V. Riabchuk, "Temperature Distribution in Film of Viscous Liquid with Heating on a Rotating Disk," *Rheology In Processes and Apparatus of Chemical Technology, Works of Polytechnic Institute of Volgograd*, pp. 82-91, 1975.

- [160] S. Thomas, A. Faghri, and W. Hankey, "Experimental analysis and flow visualization of a thin liquid film on a stationary and rotating disk," *Journal of Fluids Engineering*, vol. **113**, pp. 73-80, 1991.
- [161] C. Ramshaw, "Protensive," www.protensive.co.uk
- [162] C. Raston, "Personal Communications with Professor Colin Raston," T. Bhatelia, Ed. Perth, 2006-2009.
- [163] N. A. S. Webster, C. D. Ling, and F. J. Lincoln, "The structural and conductivity evolution of fluorite-type Bi₂O₃-Er₂O₃-PbO solid electrolytes during long-term annealing," *Solid State Ionics*, vol. **179**, pp. 697-705, 2008.
- [164] N. Anantachoke, M. Makha, C. L. Raston, V. Reutrakul, N. C. Smith, and M. Saunders, "Fine Tuning the Production of Nanosized B-Carotene Particles Using Spinning Disk Processing," *Journal of the American Chemical Society*, vol. **128**, pp. 13847-13853, 2006.
- [165] R. David, R. Colin, and H. Adam, "Process Intensification: Engineering for Efficiency, Sustainability and Flexibility ". Oxford: Butterworth-Heinemann, 2008, pp. 103-186.
- [166] J. Chen, Y. Wang, Z. Jia, and C. Zheng, "Proceedings of the 2nd Conference Series, No. 28," *International Conference on Process Intensification in Practice. BHR Group*, pp. 157-162, 1997.
- [167] J. R. Lawrence, G. D. W. Swerhone, and T. R. Neu, "A simple rotating annular reactor for replicated biofilm studies," *Journal of Microbiological Methods*, vol. **42**, pp. 215-224 2000.
- [168] R. A. Damodar and T. Swaminathan, "Performance evaluation of a continuous flow immobilized rotating tube photocatalytic reactor (IRTPR) immobilized with TiO₂ catalyst for azo dye degradation," *Chemical Engineering Journal*, vol. **144**, pp. 59-66, 2008.
- [169] F. Kargi and S. Eker, "Performance of rotating perforated tubes biofilm reactor in biological wastewater treatment," *Enzyme and Microbial Technology*, vol. **32**, pp. 464-471, 2003.
- [170] H. Guoxin, G. Xiwu, H. Hao, F. Haojie, and W. Zheng, "Experimental studies on flow and pyrolysis of coal with solid heat carrier in a modified rotating cone reactor," *Chemical Engineering and Processing: Process Intensification*, vol. **47**, pp. 1777-1785, 2008.
- [171] T. Rezić, B. Šantek, S. Novak, and V. Marić, "Comparison between the heterotrophic cultivation of *Paracoccus denitrificans* in continuous stirred tank reactor next term and horizontal previous term rotating next term tubular bioreactor " *Process Biochemistry*, vol. **41**, pp. 2024-2028 2006.
- [172] P. W. Morrison, J. O. Taweechokesupsin, C. S. Kovach, B. Roozbehani, and J. C. Angus, "In situ infrared measurements during hot filament CVD of diamond in a rotating substrate reactor," *Diamond and related materials*, vol. **5**, pp. 242-246, 1996.

Appendix A

In this section, details of the mass balances and stoichiometric calculations performed on the slug flow capillary microreactor system are presented. The calculated values of the mass fraction of each species were compared with the simulation results in Chapter 4, section 4.6.11.

Reaction:



Inlet conditions

H₂O₂			
Concentration	0.34 mol/l	Velocity m/s	0.18
Mass fraction	0.01156	Area m ²	3.14E-06
		Volumetric flow rate m ³ /s	5.65E-07
Density kg/m ³	1100	Mass Flow rate kg/s	7.19E-06
MW	34.05	kmol/s	2.11E-07
H₂O			
Mass fraction	0.98844	Velocity m/s	0.18
		Area m ²	3.14E-06
		Volumetric flow rate m ³ /s	5.65E-07
Density kg/m ³	1000	Mass Flow rate kg/s	5.59E-04
MW	18	kmol/s	3.10E-05
		Total Mass flow rate	5.66E-04
H₂			
Mass fraction	0.291	Velocity m/s	0.57
		Area m ²	3.14E-06
		Volumetric flow rate m ³ /s	1.79E-06
Density kg/m ³	0.08189	Mass Flow rate kg/s	4.27E-8
MW	2	kmol/s	2.13E-8
N₂			
Mass fraction	0.709	Velocity m/s	0.57
		Area m ²	3.14E-06
		Volumetric flow rate m ³ /s	1.79E-07
Density kg/m ³	1.251	Mass Flow rate kg/s	7.01972E-07
MW	28	kmol/s	2.51E-08
		Total Mass flow rate	7.45e-7

$$\text{Reaction rate: } R_{H_2O_2}^3 = \frac{C_{H_2O_2,in} - C_{H_2O_2,out}}{W} \frac{34gH_2O_2}{mol}$$

$$\text{Volume of Reactor} = 1.21E-7 \text{ m}^3$$

$$\text{Conversion} = 14\%$$

Outlet conditions:

H ₂ O ₂			
kmol/sec reacted	3.02E-08	Mass Fraction of H₂O₂ out	0.0109
kmol/sec unreacted	1.81E-07		
kg of H ₂ O ₂ reacted	1.03E-06		
kg of H ₂ O ₂ unreacted	6.16E-06	Total Mass out	5.66E-04
kmol/sec reacted	3.02E-08		
H ₂ O			
Kmol/sec produced	6.04E-08		
Kg of H ₂ O produced	1.09E-06	Mass fraction of H₂O out	0.9891
H ₂			
kmol of H ₂ Reacting	3.02E-08		
kg of H ₂	1.21E-07		
kg of H ₂ unreacted	7.80E-08		
kg of N ₂ inert	5.01E-07		
Total kg	5.79E-07	Mass fraction of H₂	0.135